Utilizing Changes in Repeating Earthquakes to Monitor Evolving Processes and Structure Before and During Volcanic Eruptions

Alicia Hotovec-Ellis

A dissertation

submitted in partial fulfillment of the

requirements for the degree of

Doctor of Philosophy

University of Washington

2014

Reading Committee:

John Vidale, Chair

Joan Gomberg

Seth Moran

Program Authorized to Offer Degree:

Department of Earth and Space Sciences

University of Washington

Abstract

Utilizing Changes in Repeating Earthquakes to Monitor Evolving Processes and Structure Before and During Volcanic Eruptions

Alicia Hotovec-Ellis

Chair of the Supervisory Committee:

Professor John Vidale

Department of Earth and Space Sciences

Repeating earthquakes are two or more earthquakes that share the same source location and source mechanism, which results in the earthquakes having highly similar waveforms when recorded at a seismic instrument. Repeating earthquakes have been observed in a wide variety of environments: from fault systems (such as the San Andreas and Cascadia subduction zone), to hydrothermal areas and volcanoes. Volcano seismologists are particularly concerned with repeating earthquakes, as they have been observed at volcanoes along the entire range of eruptive style and are often a prominent feature of eruption seismicity.

The behavior of repeating earthquakes sometimes changes with time, which possibly reflects subtle changes in the mechanism creating the earthquakes. In Chapter 1,

we document an example of repeating earthquakes during the 2009 eruption of Redoubt volcano that became increasingly frequent with time, until they blended into harmonic tremor prior to several explosions. We interpreted the source of the earthquakes as stick-slip on a fault near the conduit that slipped increasingly often as the explosion neared in response to the build-up of pressure in the system.

The waveforms of repeating earthquakes may also change, even if the behavior does not. We can quantify changes in waveform using the technique of coda wave interferometry to differentiate between changes in source and medium. In Chapters 2 and 3, we document subtle changes in the coda of repeating earthquakes related to small changes in the near-surface velocity structure at Mount St. Helens before and during its eruption in 2004. Velocity changes have been observed prior to several volcanic eruptions, are thought to occur in response to volumetric strain and the opening or closing of cracks in the subsurface. We compared continuous records of velocity change against other geophysical data, and found that velocities at Mount St. Helens change in response to snow loading, fluid saturation, shaking from large distant earthquakes, shallow pressurization, and possibly lava extrusion. Velocity changes at Mount St. Helens are a complex mix of many different effects, and other complementary data are required to interpret the signal.

TABLE OF CONTENTS

Page

LIST OF FIGURES

Figure Number Page

LIST OF TABLES

Table Number Page

CHAPTER 1:

Strongly Gliding Harmonic Tremor During the 2009 Eruption of Redoubt Volcano

The content of this chapter was published as part of a Special Issue in:

Hotovec, A. J., S. G. Prejean, J. E. Vidale, and J. Gomberg (2013) Strongly Gliding Harmonic Tremor During the 2009 Eruption of Redoubt Volcano, *Journal of Volcanology and Geothermal Research,* 259, 89–99, doi:10.1016/j.jvolgeores.2012.01.001.

The reader may also be interested in the follow-up paper:

Dmitrieva, K., A. J. Hotovec-Ellis, S. Prejean, and E. M. Dunham (2013) Frictional-faulting model for harmonic tremor before Redoubt Volcano eruptions, *Nature Geoscience,* 6, 652–656, doi:10.1038/ngeo1879.

Abstract

During the 2009 eruption of Redoubt Volcano, Alaska, gliding harmonic tremor occurred prominently before six nearly consecutive explosions during the second half of the eruptive sequence. The fundamental frequency repeatedly glided upward from <1 Hz to as high as 30 Hz in less than ten minutes, followed by a relative seismic quiescence of 10 to 60 seconds immediately prior to explosion. High frequency (5 to 20 Hz) gliding returned during the extrusive phase, and lasted for 20 minutes to 3 hours at a time. Although harmonic tremor is not uncommon at volcanoes, tremor at such high frequencies is a rare observation. These frequencies approach or exceed the plausible upper limits of many models that have been suggested for volcanic tremor. We also

analyzed the behavior of a swarm of repeating earthquakes that immediately preceded the first instance of pre-explosion gliding harmonic tremor. We find that these earthquakes share several traits with upward gliding harmonic tremor, and favor the explanation that the gliding harmonic tremor at Redoubt Volcano is created by the superposition of increasingly frequent and regular, repeating stick-slip earthquakes through the Dirac comb effect.

1. Introduction

Harmonic tremor is a continuous seismic and sometimes acoustic signal that often accompanies unrest on volcanoes of varying compositions and behaviors. Several narrow, evenly spaced peaks dominate the frequency spectrum of the signal: a fundamental tone and its overtones, with the fundamental tone usually in the range of 1 to 5 Hz [Neuberg, 2000; de Angelis and McNutt, 2007]. Frequencies of the peaks often change with time, forming "gliding spectral lines" on spectrograms.

Behavior of harmonic tremor is highly variable from volcano to volcano, but can be roughly grouped by style of eruption. Harmonic tremor during times of high explosive activity can be complex, but upward gliding of harmonic tremor immediately prior to an explosion has been observed at Arenal Volcano, Costa Rica [Lesage et al., 2006], and Soufrière Hills Volcano, Montserrat [Powell and Neuberg, 2003]. In both cases, the fundamental tone rose nearly monotonically from 1 to 3 Hz in the span of a few minutes. Chugging is a subset of harmonic tremor immediately following steam or Strombolian explosions, and is often accompanied by audible sounds and pulsed acoustic recordings. Chugging has been observed following Strombolian explosions at Mt. Semeru Volcano,

Indonesia [Schlindwein et al., 1995], Arenal Volcano, Costa Rica [Benoit and McNutt, 1997; Hagerty et al., 2000; Lesage et al., 2006], Karymsky Volcano, Russia [Ozerov et al., 2003; Lees et al., 2004], Reventador Volcano [Johnson and Lees, 2000], Sangay Volcano [Lees and Ruiz, 2008], and Tungurahua Volcano [Ruiz et al., 2006], Ecuador, and following Vulcanian explosions at Sakurajima Volcano, Japan [Maryanto et al., 2008]. The fundamental tone shifts both up and down in the range of 0.5 and 4 Hz, and lasts on the order of seconds to minutes. Alternatively, harmonic tremor can last minutes to hours during times of low explosive or eruptive activity. The fundamental tone remained steadily around 1 Hz for 18 hours at Lascar Volcano, Chile [Hellweg, 2000], for at least 6 hours at Veniaminof Volcano, Alaska [de Angelis and McNutt, 2007], and for almost 2 hours at Erebus Volcano, Antarctica [Rowe et al., 2000]. Reventador Volcano produced multiple cases of harmonic tremor with a fundamental tone of 2 Hz that glided slightly, and lasted tens of minutes to hours at a time [Lees et al., 2008]. Periods of gliding from 5 to 9 Hz, and perhaps as high as 20 Hz, lasted for almost an hour at Stromboli Volcano, Italy, during a non-explosive phase of eruption [Ripepe et al., 2009].

Although gliding harmonic tremor is relatively common on active volcanoes, the mechanism producing the signal is still debated. A wide variety of models have been proposed that are capable of producing harmonics. The first model invokes the resonance of a fluid-filled crack, described by Chouet [1985]. In this model, a hydrothermal crack, or the volcanic conduit itself, acts like a tube bell or flute, and harmonic overtones are produced by the multiple standing waves in the tube. Other models involve the resonance of gas-filled bubbles [Maryanto et al., 2008], or the vibration of the volcanic conduit

inside an annulus [Jellinek and Bercovici, 2011]. Another set of models utilizes the Dirac comb effect, in which the Fourier transform of a comb of evenly spaced, discrete pulses in time will produce evenly spaced harmonics in the frequency domain [mathematical details in the Appendix]. Often, non-linear fluid flow [Hellweg, 2000] or non-linear responses to fluid flow [Julian, 1994] are invoked as the source of these highly regular pulses. Each model has useful specific implications about conditions within the volcano, which are often difficult to constrain. A primary goal of this study is to identify the most plausible models that explain the observations of harmonic tremor from the 2009 eruption of Redoubt Volcano.

2. Gliding Harmonic Tremor

2.1. Summary of observations on Redoubt Volcano

Redoubt Volcano explosively erupted in March 2009 after 20 years of quiescence. Intermittent seismic activity began in January 2009, and some reports of degassing date back to July 2008 [Schaefer, 2011]. This behavior is in stark contrast to the mere 23 hours of pre-eruptive seismicity that heralded the 1989 eruption [Power et al., 1994]. The eruptive sequence began March 23, 2009, with a series of five major Vulcanian explosions spaced just over an hour apart. A second pulse of closely spaced explosions followed between March 26 and March 29, 2009, most of which were preceded by upward gliding harmonic tremor. The entire sequence lasted two weeks, consisted of more than eighteen Vulcanian explosions with plume heights ranging from 4 to 18.8 km, and culminated in a major dome collapse on April 4, 2009 [Bull and Buurman, 2013]. Figure 1 shows a timeline of the explosive events, their associated plume heights, and the

numbering scheme used to reference specific explosions of interest throughout this paper. A dome-building phase followed the last explosion, and began with unusually high extrusion rates [Bull et al., 2013; Diefenbach et al., 2013]. This phase lasted until July 2009, and was also accompanied by periods of harmonic tremor and drumbeat earthquakes [Buurman et al., 2013].

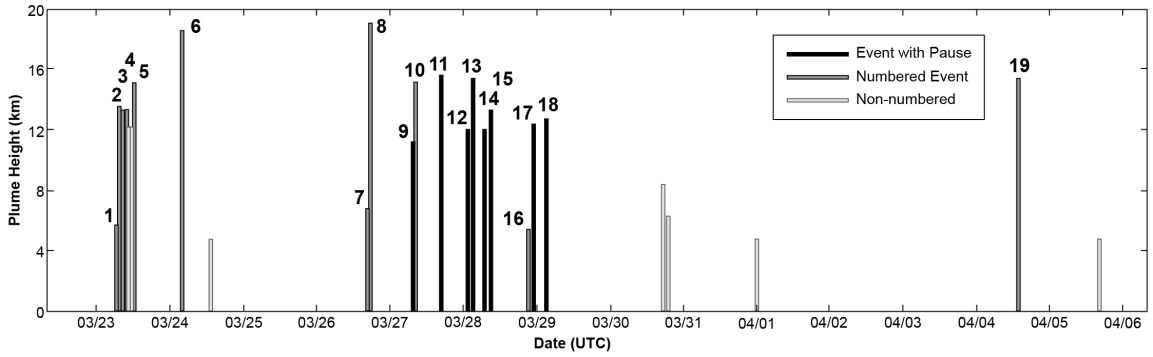

Figure 1. Timeline of explosive events during the 2009 eruption. Height of plume is from FAA Nexrad radar and/or USGS radar at Kenai [Ekstrand et al., 2013]. Events without numbers were identified upon reanalysis. Events preceded by a short silence are highlighted and discussed in later sections. After Schaefer [2011].

2.1.1. Seismic instrumentation

The Alaska Volcano Observatory (AVO) operates a permanent seismic network near Redoubt Volcano of one L22 and seven L4 short-period seismometers (Figure 2) [Dixon et al., 2010]. Of these stations, REF and RED are 3-component, and remaining stations have only a vertical channel. The existing network was supplemented by six Guralp CMG-6TD 3-component broadband seismometers. RDJH was installed on February 4, 2009, and RDW-B on February 24, 2009; both were telemetered. Additional campaign stations (RD01, RD02, RD03, and RDW-C) were deployed on March 21, 2009, during the pre-eruptive sequence. Actual station coverage during the entirety of the

eruptive sequence is poorer than the station map in Figure 2 implies. Both RSO and RDJH went offline on March 25, 2009, and RED was often saturated with noise. DFR is co-located with an acoustic microphone that recorded infrasound of the explosive events.

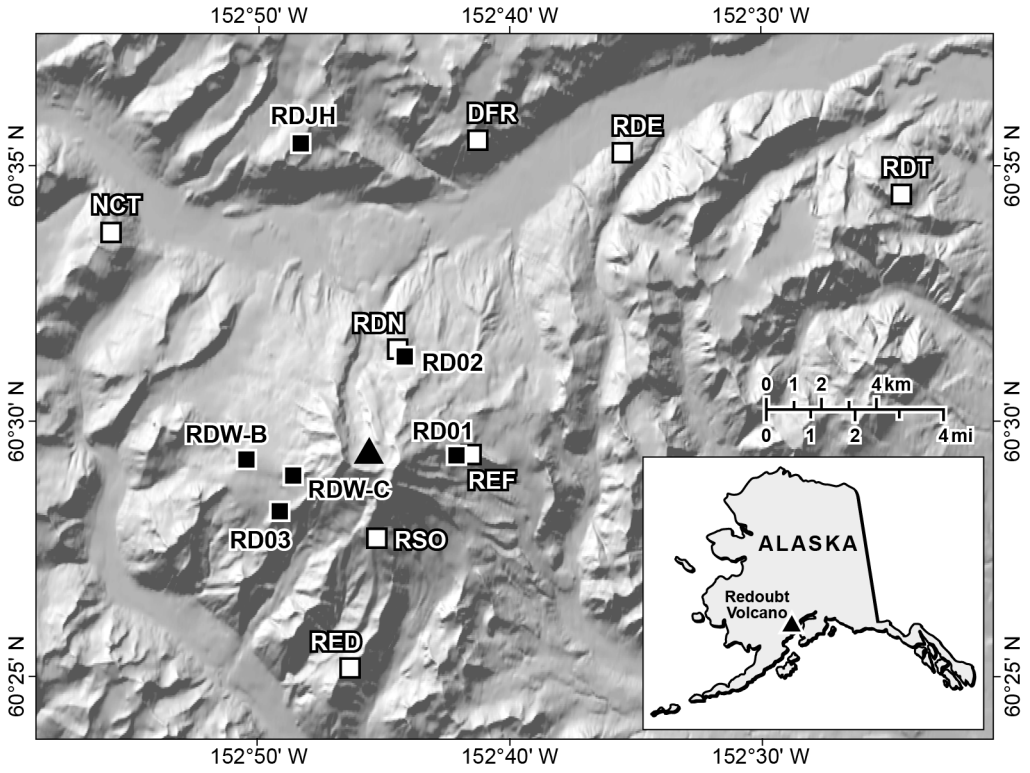

Figure 2. Seismic network map. The black triangle marks approximate location of the active vent and dome. White squares are permanent short-period stations, and black squares are broadband stations.

2.1.2. Seismic signal characteristics

The focus of our study is gliding harmonic tremor present immediately prior to six nearly consecutive explosions on March 27 and 28 (Figure 3), spanning Events 9 through 15. Many explosive events in the latter half of the eruptive sequence had a marked increase in seismicity in the minutes to hours before explosion, either as tremor

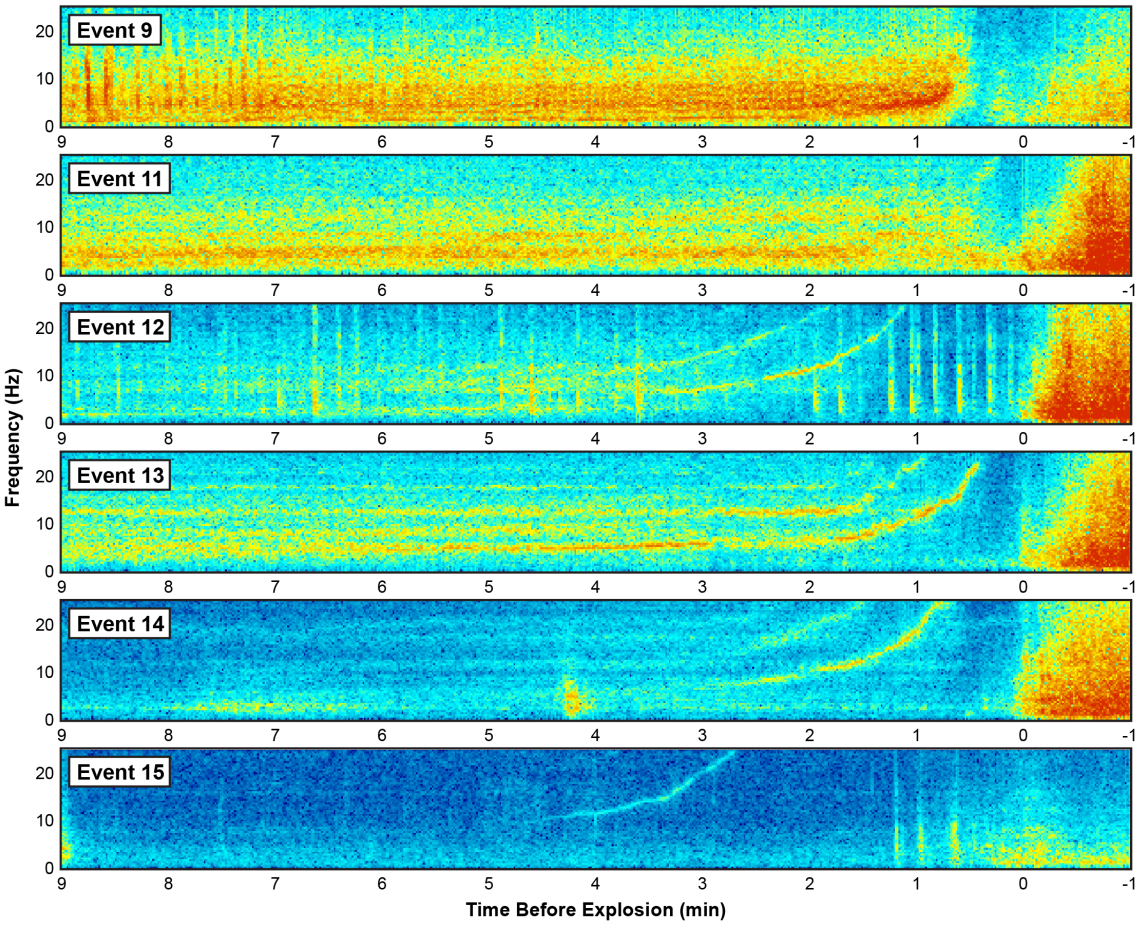

Figure 3. Velocity spectrograms of the pre-explosive gliding harmonic tremor on station RD01, to the east of the vent. All spectrograms are plotted on a common logarithmic color scale using a 2-second 50% overlapping window. Times are aligned to the approximate explosion onset at t=0, and frequency is plotted up to the broadband Nyquist frequency of 25 Hz. Bright vertical lines are earthquakes.

or earthquake swarms [Buurman et al., 2013] followed by a seismic quiescence, but only six show gliding clearly. Table 1 summarizes these observations for Events 9 through 18. Gliding tremor was recorded across the local network, and as far away as 90 km at both Spurr and Iliamna volcanoes for Events 9 and 13. Frequencies above 15 Hz were not recorded at more distant stations due to attenuation, but tremor frequencies approaching 20 to 25 Hz were apparent on multiple stations near the summit, and as high as nearly 30 Hz at short-period station REF. Despite these high frequencies, the same evolution of

harmonic tremor is seen on both campaign and telemetered stations, so we can rule out station noise and path effects as causes. Integer harmonic overtones exist for most events, but are usually weaker than the fundamental tone, and many events have only one overtone visible even at the closest stations. Harmonic tremor was never recorded infrasonically at DFR, but the associated explosions had energetic acoustic signals [Fee et al., 2013].

Event #	Date Time (UTC)	Plume Height (km asl)	Explosion Acoustic Onset	Lowest Harmonic Frequency (Hz)	Highest Harmonic Frequency (Hz)	Approx. Pre-explosive Quiescence (s)	Repeating earthquakes detected	Furthest distance recorded (km)
9	03/27 07:47	12.5	Emergent	0.8	10	30	Yes	86
11	03/27 06:39	15.6	Impulsive	?	30	15	Yes	22
12	03/28 01:34	14.6	Impulsive	0.5	28	70	Yes	22
13	03/28 03:24	15.2	Impulsive	2	23	30	Maybe	86
14	03/28 07:19	14.6	Impulsive	7	30	45	No	4
15	03/28 09:19	14.6	Impulsive	10	25	180	No	3
17	03/28 03:29	12.5	Impulsive	0.5	?	240	Maybe	22
18	03/29 03:23	14.6	Emergent	n/a	n/a	180	Yes	12

Table 1. Summary of Gliding Events. Plume heights from Bull et al. [2013]. Lowest frequency with harmonics visible using a 10-second, 50% overlapping FFT window on any station. Highest frequency observed on station REF. Quiescence measured from time of highest observed frequency to explosion onset on REF, and rounded to the nearest 5 seconds. Repeating earthquakes are considered present if they can be correlated via waveform cross-correlation. Furthest distance is measured from furthest station where tremor is visible to dome. For Event 18, this applies to visibility of repeating earthquakes rather than harmonic tremor.

Pre-explosive gliding occurs on consecutive explosions between Events 9 and 15, with the possible exception of Events 10 and 11. Event 10 occurred just a few minutes

after Event 9, so any gliding preceding this explosion might be buried in the previous explosion signal. Gliding prior to Event 11 is difficult to detect due to strong nonharmonic tremor that dominates the signal. Weak, upward gliding energy from 10 to 25 Hz exists across most of the network and up to 30 Hz at REF in the last two minutes before this explosion, followed by 30 seconds of relative quiescence. Because this behavior is generally consistent with the other events, we consider Event 11 to be part of the sequence.

The spectral evolution of gliding on Redoubt Volcano is reminiscent of, but at significantly higher frequencies than, pre-explosive gliding from 1 to 3 Hz on Montserrat in 1999 [Powell and Neuberg, 2003]. Over the six explosions, the fundamental tone spans the range of less than 1 Hz to upwards of 30 Hz, and changes by as much as 20 Hz in one minute. Both frequency range and rate of frequency change are similar for Events 12 through 15. Figure 4 illustrates the high degree of repeatability in time evolution of the fundamental spectral line for these events, as well as its similarity to the simple rational function $f=1/T$, where T is period, which is a linearly decreasing function of time. We also notice that harmonic tremor seems to start, or at least become visible, at higher frequencies for each new explosion. Due to low amplitudes at the highest frequencies, it is difficult to constrain how the highest frequency is changing from event to event.

After the tremor rises in frequency then fades, there is a quiet interval in the range of 15 to 270 seconds before an explosion. There is no consistent correlation between duration of the quiet time and either order of explosion, plume height, maximum frequency, or tremor amplitude. It is possible that the frequency of the tremor continues

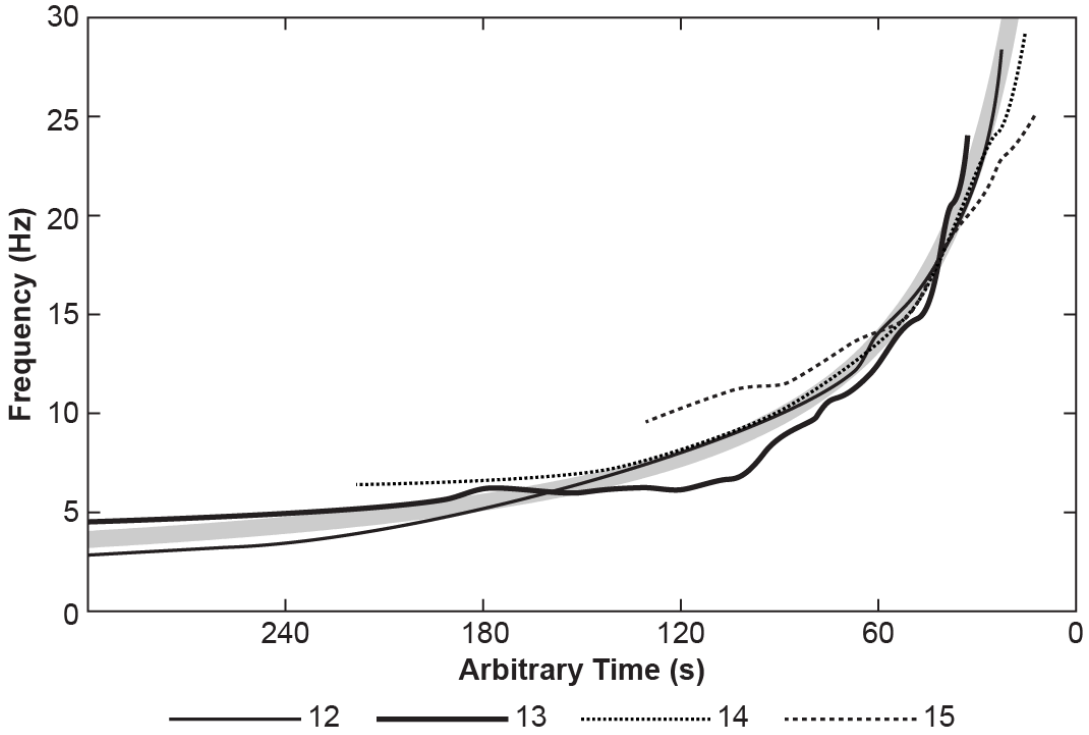

Figure 4. Fundamental frequencies of four consecutive gliding events plotted on an arbitrary time axis, so that they align at f=18 Hz. The lines are traced from a spectrogram of short period station REF, which has a Nyquist frequency of 50 Hz. The lines have repeatable shapes, though there is some variation in slope. Thick shaded line is a simple rational function, f=1/(-0.001t), where f is frequency (Hz) and t is time (s).

to climb unobserved, but because there is no evidence that is the case, we assume the interval is aseismic. Although they do not have the same dramatic gliding as earlier events, Events 17 and 18 also have similar quiet intervals prior to explosion. Harmonic tremor with fundamental frequency on the order of 0.5 Hz abruptly begins approximately 40 minutes prior to Event 17, but it eventually degrades into nonharmonic tremor that abruptly decays in amplitude immediately before the explosion. Small, increasingly frequent earthquakes that also abruptly stop precede Event 18. There is no clear silence before Event 16, 19, or any other previous explosion.

Because gliding tremor shares so many behavioral features among explosive events, we suspect a common, non-destructive source. Fundamental frequencies observed

as high as 30 Hz strongly constrain models to explain the tremor. Surprisingly, such high frequencies are not exclusive only to the explosive phase, as extended periods of high-frequency gliding were also observed beginning April 5, while the volcano was actively extruding a lava dome (Figure 5). During this time, the fundamental tone remained over 15 Hz for nearly twenty minutes in multiple instances, compared to just a few seconds prior to the explosions. The fundamental tone oscillates wildly, gliding both up and down in frequency, although there seems to be a preference toward downward gliding. Tremor continues sporadically in two- to three-hour bursts until April 10, 17:30 UTC, and is accompanied by continuous swarms of earthquakes.

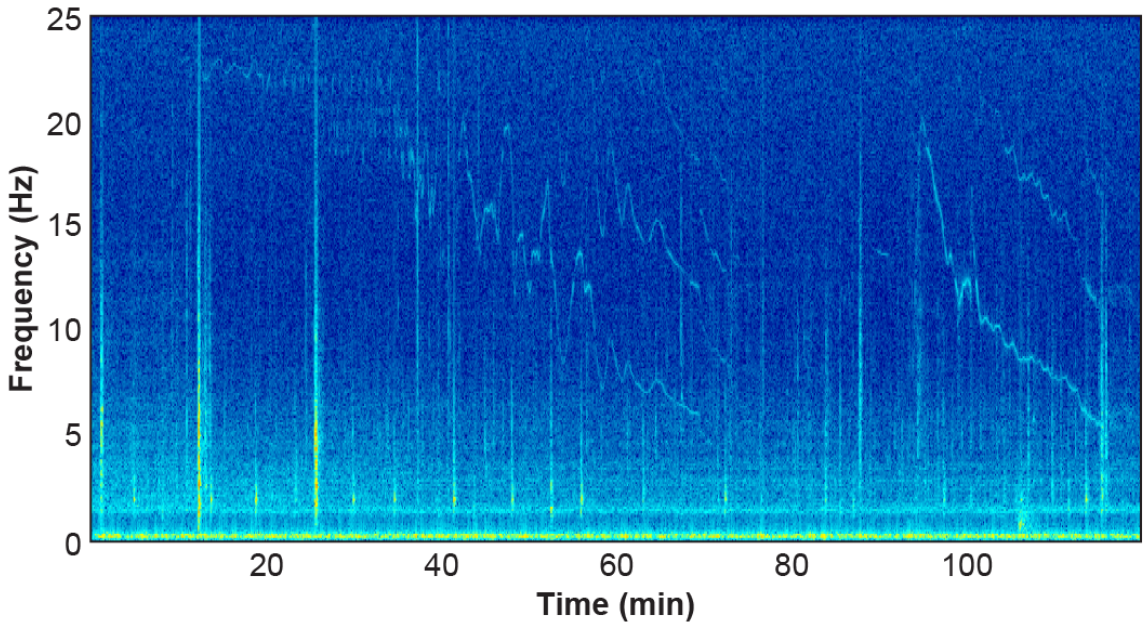

Figure 5. Two-hour representative sample of harmonic tremor on station RDW-C during the extrusive phase, beginning April 5, 2009 08:00 UTC. Spectrogram was made using a 10-second 50% overlapping sliding window, and is plotted on the same color scale as in Figure 3. Harmonic tremor with fundamental tones consistently above 5 Hz continued sporadically until April 10. This tremor was observed on several other stations in the network, both telemetered and untelemetered, but at lower amplitude.

Although the temporal behavior of extrusive-phase gliding is different than that of pre-eruptive gliding, the unusually high frequency content suggests that the same or similar source may be at work for both time periods. Therefore, we require a model that can produce harmonics with a fundamental frequency up to 30 Hz, permits the dominant frequency to change monotonically in a matter of minutes, can stably remain at high frequencies for extended periods of time, can survive or be easily reestablished between multiple explosions, and is seismically powerful enough to have harmonics be recorded at distances of 20 to 100 km. If possible, the model should permit conditions expected in both the pre-explosive and extrusive phases of volcanic activity.

2.2. Evaluation of models

Many explanations for the source of harmonic peaks in volcanic tremor invoke resonance of a fluid-filled pipe or crack, such as the volcanic conduit [Chouet, 1985; Benoit and McNutt, 1997; de Angelis and McNutt, 2007; Maryanto et al., 2008]. Gliding is attributed to changes in properties of a resonator, most often fluid acoustic velocity or effective resonator length [Neuberg, 2000; Jousset et al., 2003]. Although it is easy to visualize the rise and fall of a bubbly magma within the conduit as similar to a slide whistle, the excitation mechanism for the resonance itself is usually left unspecified.

Following these models we can calculate reasonable dimensions of the crack for a given frequency using the general equation for resonance of a tube with matched end conditions (open-open or closed-closed: $f=v/(2L)$, where f is frequency, v is acoustic velocity, and L is the length of the tube. The equation implies that if acoustic velocity alone changes, it must increase to 30 times its initial value for the case of Redoubt

Volcano's tremor. This range is roughly equivalent to the difference in P-wave velocity between air and the upper mantle, but could be feasible for acoustic velocities well below 1 km/s if two-phase flow is involved. Alternatively, if we assume that acoustic velocity remains constant at that of bubbly water or gas-rich magma (roughly 1 km/s, after modeling by Jousset et al. [2003]), a crack of 250 m length would produce 2 Hz harmonic tremor, and a crack of 16 m length would produce 30 Hz harmonic tremor. For Events 12 through 15, the crack must be consistently shortening at a rate of approximately 0.5 m/s, and perhaps closer to 2 m/s to reproduce the gliding at the end of Event 9. These lengths are for the matched end condition case; the lengths would be half as much for unmatched (open-closed) end conditions and produce only odd harmonics, which we do not observe. If we consider the resonating body to be the volcanic conduit, an acoustically impermeable layer, such as a bubble nucleation level, could be rising quickly and shortening the resonating portion of the conduit. Conversely, the resonating body could also be a thin hydrothermal crack that is collapsing on one or both ends, perhaps from increased pressure, and is then propped open again after each explosion [B. Chouet, personal communication, 2010]. Although we only present the end members, it is possible that a linear combination of change in acoustic velocity and length occurred simultaneously.

The magma wagging model of Jellinek and Bercovici [2011] also describes conduit processes, but the frequency of tremor depends primarily on the width and properties of the annulus surrounding the conduit. However, for realistic combinations of conduit geometry, the range for which magma wagging is viable is 0.1 to 5 Hz, which is well below the range of observed frequencies at Redoubt Volcano. The model also

requires the conduit to bend or other nonlinear effects to produce harmonic overtones [D. Bercovici and M. Jellinek, personal communication, 2011].

An alternative suite of models focuses on the flow of fluids through cracks. [Julian, 1994] proposes that harmonic tremor is a non-linear response to fluids flowing through constricted pathways, and that damping of the system will produce periodic oscillations. Alternatively, the harmonic nature of the signal could arise from constricted flow of the fluid itself, not unlike the whistle of a teakettle, with eddy shedding of steam being the most reasonable mechanism for our range of observed frequencies [Hellweg, 2000]. Choked flow of gas near the surface can be consistent with the seismic and acoustic observations of chugging [Johnson and Lees, 2000]. The choked flow mechanism might also be supplemented with feedback control through conduit resonance [Lesage et al., 2006]. These models have mostly been applied to chugging, or to extended periods of tremor around 1 Hz in frequency. All these theories imply that higher flow rates are required for higher frequencies, and are heavily dependent on assumptions about flow dimension and Reynolds number. For Redoubt Volcano, this implies that the extended periods of high frequency tremor represent extended periods of high velocity fluid flow. The lack of acoustic signal suggests the source may not be gas escaping at the surface, but does not exclude the possibility of flow deeper within the edifice. It may also be that flow is poorly acoustically coupled or that the signal to noise ratio for the single microphone is too high to detect the gas release.

While fluid flow and degassing are ways of generating highly regular pulses of seismic energy, they are not necessarily the only ways. For example, iceberg harmonic tremor is generated by repetitive stick-slip events as icebergs rub against each other in

collisions [MacAyeal et al., 2008] or against the sea floor in shoaling events [Martin et al., 2010]. The individual energy pulses are small, stick-slip icequakes, and the velocity of the drifting iceberg modulates the inter-event rate. Previous studies involving spectral character have indicated that low-frequency earthquakes and volcanic tremor may share a common source [Fehler, 1983]. The sources of low-frequency and hybrid earthquakes are often also closely linked to the influence of fluids [Chouet, 1988; Matoza et al., 2009]. Modeling has also indicated that at least some of the low-frequency content and spurious source mechanisms may be partly due to near-surface path effects [Malone and Haulter, 2003; Bean et al., 2008], and others have suggested brittle-failure as a mechanism [Iverson et al., 2006; Neuberg et al., 2006; Harrington and Brodsky, 2007]. Regardless of source, multiple observations exist of swarms of low-frequency earthquakes merging into tremor on Soufriére Hills Volcano, Montserrat [Neuberg et al., 1998; Neuberg, 2000], and Miyakejima Volcano, Japan [Fujita et al., 2009], and both in and out of tremor on Mount St. Helens, Washington [Malone and Qamar, 1984], and Augustine Volcano, Alaska [Power and Lalla, 2010]. The highly repetitive and periodic nature of some earthquake swarms, such as "drumbeat" swarms on Mount St. Helens [Moran et al., 2009], seem to mimic the periodic nature of harmonic tremor but at much slower rates.

3. Closely Repeating Earthquakes and Harmonic Tremor

A large swarm of repeating earthquakes preceded the first onset of harmonic tremor before Event 9 [Buurman et al., 2013]. While this observation alone is not extraordinary, we find that earthquakes comprising the swarm prior to Event 9 occur increasingly frequently as the time approaches the explosion, until they blend into

harmonic tremor. Event 11 also had a small swarm prior to nonharmonic tremor, and Event 12 had a swarm prior to and concurrently with harmonic tremor. The simplest hypothesis proposes that the earthquakes and tremor are related, and possibly even resulting from the same physical process.

The first test of our hypothesis is that the earthquakes all must originate from a single source. If the earthquakes were widely distributed in space, at each station the waveforms and arrival times would differ from earthquake to earthquake, and may be too irregular to form harmonics. However, if the earthquakes share the same location, timing will only depend on when the earthquakes actually occurred, and their waveforms will be highly similar if we assume they also share the same source mechanism. We measure waveform similarity using waveform cross-correlation, following previous studies that employed cross-correlation and multiplet analysis on volcanic earthquake swarms, especially those of low-frequency nature [e.g., Stephens and Chouet, 2001; Caplan-Auerbach and Petersen, 2005; Green and Neuberg, 2006; Umakoshi et al., 2008; Buurman and West, 2010; Thelen et al., 2010].

Of the earthquakes in the swarm preceding Event 9, 267 were large enough to be located with the permanent local network by AVO [Dixon et al., 2010]. We high pass filtered the seismograms from those earthquakes above 0.5 Hz to reduce microseism noise on the broadband stations, and then cross-correlated over a 15-second, amplitude-normalized window starting on the P-wave arrival. Approximately 95% of these seismogram pairs have normalized correlation coefficients greater than 0.85, and at least 75% correlate with coefficients in excess of 0.95. In fact, those earthquakes that do not correlate as highly generally contain more than one earthquake within this time window.

Closer analysis of broadband data revealed many additional earthquakes with visually similar waveforms that were missing from the AVO catalog. To make the catalog with repeating earthquakes from this family more complete, we used the largest earthquake on the vertical component of broadband station RDW-C as a template to find other similar earthquakes. We scanned the continuous data over a 3-second sliding window, and set the threshold for a potential match at a generous correlation coefficient of 0.5. This is a variation of a method used to find repeating long-period earthquakes prior to the 1989 eruption of Redoubt Volcano [Stephens and Chouet, 2001], and was also utilized for repeating coupled earthquakes at Shishaldin Volcano, Alaska [Caplan-Auerbach and Petersen, 2005], and repeating explosions of Pavlof Volcano, Alaska [Haney et al., 2009].

We found 1691 additional matches with correlation coefficients greater than 0.5, with 483 of these having coefficients greater than 0.75 during this swarm. The largest earthquakes correlate best with few exceptions. That is, as amplitude decreases, so too does the signal-to-noise ratio and correlation coefficient (Figure 6). We note that there is a bimodal amplitude distribution, with alternating large and small earthquakes that appear to be part of the same family. The detector only seemed to miss the smallest earthquakes for which only a small S-wave was visible, or when earthquake waveforms began to significantly overlap in the last hour leading up to the gliding. Between 5 and 50 additional matches, depending on coefficient cutoff and window size, were found within the harmonic tremor where the amplitude of individual events was large enough to overpower the harmonics. It is also worth noting that the amplitudes of the small earthquakes increase smoothly with time until they are consistent with the amplitude of

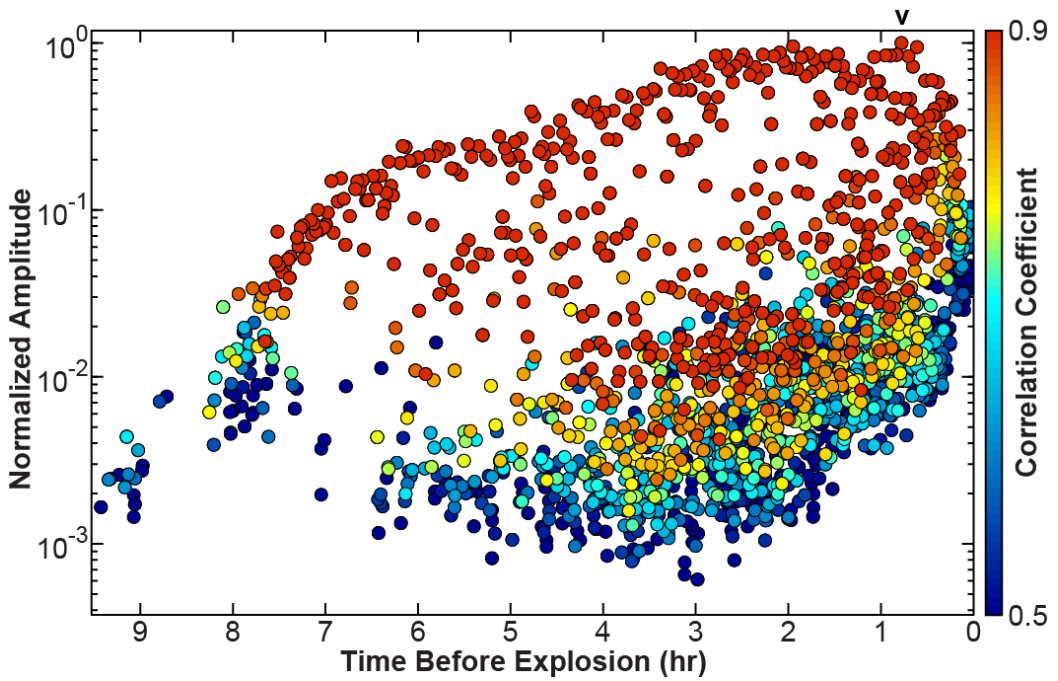

Figure 6. Normalized amplitude and correlation coefficient with respect to largest earthquake from before Event 9, marked with a 'v'. Amplitude is based on the maximum velocity amplitude of the S-wave, and is then normalized to the amplitude of the largest earthquake. Correlation coefficient is computed over a 3-second window beginning on the P-wave arrival. Longer window times do not significantly decrease the coefficient except where earthquakes begin to overlap. Color scale has been cropped between 0.9 and 0.5 to highlight the smooth gradient between correlation coefficient and amplitude. The relative amplitude of the subsequent harmonic tremor ranges from approximately $5x10^{-2}$ to $1x10^{-1}$.

the harmonic tremor. This detector was also applied to the earthquakes prior to Event 12, but we found a much more complicated time series with lower amplitudes and cross-correlation coefficients. Therefore, we focus on Event 9 because it has the clearest matches, and is the most temporally regular swarm.

A second test of our hypothesis is that the changing periodicity of the earthquakes should be compatible with the frequencies at which we observe tremor. That is, the inverse of the smallest inter-event period measurable from between earthquakes should be just slightly lower than the lowest fundamental frequency of the harmonic tremor. We

measured the P-wave arrival time for each earthquake at station RD01 through waveform cross-correlation of matched earthquakes down to a correlation coefficient of 0.5 over a 3-second window. RD01 was chosen for its clear, impulsive arrivals for both large and small earthquakes. First arrival times were supplemented in the last two hours by hand picks where we had reason to believe that the detector skipped an earthquake. Most of these missed earthquakes were buried in the surface waves of larger events or were small; they were objectively identified by simultaneously looking at a spectrogram, a high-pass filtered trace at 0.5 Hz, and a second high-pass filtered trace at 10 Hz. Where visible, the first P-wave motion was hand picked. In many cases, the P-wave was not clearly visible, but the S-wave arrival was. For these cases, we assumed the P-wave arrived 1 second before the S-wave. Hand picking became difficult around 20 minutes prior to explosion, where the time between earthquakes approached the time between the arrival of the P- and S-waves.

Figure 7 shows quantitatively how the timing between individual earthquakes decreases as a function of time. Although the timing errors in hand picked arrivals and skipped earthquakes increases with time in the sequence, the earthquakes seem to become more regularly spaced with time. The percent error in periodicity, defined as the standard deviation of the periodicity divided by the mean periodicity for a bin of 100 earthquakes, reaches a minimum at 25%, but likely overestimates the actual variation. Regardless of these errors, our measurements should still provide useful first-order estimates of the change in period with time. We sampled the fundamental frequency of the harmonic tremor during Event 9 from a spectrogram on the same station, and then plotted its inverse, or period, on the same axes as the earthquakes. The average inter-earthquake

time approaches the period of the tremor. Remarkably, a least squares linear trend of the inter-earthquake period has a slope of roughly -0.001 s/s, which is the same slope used to fit the period of gliding tremor from Events 12 through 15 in Figure 4.

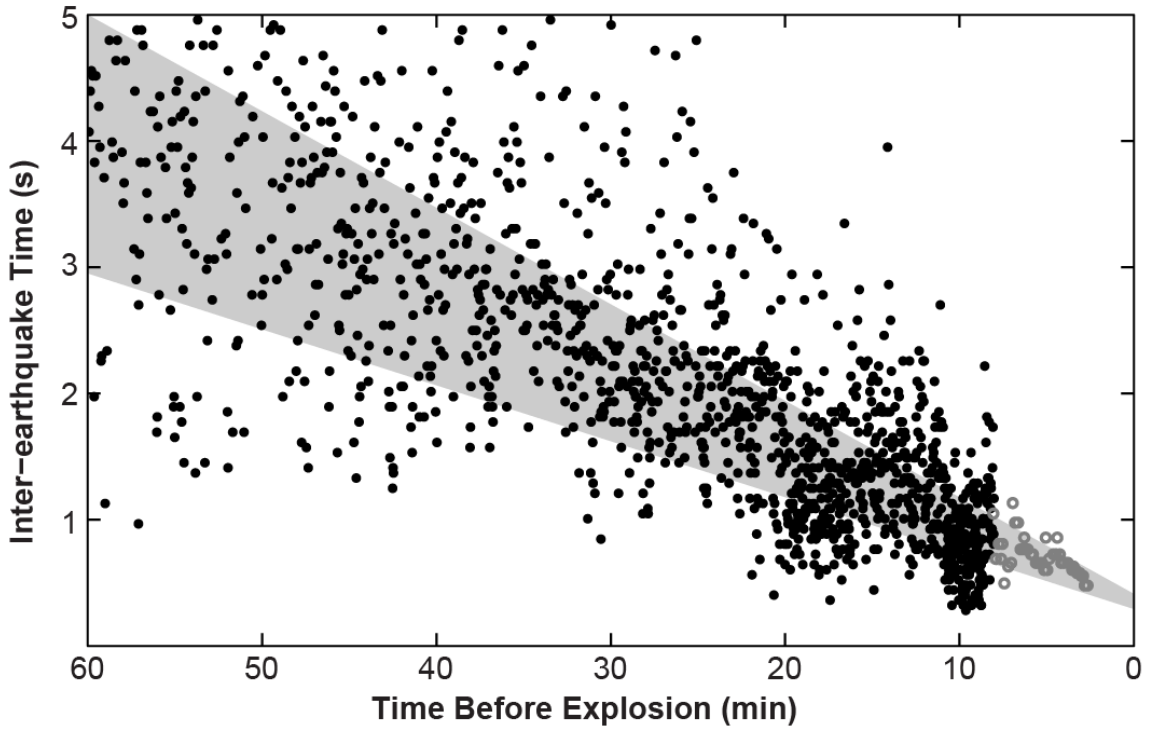

Figure 7. Change in period between earthquakes (black dots) and period of tremor (open gray circles) over the last hour leading up to Event 9, with least squares linear trend line fit to the full ten-hour swarm of slope -0.001 s/s and thickness 25% of period (bold gray line). Period of tremor was measured by taking the inverse of the frequency of the fundamental tone from Figure 3.

We further tested our hypothesis that the tremor is comprised of regularly repeating earthquake signals through a series of synthetic experiments. We verified that earthquakes that repeat with sufficient regularity could produce harmonics through the Dirac comb effect, in which frequency of the fundamental tone is inversely related to the timing between sources [Powell and Neuberg, 2003]. We summarize the mathematical underpinnings of this effect in the Appendix. [Powell and Neuberg 2003] state in a

similar analysis that in order to produce harmonics through the comb effect, the error in periodicity of the sources must be less than 2% to reproduce features of the tremor observed on Lascar, and [Hagerty et al. 2000] attest that the error must be less than 1% to reproduce the tremor on Arenal. Harmonic tremor at Redoubt had fewer overtones than Lascar and Arenal, so we reconsider the allowable variability in timing and amplitudes of repeating earthquakes necessary to be consistent with the tremor we observe.

We constructed synthetic harmonic tremor by convolving an earthquake from a swarm prior to Event 9 with a pulse train of linearly decreasing recurrence interval with time, from 0.4 to 0.02 seconds over 6 minutes (Figure 8). Variability in timing was included by adding Gaussian noise centered on the period between each earthquake, such that the percentage variation of interval remains constant despite changing frequency. We find for harmonic tremor with few overtones, as we see on Redoubt Volcano, that the period may vary by as much as 10% without destroying the first overtone, and by nearly 20% without destroying the fundamental tone. It is also important to note, especially for lower frequencies, that the choice of FFT window length affects the resolution of the harmonics. The spectrum becomes more peaked as more repeating pulses are included in the window, but becomes less harmonic if the time between these pulses changes sufficiently over the window.

We also evaluated the allowable variation in amplitude by adding Gaussian noise to the amplitude of the pulse train, and found that even 100% noise in amplitude does not significantly alter the harmonic nature of the signal. While we cannot separate individual earthquake signals during the interval in which we observe the harmonic tremor, the variability of the earthquake inter-event periods and amplitudes measured in the hours

leading up to the tremor decreases with time such that just prior to the tremor it is of the order of the 20% and 100% limits, respectively, inferred in our synthetic tests. Moreover,

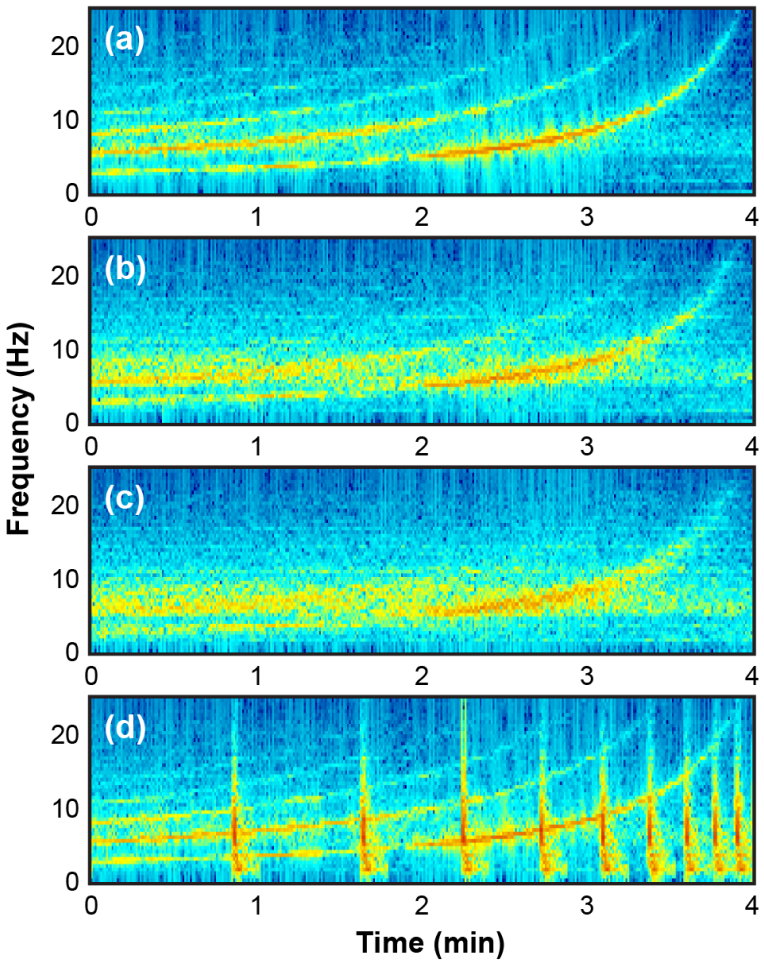

Figure 8. Synthetic harmonic tremor was made by convolving a comb function of linearly decreasing period with time and a sample earthquake from the Event 9 swarm on station RDW-C. Error in periodicity of the comb with standard deviation of (a) 5%, (b) 10%, and (c) 15% degrades the harmonic nature of the signal. Random amplitude variation did not significantly alter the signal, but a few significantly larger outliers of the same family, as in (d), creates the appearance of simultaneous earthquakes and harmonic tremor. Purely horizontal bands across the spectrogram match the source earthquake's spectrum. The weak fundamental tone between 1 and 2 min coincides with a trough in the earthquake spectrum, giving the illusion of a missing fundamental tone.

even for spectrograms constructed with longer windows we do not observe harmonics prior to the last few minutes. In other words, the synthetic tests are consistent with the observations. Physically they imply that in the hours leading up to the explosions the earthquakes occur both with increasing rate and regularity.

Our hypothesis that the tremor is comprised of repeating earthquakes also predicts that the two signals should also share the same spectral characteristics in the nonharmonic portion of the spectrum, since the total spectrum of tremor is the combination of the earthquake's spectrum and a comb [Garces and McNutt, 1997]. Thus, our third test makes an effort to compare the tremor spectrum with a single repeating earthquake's spectrum. Figure 9 shows the normalized spectrum of one of the repeating earthquakes with the average spectrum of ten minutes of harmonic tremor immediately prior to Event 9. We averaged the tremor spectra over a time period when the harmonic peaks change dramatically to let the nonharmonic character dominate the spectrum, even though harmonics are present in shorter time windows. In this case the tremor spectrum should simply be the sum of multiple copies of the spectrum of a single earthquake, and the comb effect is reduced because the time between copies is insufficiently regular over the longer time period. Although the relative amplitudes of spectral peaks are slightly different, the earthquake and tremor spectra share highly similar shapes across the network.

Given that the earthquakes in the swarm prior to Event 9 appear to merge into harmonic tremor, and may indeed comprise it, we investigated the possible source mechanism of these earthquakes by further analyzing the spectra of the signals they generate. We note that the spectral content of these earthquakes is rich in frequencies

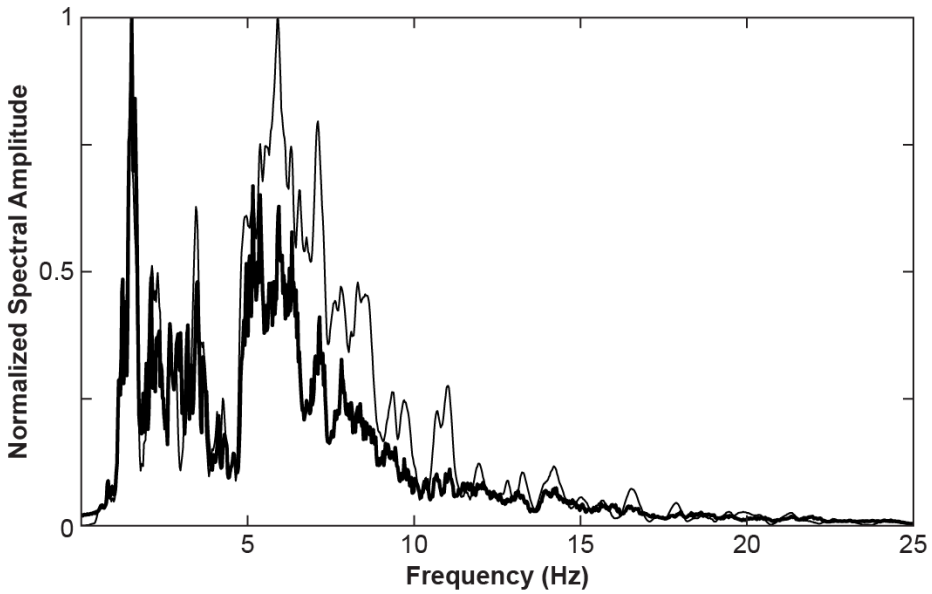

Figure 9. Normalized spectrum of a single repeating earthquake (thin line) vs. 10 minutes of tremor (thick line), both from prior to Event 9 on station RDW-C. Spectrum for the earthquake was calculated over a 30-second window, and the spectrum for tremor was averaged over 30-second long, 10-second overlapping sliding windows to enhance the nonharmonic part of the spectrum.

above 5 Hz, and that many stations located on the volcano proper have waveforms with clearly impulsive arrivals. Based on classification of volcanic earthquakes by [Lahr et al. 1994], these earthquakes most closely resemble shallow volcano-tectonic (VT) earthquakes. Often, VT earthquakes are attributed to brittle failure, and should theoretically have the same source spectra as non-volcanic earthquakes of the same size. Following Prejean and Ellsworth [2001], we computed fits of the P-wave spectra for large, similarly sized repeating earthquakes on multiple stations to both ω^2 and ω^3 source models [Brune, 1970] for a range of corner frequencies and seismic quality (Q) factor. Because uncorrected path effects may heavily contaminate spectra and because impulsive high-frequency earthquakes can have non-double couple moment tensors [e.g., Foulger et al., 2004], we use this analysis as a simple test to explore general consistency with the models, rather than to establish specific source parameters. Spectral fits were checked for

consistency across the network. We find the best fitting source spectra for these M_d 1.0 - 1.7 earthquakes are consistent with an ω^2-source model with a corner frequency above 20 Hz and Q between 6 and 30 depending on seismic station used. Unfortunately, there is a heavy tradeoff between corner frequency and Q, where lower Q will yield higher corner frequency. Q is not well constrained, though stations with consistently low-Q fits had broadband sensors installed temporarily on unconsolidated ash. Additionally, the Nyquist frequency for the broadband instruments is 25 Hz and the close short-period stations clipped on these earthquakes, so little reliable data are available to fully constrain the high corner frequencies one might expect for this magnitude range.

To further constrain the earthquake source properties, we stacked similar waveforms to resolve clear first motions on 12 stations, which included one station from both Spurr and Iliamna volcanoes, 90 km distant. First motions were mixed, with first compressional motion on stations to the north and east, and dilatational to the south and west (Figure 10). These mixed first motions contrast observations of repeating long-period earthquakes with all dilatational first motions during the previous eruption of Redoubt Volcano in 1989-90 [Chouet et al., 1994], and the 2004 eruption of Mount St. Helens [Matoza et al., 2009]. Fortuitously, many of the earthquakes in this swarm were large enough to be located, enabling us to solve for a focal mechanism. According to double difference relocations by Wessale et al. [2010], earthquakes in this swarm locate approximately 250 m WSW of the surface vent, roughly 300 m below sea level, and within 200 m of each other. We determined takeoff angles by assuming the average double-difference location and depth [Wessale et al., 2010], then traced rays through AVO's local 1-D velocity model for Redoubt Volcano [Dixon et al., 2010]. We first

solved for an initial double-couple fault plane solution with FPFIT [Reasenberg and Oppenheimer, 1985], and then further constrained the possible focal mechanism with P/S ratios for the closest stations using HASH v1.2 [Hardebeck and Shearer, 2002]. Table 2 lists the motions and P/S ratios used in this inversion. The resulting fault plane solution is close to pure dip-slip (Figure 10). However, although we can easily fit a double-couple mechanism to these earthquakes and the spectral fits are consistent with a double-couple mechanism, we do not have enough station coverage to perform a reliable full moment tensor inversion.

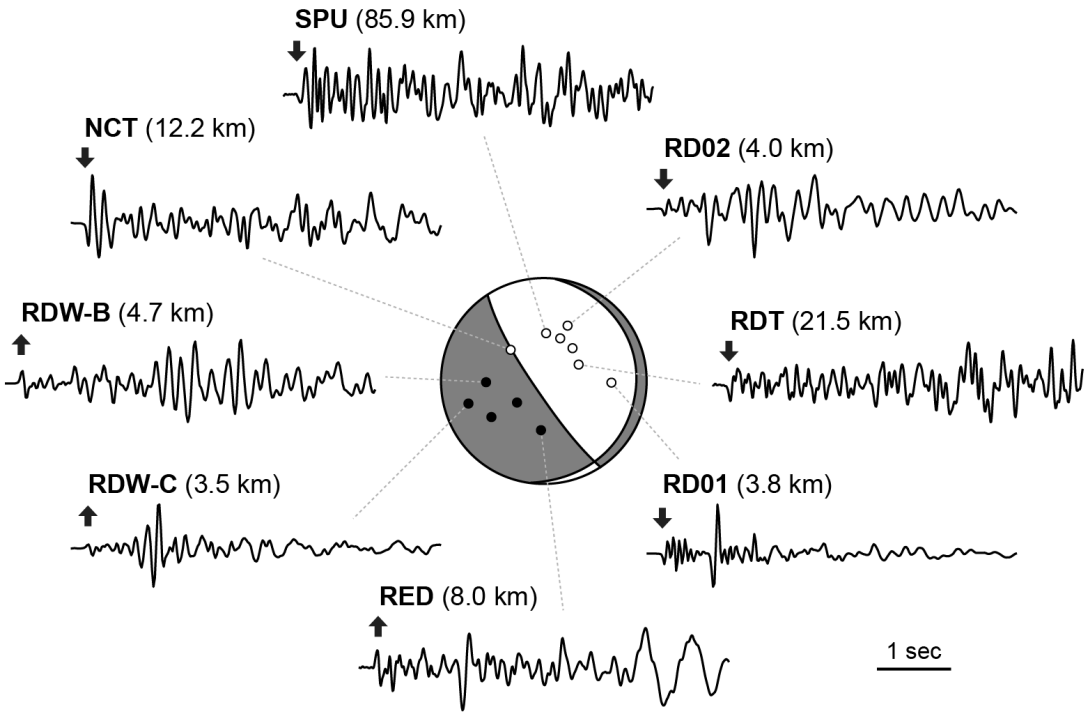

Figure 10. Stack of repeating earthquakes prior to Event 9 at multiple stations showing difference in first motions and character of signal with both distance and azimuth. Traces are 5 s long, and normalized to the same maximum amplitude. Respective first motions are plotted on the best fitting focal sphere constrained by both first motion and P/S ratio.

Station	First Motion	P/S Ratio
DFR	down	0.31
INE	up	-
NCT	down	1.70
RD01/REF	down	0.28
RD02/RDN	down	0.28
RD03	up	0.14
RDE	down	0.87
RDT	down	0.44
RDW-B	up	0.57
RDW-C	up	0.23
RED	up	0.53
SPU	down	-

Table 2. List of first motions and P/S ratios used in the determination of focal mechanism.

4. Discussion

We believe the best explanation for the observed gliding tremor at Redoubt Volcano is that it is composed of repeating earthquakes. We base this on observations of a smooth transition between the inter-event times of discrete earthquakes and frequency of harmonic tremor prior to Event 9, the similarity in spectrum of the tremor window and an earthquake, and the fact that we can reproduce all the features of the observations with synthetic time series. Although Event 9 has the clearest supporting evidence, it is possible to explain the behavior of the following explosions in terms of this model. For Event 11, the majority of the pre-explosive tremor is nonharmonic, with only faint high frequency gliding visible near the end. A small swarm of earthquakes is visible prior to tremor, but with less regularity than Event 9. Our model is consistent with this event if earthquakes comprising the tremor were too irregularly spaced in time to form harmonics until the end. Event 12 had a large swarm of repeating earthquakes prior to and concurrent with gliding up to the onset of explosion that at times would blend in and out of harmonic tremor if long enough windows were used. Like Event 9, there seems to be a bimodal amplitude distribution based on waveform cross correlations, with small, more frequent

earthquakes comprising tremor, and larger earthquakes of the same family individually visible. However, the behavior is much less regular in time than Event 9 for reasons we do not understand. Events 13 – 15 have few, if any, visibly repeating earthquakes. Thus consistency between our model and these events requires that the swarms become large enough to be detected when the inter-event rate is too high to see individual repeaters. The explosion associated with Event 16 had different acoustic character from the previous explosions [Fee et al., 2013], and we suppose that the source either did not have time to re-establish itself or was even destroyed in this event. Event 17 marks the return of repeating earthquakes and low-frequency harmonic tremor, but the signal eventually degrades into nonharmonic tremor. We interpret that the nonharmonic tremor is still composed of repeating earthquakes with irregular periodicity, as was possibly the case for Event 11. Event 18 has some repeating earthquakes that become more frequent, but do not become frequent enough to form harmonic tremor over our chosen window length before explosion. Finally, although frequency of tremor during the extrusive phase is considerably more variable with time than that of pre-explosive tremor, differences in behavior may be related to changes in extrusion rate [Diefenbach et al., 2013], eruptive style, or magma properties [Coombs et al., 2013] and subsequently on processes controlling earthquake repeat rate.

Proximity of repeating earthquakes to the inferred location of the conduit and high-angle faulting make a case for slip at or near the edge of the conduit wall. Stick-slip phenomena in the conduit have been attributed to cyclic eruptive activity [Denlinger and Hoblitt, 1999] and chugging [Ozerov et al., 2003], but these are on longer time scales than we observe. We suppose that slip in our case could represent brittle failure of

viscous magma at the conduit wall itself as the magma ascends, as has been proposed as a possible mechanism for hybrid and long period earthquakes [Iverson et al., 2006; Neuberg et al., 2006; Harrington and Brodsky, 2007]. Conceptually, as magma rises in the conduit, it cools near the top and along the edges, and may fracture under high enough strain-rate. [Tuffen et al., 2008] demonstrated this phenomenon for magma in the lab at 900 ºC, and showed that this fracture mechanism produces similar seismic signals as tectonic earthquakes. If we believe that our repeating earthquakes are similar to tectonic earthquakes of comparable size, the stressing rates required to have even a few earthquakes per second still seem abnormally high. It is possible that unusual material properties in the conduit region violate traditional assumptions about earthquake source mechanics such as stress drop. It is also unclear at this point exactly what force is causing the rate of occurrence to increase and become more regular immediately prior to these explosions. Acoustic character [Fee et al., 2013] and ashfall analysis [Wallace et al., 2013] of this subset of explosions indicates that the magma that erupted was possibly more viscous than in earlier explosions. Although viscosity may play a strong role in this model, there are many other variables that could conceivably control the rate of earthquake repetition, but a thorough investigation of these poorly constrained degrees of freedom is beyond the scope of this paper. However, it is clear that the process is repeatable between explosions, and returns when magma is extruded at the surface during dome building.

We infer that part of the repeatability between explosions has to do with the depth of the earthquakes, and therefore the harmonic tremor. Although the earthquakes are located near the conduit, they are relatively deep [Wessale et al., 2010]. When the

volcano erupts in a Vulcanian explosion, the conduit drains down the top 0.5 to 2 km [Druitt et al., 2002]. If we believe the earthquakes locate at 300 m below sea level, or roughly 3 km below the surface vent, the earthquake and tremor source would be well below the fragmentation front, and remain intact through the explosion. The process repeats again in similar fashion as the conduit refills, and conditions for failure are met.

A curious and significant detail we have not yet discussed is the nearly aseismic period between the highest frequency tremor and the onset of explosion. One could imagine that the frequency of the fundamental tone actually exceeds 30 Hz, and is attenuated away or too low in amplitude to be recorded. Although we could argue this may be the case for Event 12, where earthquakes occur even during the otherwise quiet pause, the earthquakes prior to Event 18 clearly cease three minutes before the explosion. Whether this cessation in seismicity is caused by a temporary transition from stick-slip to aseismic sliding, a pause in movement, or whether some other pre-explosive process is at work is still an open question.

Even though we have presented evidence to support the hypothesis that harmonic tremor is composed of repeating earthquakes, we are still left with several other important and unanswered questions regarding this model. For example, why are the repeat rates and tremor frequencies for Redoubt Volcano so much higher than other, similar volcanoes? For that matter, what stressing rate is required to produce upwards of 30 small earthquakes per second, and is that feasible to apply to both phases of eruption? Why is the decrease in the period between the earthquakes and the period of the harmonic tremor linear? Interestingly, the linearly decreasing period in harmonic tremor does not appear to be unique to Redoubt Volcano alone, as the upward gliding harmonic tremor from

Soufriére Hills Volcano also has a nearly linear shape when plotted in terms of period. Soufriére Hills Volcano also exhibited a linear increase in number of earthquakes over several swarms prior to dome failure [Hammer and Neuberg, 2009], which was proposed to be in line with the material failure law [Voight, 1988]. With more study, we hope similar observations of gliding tremor can be applicable to forecasting behavior of other volcanoes in the short term.

5. Conclusions

Redoubt Volcano produced repeatable, upward gliding harmonic tremor preceding six explosive events, for which the fundamental tone spanned from <1 Hz to 30 Hz. Harmonic tremor with fundamental frequencies consistently above 10 Hz returned for several hours during the early extrusive phase. This frequency range greatly exceeds other observations of harmonic tremor, and has implications for the applicability of previously proposed tremor sources that work in the 1 to 5 Hz range. We find that the most likely source of harmonic tremor for Redoubt Volcano is that of repeating earthquakes through the Dirac comb effect, based primarily on the observation of a smooth transition between the inter-event time of repeating earthquakes and fundamental period of harmonic tremor prior to Event 9. Further investigation into the source of these earthquakes points toward a shear source near the conduit, deep enough to survive a series of explosions. Although we do not have a complete explanation for why the earthquake rate speeds up and becomes more regular prior to explosion, we believe these observations can inform future studies of pre-explosive conduit dynamics.

Acknowledgements

We thank multiple AVO seismologists who first noted gliding tremor during the eruption, including Matt Haney and Glenn Thompson. We also thank John Power, Helena Buurman, Steve Malone, Cliff Thurber, Silvio de Angelis, Cyrus Read, Wes Thelen, Bernard Chouet, Michelle Coombs, and the rest of the AVO staff for useful discussions and assistance. The manuscript was greatly improved by thoughtful reviews by Jackie Caplan-Auerbach, Matt Haney, and an anonymous reviewer. A. Hotovec was supported by USGS ARRA funds for 3 months in 2010.

Appendix

A Dirac comb is an infinite series of evenly spaced Dirac delta functions in time, which has the special property that its Fourier transform is a comb function in frequency as well. The spacing of the delta functions in frequency is the inverse of the period between delta functions in time.

We can represent a comb function as a series of incrementally phase shifted delta functions:

$$g(t) = \delta(t) + \delta(t-\tau) + \delta(t-2\tau) + \cdots + \delta(t-N\tau) + \cdots \quad (1)$$

whose Fourier transform can be represented as a geometric series:

$$G(\omega) = 1 + e^{-i\omega\tau} + e^{-i\omega 2\tau} + \cdots + e^{-i\omega N\tau} + \cdots \quad (2)$$

Strictly speaking, a true comb function contains an infinite number of phase shifted delta functions. In practice, we only have a limited number of copies within a finite time window. Let us consider the case where we have only $N + 1$ pulses with period τ over the window $t = 0$ to $t = N\tau$. We can simplify the first $N + 1$ terms of a geometric series as:

$$G[r] = 1 + r + r^2 + r^3 + \cdots + r^N = \frac{1-r^{N+1}}{1-r} \tag{3}$$

where in our case:

$$r[\omega] = e^{-i\omega\tau} \tag{4}$$

By substituting Eq. 4 into Eq. 3, and using both Euler's formula ($e^{ix} = \cos x + i \sin x$) and the double angle formulae, we find that the spectrum of a sequence of $N + 1$ equally spaced delta functions is:

$$G(\omega) = e^{-\frac{1}{2}i\omega\tau} \frac{\sin\left(\frac{1}{2}\omega(N+1)\tau\right)}{\sin\left(\frac{1}{2}\omega\tau\right)} \tag{5}$$

The ratio of the two sin functions is essentially a periodic sinc function, with maxima where $(1/2)\omega\tau = \pi$. This occurs at integer frequencies $f = n/\tau$, the same as the true Dirac comb. Unlike the Dirac comb, the peaks of $G(\omega)$ have finite width, which can be approximated as $\Delta f \cong 1/[N\tau]$, and finite maximum amplitude $N + 1$. Clearly, the larger

N is [more repeats] the narrower the peaks become and the more harmonic the spectrum appears.

In our model, the repeating function is not a delta function, but a repeating earthquake. Thus, the total spectrum is the product of $G(\omega)$ and the spectrum of an earthquake. The harmonic frequencies of the spectrum are governed completely by the repeat interval, τ, but provide information about the earthquake spectrum where $G(\omega)$ is nonzero. It should be noted that earthquake spectra have finite bandwidths, typically decreasing with increasing frequency above some 'corner frequency' f_c. Finally, the harmonic nature of the signal may not be discernable for low values of N, even for perfectly timed repetitions, given the finite width and lower amplitude of the 'comb'.

References

Bean, C., I. Lokmer, and G. O'brien (2008), Influence of near-surface volcanic structure on long-period seismic signals and on moment tensor inversions: Simulated examples from Mount Etna, *J. Geophys. Res., 113,* B08308.

Benoit, J.P., and S. R. McNutt, (1997), New constraints on source processes of volcanic tremor at Arenal Volcano, Costa Rica, using broadband seismic data, *Geophys. Res. Lett., 24,* 449–452.

Brune, J. N. (1970), Tectonic stress and the spectra of seismic shear waves from earthquakes, *J. Geophys. Res., 75,* 4997–5009.

Bull, K., S. W. Anderson, A. Diefenbach, R. L. Wessels, and S. M. Henton, (2013), Emplacement of the final lava dome of the 2009 eruption of Redoubt Volcano, Alaska, *J. Volcanol. Geotherm. Res., Special Issue on the 2009 Redoubt Eruption,*

259, 334–348.

Bull, K., and H. Buurman (2013), An overview of the 2009 eruption of Redoubt Volcano, Alaska, *J. Volcanol. Geotherm. Res., Special Issue on the 2009 Redoubt Eruption, 259,* 2–15.

Buurman, H., M. E. West, and G. Thompson (2013), The seismicity of the 2009 Redoubt eruption, *J. Volcanol. Geotherm. Res., Special Issue on the 2009 Redoubt Eruption, 259,* 16–30.

Buurman, H. and M. West (2010), Seismic Precursors to Volcanic Explosions During the 2006 Eruption of Augustine Volcano, in *The 2006 Eruption of Augustine Volcano,* edited by J. A. Power, M. L. Coombs, and J. T. Freymueller, *Prof. Paper 1769,* chap. 2, pp. 41–57, U.S. Geol. Surv., Reston, Va.

Caplan-Auerbach, J., and T. Petersen (2005), Repeating coupled earthquakes at Shishaldin Volcano, Alaska, *J. Volcanol. Geotherm. Res.*, *145,* 151–172.

Chouet, B. (1985), Excitation of a buried magmatic pipe: a seismic source model for volcanic tremor, *J. Geophys. Res., 90,* 1881–1893.

Chouet, B. (1988), Resonance of a Fluid-Driven Crack: Radiation Properties and Implications for the Source of Long-Period Events and Harmonic Tremor, *J. Geophys. Res., 93,* 4375–4400.

Chouet, B. A., R. A. Page, C. D. Stephens, J. C. Lahr, and J. A. Power (1994) Precursory swarms of long-period events at Redoubt Volcano[1989-1990], Alaska: their origin and use as a forecasting tool, *J. Volcanol. Geotherm. Res., 62,* 95–135.

Coombs, M. L., T. Sisson, H. A. Bleick, S. Henton, C. Nye, A. Payne, C. Cameron, J. Larsen, K. Wallace, K. Bull, (2013), Andesites of the 2009 eruption of Redoubt

Volcano, Alaska, *J. Volcanol. Geotherm. Res., Special Issue on the 2009 Redoubt Eruption, 259,* 349–372.

de Angelis, S., and S. R. McNutt (2007), Observations of volcanic tremor during the January–February 2005 eruption of Mt. Veniaminof, Alaska, *Bull. Volcanol., 69,* 927–940.

Denlinger, R. P., and R. P. Hoblitt (1999), Cyclic eruptive behavior of silicic volcanoes, *Geology, 27,* 459–462.

Diefenbach, A. K., K. F. Bull., R. L. Wessels, and R. McGimsey (2013), Photogrammetric monitoring of lava dome growth during the 2009 eruption of Redoubt Volcano, *J. Volcanol. Geotherm. Res., Special Issue on the 2009 Redoubt Eruption, 259,* 308–316.

Dixon, J. P., S. D. Stihler, J. A. Power, and S. Searcey (2010), Catalog of earthquake hypocenters at Alaskan Volcanoes: January 1 through December 2009, U.S. Geol. Sur. Data Series 531 [http://pubs.usgs.gov/ds/531].

Druitt, T. H., S. R. Young, B. Baptie, C. Bonadonna, E. S. Calder, A. B. Clarke, P. D. Cole, C. L. Harford, R. A. Herd, R. Luckett, G. Ryan, and B. Voight (2002), Episodes of cyclic Vulcanian explosive activity with fountain collapse at Soufrière Hills Volcano, Montserrat, in *The eruption of Soufriére Hills volcano, Montserrat, from 1995 to 1999*, edited by T. H. Druitt, and B. P. Kokleaar, *Geological Society of London, Memoirs 21,* pp. 281–306.

Ekstrand, A. P., W. Webley, D. L. Nelson, M. J. Garay, J. Dehn, T. S. Steensen, K. D. Dean, and A. Prakash (2013), A Multisensor Plume Height Analysis of the 2009 Redoubt Eruption, *J. Volcanol. Geotherm. Res., Special Issue on the 2009 Redoubt*

Eruption, 259, 170–184.

Fee, D., S. R. McNutt, T. M. Lopez, K. M. Arnoult, C. A. Szuberla, and J. V. Olson (2013), Combining Local and Remote Infrasound Recordings from the 2009 Redoubt Volcano Eruption, *J. Volcanol. Geotherm. Res., Special Issue on the 2009 Redoubt Eruption, 259,* 100–114.

Fehler, M. (1983), Observations of volcanic tremor at Mount St. Helens volcano, *J. Geophys. Res., 88,* 3476–3484.

Foulger, G. R., B. R. Julian, D. P. Hill, A. M. Pitt, P. E. Malin, and E. Shalev (2004), Non-double-couple microearthquakes at Long Valley caldera, California, provide evidence for hydraulic fracturing, *J. Volcanol. Geotherm. Res., 132,* 45–71.

Fujita, E., M. Ukawa, E. Yamamoto, Y. Okada, and M. Kikuchi (2009), Volcanic Earthquakes and Tremors Associated with the 2000 Miyakejima Volcano Eruption, *Journal of Geography*, *110,* 191–203, in Japanese, with English Abstract.

Garces, M.A., and S. R. McNutt (1997), Theory of the airborne sound field generated in a resonant magma conduit, *J. Volcanol. Geotherm. Res., 78,* 155–178.

Green, D. N., and J. Neuberg (2006), Waveform classification of volcanic low-frequency earthquake swarms and its implication at Soufrière Hills Volcano, Montserrat, *J. Volcanol. Geotherm. Res., 153,* 51–63.

Hagerty, M. T., S. Y. Schwartz, M. A. Garcés, and M. Protti (2000), Analysis of seismic and acoustic observations at Arenal Volcano, Costa Rica, 1995–1997, *J. Volcanol. Geotherm. Res., 101,* 27–65.

Hammer, C., and J. W. Neuberg (2009), On the dynamical behaviour of low-frequency earthquake swarms prior to a dome collapse of Soufrière Hill volcano, Montserrat,

Geophys. Res. Lett., 36.

Haney, M. M., K. van Wijk, L. A. Preston, and D. F. Aldridge (2009), Observation and modeling of source effects in coda wave interferometry at Pavlof volcano, *The Leading Edge, 28,* 554–560.

Hardebeck, J. L., and P. M. Shearer (2002), A New Method for Determining First-Motion Focal Mechanisms, *Bull. Seismol. Soc. Am., 92,* 2264–13.

Harrington, R. M., and E. E. Brodsky (2007), Volcanic hybrid earthquakes that are brittle-failure events, *Geophys. Res. Lett., 34.*

Hellweg, M. (2000), Physical models for the source of Lascar's harmonic tremor, *J. Volcanol. Geotherm. Res., 101,* 183–198.

Iverson, R. M., D. Dzurisin, C. A. Gardner, T. M. Gerlach, R. G. LaHusen, M. Lisowski, J. J. Major, S. D. Malone, J. A. Messerich, S. C. Moran, J. S. Pallister, A. I. Qamar, S. P. Schilling, and J. W. Vallance (2006), Dynamics of seismogenic volcanic extrusion at Mount St Helens in 2004–05, *Nature*, *444,* 439–443.

Jellinek, A. M., and D. Bercovici, (2011), Seismic tremors and magma wagging during explosive volcanism, *Nature*, *470,* 522–525.

Johnson, J. B., and J. M. Lees (2000), Plugs and chugs--seismic and acoustic observations of degassing explosions at Karymsky, Russia and Sangay, Ecuador, *J. Volcanol. Geotherm. Res., 101,* 67–82.

Jousset, P., J. Neuberg, and S. Sturton, (2003), Modelling the time-dependent frequency content of low-frequency volcanic earthquakes, *J. Volcanol. Geotherm. Res., 128,* 201–223.

Julian, B. R. (1994), Volcanic tremor: nonlinear excitation by fluid flow, *J. Geophys.*

Res., 99, 11859–11877.

Lahr, J. C., B. A. Chouet, C. D. Stephens, J. A. Power, and R. A. Page (1994), Earthquake classification, location, and error analysis in a volcanic environment: implications for the magmatic system of the 1989-1990 eruptions at Redoubt Volcano, Alaska, *J. Volcanol. Geotherm. Res., 62,* 137–152.

Lees, J. M., J. B. Johnson, M. Ruiz, L. Troncoso, and M. Welsh (2008), Reventador Volcano 2005: Eruptive activity inferred from seismo-acoustic observation, *J. Volcanol. Geotherm. Res., 176,* 179–190.

Lees, J. M., and M. Ruiz (2008), Non-linear explosion tremor at Sangay, Volcano, Ecuador, *J. Volcanol. Geotherm. Res., 176,* 170–178.

Lees, J. M., E. I. Gordeev, and M. Ripepe (2004), Explosions and periodic tremor at Karymsky volcano, Kamchatka, Russia, *Geophysical Journal International, 158,* 1151–1167.

Lesage, P., M. M. Mora, G. E. Alvarado, J. Pacheco, and J. Métaxian (2006), Complex behavior and source model of the tremor at Arenal volcano, Costa Rica, *J. Volcanol. Geotherm. Res., 157,* 49–59.

MacAyeal, D.R., E. A. Okal, R. C. Aster, and J. N. Bassis (2008), Seismic and hydroacoustic tremor generated by colliding icebergs, *J. Geophys. Res., 113.*

Malone, S., and A. Haulter (2003), How glacier-quakes can mimic low-frequency volcanic earthquake seismograms, EGS-AGU-EUG Joint Assembly, VGP14-ITU2P-0255.

Malone, S.D., and A. Qamar (1984), Repetitive micro-earthquakes as a source for volcanic tremor at Mount St. Helens, EOS, Trans., Am. Geophys. Union 65, 1001,

Abstr.

Martin, S., R. Drucker, R. Aster, F. Davey, E. Okal, T. Scambos, and D. Macayeal (2010), Kinematic and seismic analysis of giant tabular iceberg breakup at Cape Adare, Antarctica, *J. Geophys. Res., 115.*

Maryanto, S., M. Iguchi, and T. Tameguri (2008), Constraints on the source mechanism of harmonic tremors based on seismological, ground deformation, and visual observations at Sakurajima volcano, Japan, *J. Volcanol. Geotherm. Res., 170,* 198–217.

Matoza, R. S., M. A. Garcés, B. A. Chouet, L. D'Auria, M. A. H. Hedlin, C. De Groot Hedlin, and G. P. Waite (2009), The source of infrasound associated with long-period events at Mount St. Helens, *J. Geophys. Res., 114,* B04305.

Moran, S. C., S. D. Malone, A. I. Qamar, W. A. Thelen, A. K. Wright, and J. Caplan-Auerbach (2008), Seismicity Associated with Renewed Dome Building at Mount St. Helens, 2004–2005, in *A Volcano Rekindled: The Renewed Eruption of Mount St. Helens, 2004–2006,* edited by D. R. Sherrod, W. E. Scott, and P. H. Stauffer, *Prof. Paper 1750,* chap. 2, pp. 27–60, U.S. Geol. Surv., Reston, Va.

Neuberg, J. (2000), Characteristics and causes of shallow seismicity in andesite volcanoes, *Phil. Trans. R. Soc. Lond. A, 358,* 1533–1546.

Neuberg, J., B. Baptie, R. Luckett, and R. Stewart (1998), Results from the broadband seismic network on Montserrat, *Geophys. Res. Lett.,* 25, 3661–3664.

Neuberg, J. W., H. Tuffen, L. Collier, D. Green, T. Powell, and D. Dingwell (2006), The trigger mechanism of low-frequency earthquakes on Montserrat, *J. Volcanol. Geotherm. Res., 153,* 37–50.

Ozerov, A., I. Ispolatov, and J. Lees (2003), Modeling Strombolian eruptions of Karymsky volcano, Kamchatka, Russia, *J. Volcanol. Geotherm. Res.*, *122,* 265–280.

Powell, T. W., and J. Neuberg (2003), Time dependent features in tremor spectra, *J. Volcanol. Geotherm. Res., 128,* 177–185.

Power, J. A., J. C. Lahr, R. A. Page, B. A. Chouet, C. D. Stephens, D. H. Harlow, T. L. Murray, J. N. Davies (1994), Seismic evolution of the 1989-1990 eruption sequence of Redoubt Volcano, Alaska, *J. Volcanol. Geotherm. Res., 62,* 69–94.

Power, J. A., and D. J. Lalla (2010), Seismic Observations of Augustine Volcano, 1970-2007, in *The 2006 Eruption of Augustine Volcano,* edited by J. A. Power, M. L. Coombs, and J. T. Freymueller, *Prof. Paper 1769,* chap. 1, pp. 1–38, U.S. Geol. Surv., Reston, Va.

Power, J. A., S. D. Stihler, B. A. Chouet, M. M. Haney, and D. M. Ketner (2013), Seismic Observations of Redoubt Volcano, Alaska—1989-2010 and a Conceptual Model of the Redoubt Magmatic System, *J. Volcanol. Geotherm. Res., Special Issue on the Redoubt Eruption, 259*, 31–44.

Prejean, S. G., and W. L. Ellsworth (2001), Observations of earthquake source parameters at 2 km depth in the Long Valley caldera, eastern California, *Bull. Seismol. Soc. Am., 91*, 165–177.

Reasenberg, P. A., and D. Oppenheimer (1985), FPFIT, FPPLOT, and FPPAGE: Fortran computer programs for calculating and displaying earthquake fault-plane solutions, U.S. Geological Survey Open-File Report 85-739.

Ripepe, M., D. Delle Donne, G. Lacanna, E. Marchetti, and G. Ulivieri (2009), The onset of the 2007 Stromboli effusive eruption recorded by an integrated geophysical

network, *J. Volcanol. Geotherm. Res., 182,* 131–136.

Rowe, C. A., R. C. Aster, P. R. Kyle, R. R. Dibble, and J. W. Schlue (2000), Seismic and acoustic observations at Mount Erebus Volcano, Ross Island, Antarctica, 1994-1998, *J. Volcanol. Geotherm. Res., 101,* 105–128.

Ruiz, M. C., J. M. Lees, and J. B. Johnson (2006), Source constraints of Tungurahua volcano explosion events, *Bull. Volcanol., 68,* 480–490.

Schaefer, J. R. G., ed., (2011), The 2009 Eruption of Redoubt Volcano, Alaska: Alaska Division of Geological & Geophysical Surveys Report of Investigations 2011-5. In press.

Schlindwein, V., J. Wassermann, and F. Scherbaum (1995), Spectral analysis of harmonic tremor signals at Mt. Semeru volcano, Indonesia, *Geophys. Res. Lett., 22.*

Stephens, C. D., and B. A. Chouet (2001), Evolution of the December 14, 1989 precursory long-period event swarm at Redoubt Volcano, Alaska, *J. Volcanol. Geotherm. Res., 109,* 133–148.

Thelen, W., M. West, and S. Senyukov (2010), Seismic characterization of the fall 2007 eruptive sequence at Bezymianny Volcano, Russia, *J. Volcanol. Geotherm. Res., 194,* 201–213.

Tuffen, H., R. Smith, and P. R. Sammonds (2008), Evidence for seismogenic fracture of silicic magma, *Nature, 453,* 511–514.

Umakoshi, K., N. Takamura, N. Shinzato, K. Uchida, N. Matsuwo, and H. Shimizu (2008), Seismicity associated with the 1991-1995 dome growth at Unzen Volcano, Japan, *J. Volcanol. Geotherm. Res., 175,* 91–99.

Voight, B. (1988), A method for prediction of volcanic eruptions, *Nature, 332,* 125–130.

Wallace, K., J. Schaefer, and M. Coombs (2013), Character, mass, distribution, and origin of tephra-fall deposits from the 2009 eruption of Redoubt Volcano, Alaska, *J. Volcanol. Geotherm. Res., Special Issue on the 2009 Redoubt Eruption, 259*, 145–169.

Wessale, M. S., J. D. Pesicek, E. M. Syracuse, C. H. Thurber, H. R. DeShon, J. A. Power, and S. G. Prejean (2010), Comparison of Seismicity Preceding the 1989-1990 and 2009 Eruptions of Redoubt Volcano, Alaska, Abstract S21B-2037 presented at 2010 Fall Meeting, AGU, San Francisco, Calif., 13-17 Dec.

CHAPTER 2:

A Continuous Record of Inter-eruption Velocity Change at Mount St. Helens from Coda Wave Interferometry

The content of this chapter was published in:

Hotovec-Ellis, A. J., J. Gomberg, J. E. Vidale, and K. C. Creager (2014) A continuous record of inter-eruption velocity change at Mount St. Helens from coda wave interferometry, *Journal of Geophysical Research Solid Earth,* 119, 2199–2214, doi:10.1002/2013JB010742.

Abstract

In September 2004, Mount St. Helens (MSH) volcano erupted after nearly 18 years of quiescence. However, it is unclear from the limited geophysical observations when or if the magma chamber replenished following the 1980-1986 eruptions, in the years before the 2004-2008 extrusive eruption. We use coda wave interferometry with repeating earthquakes to measure small changes in the velocity structure of Mount St. Helens volcano that might indicate magmatic intrusion. By combining observations of relative velocity changes from many closely located earthquake sources we solve for a continuous function of velocity changes with time. We find that seasonal effects dominate the relative velocity changes. Seismicity rates and repeating earthquake occurrence also vary seasonally; therefore, velocity changes and seismicity are likely modulated by snow loading, fluid saturation, and/or changes in groundwater level. We estimate hydrologic effects impart stress changes on the order of 10's of kPa within the upper 4 km, resulting in annual velocity variations of 0.5 to 1%. The largest non-seasonal

change is a decrease in velocity at the time of the deep $M_w = 6.8$ Nisqually earthquake. We find no systematic velocity changes during the most likely times of intrusions, consistent with a lack of observable surface deformation. We conclude that if replenishing intrusions occurred, they did not alter seismic velocities where this technique is sensitive due to either their small size or the finite compressibility of the magma chamber. We interpret the observed velocity changes and shallow seasonal seismicity as a response to small stress changes in a shallow, pressurized system.

1. Introduction

Mount St. Helens (MSH) is a dacite-andesite stratovolcano located in southwestern Washington State, famous for its massive explosive eruption in 1980. When it erupted again in late 2004, it did so with less than two weeks of warning, which took the form of vigorous shallow earthquake swarms [Moran et al., 2008; Thelen et al., 2008], GPS-measured deflation [Dzurisin et al., 2008; Lisowski et al., 2008], and visible deformation of the crater glacier [Dzurisin et al., 2008]. Petrologic studies of the eventually extruded magma found it was likely sourced near the top of the chamber (~5 km depth), largely degassed, and similar to but chemically distinct from previous eruptions. This evidence can be interpreted as either due to tapping of a geochemically-isolated region of the chamber, or mixing with a fresh supply of low-gas dacite from depth [Pallister et al., 2008]. It is not clear whether this magma was introduced into the system before the end of the last eruption in 1986, or if the magma chamber was replenished during the inter-eruptive period. Distinguishing which of these two processes occurred is important for anticipating what MSH, and volcanoes like it, may do in the

future.

There are limited geophysical data to constrain what occurred in the subsurface during the 18 years since the end of the previous dome-building eruption in late 1986 (Figure 1). A permanent GPS station installed at Johnston Ridge Observatory (JRO1, Fig. 2) in 1997 and radar interferograms [Poland and Lu, 2008] recorded no measurable deformation attributable to the volcano between at least 1992 and September 2004. Earlier trilateration and campaign GPS further concur that although some measurable inflation occurred between 1982 and 1991, no measurable surface deformation occurred after [Dzurisin et al., 2008]. However, lack of geodetic evidence does not exclude the

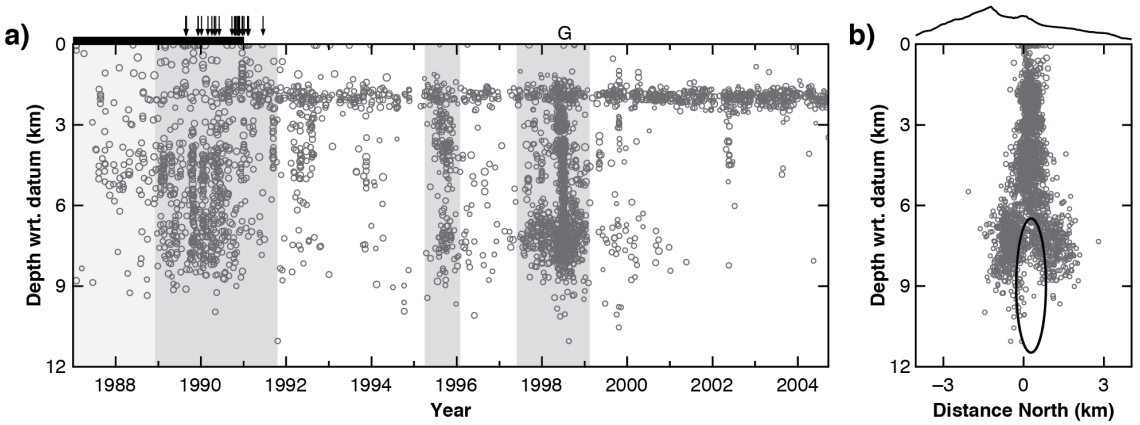

Figure 1: (a) Depth-time plot of well-located seismicity within 3 km of the dome (travel-time residual <.15 s, 8 or more phases used, azimuthal gap ≤90°, and closest picked station within 5 km); coda wave interferometry was performed on all earthquakes in the catalog regardless of magnitude or location quality. Times of observed deformation from line-length measurements (black bar), shallow explosions (arrows), and a gas emission (G) are also noted above the plot. Major swarms of deeper seismicity are highlighted in gray, and have been interpreted in other studies as a response to magmatic intrusions. (b) Depth cross-section through seismicity from south to north, centered on the dome. Depths are relative to a datum 1.1 km above sea level, which is the average elevation of stations in the seismic network near MSH; surface elevation of MSH is plotted above for reference. Hypocenters below 6 km surround an aseismic magma chamber, denoted by a black ellipse. The geometry of this chamber is the same used to model strain in Figure 11, from Lisowski [2006].

possibility that finite compressibility of the magma chamber could offset deformation due to an intrusion [Dzurisin et al., 2008; Mastin et al., 2008].

The most compelling evidence for magmatic intrusions during this time period is the occurrence of several deep (6 - 10 km depth) swarms of earthquakes [Moran, 1994]. The first burst of deeper seismicity occurred from 1987 to 1992. Focal mechanisms for these earthquakes were primarily strike-slip, but with P-axes inconsistent with the regional trend. Moran [1994] modeled these focal mechanisms as an increase in pressure within a cylindrical magma chamber, and interpreted the pressurization as being due to the sealing of the shallow conduit system, trapping exsolved magmatic gasses. During this time, there was also a series of shallow gas explosions following rain and/or snow storms, interpreted as the explosive release of these trapped gasses when water penetrated a low permeability cap [Mastin, 1994]. Two more bursts of deep seismicity occurred from 1994 to 1995 and from 1997 to 1998. Several fixed-wing gas flights were flown between June and September 1998, when seismicity was at its peak. The first flight recorded gas emissions of 1,900 t/d of CO_2, but the subsequent flights recorded only trace amounts or 0 t/d [Gerlach et al., 2008]. Focal mechanisms of the deeper seismicity suggested another increase in pressure within the magma chamber. Hypocentral relocations of the seismicity by Musumeci et al. [2002] revealed that a large number of deeper earthquakes occur on at least two NE-SW striking, steeply dipping faults rather than being distributed around the chamber. They further suggested that the southeastern fault had slip consistent with magma being periodically injected into a truncated dike on the northwest side of the fault (i.e., right-lateral motion to the north of the chamber, left-lateral to the south as the chamber expands).

The state of the shallow subsurface is also relevant, as the overwhelming majority (>99%) of seismicity leading up to and during the 2004-2008 eruption occurred above 4 km depth [Moran et al., 2008] and the eruption itself was potentially influenced by an abnormally wet late summer [Scott et al., 2008]. The aforementioned shallow explosions from 1989 to 1991, which often also followed intense rainfall events, and shallow (<4 km depth), seasonally modulated [Christiansen et al., 2005] seismicity suggest the system above the magma chamber was also pressurized long before 2004, and sensitive to the influx of water and/or other small pressure perturbations of 10's of kPa. Focal mechanisms of these shallow earthquakes further suggest a complex stress regime best explained by localized increases in pore pressure from water and/or magmatic gases [Lehto et al., 2013].

In this study, we use coda wave interferometry (CWI) of repeating earthquakes at MSH to measure small changes in seismic wave speed in an attempt to better resolve the timing of magma injection and the pressurization of the magmatic system, as well as the evolution of the shallow (<4 km) subsurface, including the conduit. Small (<1%) changes in seismic velocity have been observed at a handful of other volcanoes prior to eruptions [Ratdomopurbo and Poupinet, 1995; Wegler et al., 2006; Brenguier et al., 2008a], during intrusive events [Ueno et al., 2012], in response to large earthquakes [Battaglia et al., 2012], and changes in groundwater hydrology [Sens-Schönfelder and Wegler, 2006]. These observations and laboratory results [Grêt et al., 2006] suggest seismic velocity, in particular S-wave velocity [Snieder, 2002], is sensitive to deformation and the opening/closing of cracks due to changes in stress, fluid saturation, and temperature.

2. Data

Figure 2 is a map of the local seismic network surrounding Mount St. Helens between January 1987 and September 2004. We use earthquakes that have epicenters and horizontal location uncertainty within 3 km of the volcano's summit (i.e., a 3.4 km distant earthquake with 0.5 km horizontal uncertainty would be included) and depths between 0 and 12 km relative to the datum of the local velocity model, approximately 1.1 km above sea level (Figure 1b). This area comprises the majority of located seismicity in the MSH vicinity related to the volcano. Seismicity beneath the volcano between 1 and 4 km depth is persistent across the nearly 18-year time span, whereas seismicity between 4 and 10 km mostly occurred in the three large swarms (Figure 1a). The earthquakes that we use in

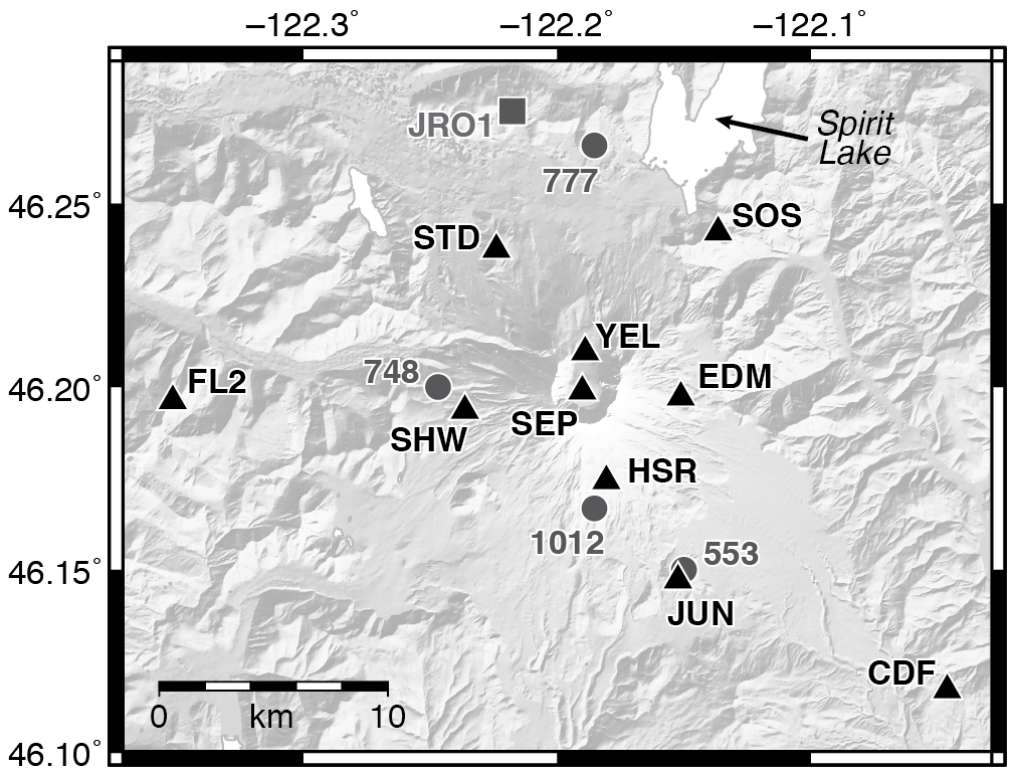

Figure 2: Map of GPS station JRO1 (gray square), SNOTEL stations (gray circles), and seismic network (black triangles) around Mount St. Helens. Seismic instruments are primarily L4 geophones, except HSR and CDF, which are S-13 geophones.

this study are cataloged and located by the Pacific Northwest Seismic Network (PNSN), using a network of Mark L4-C and Geotech S-13 single component, short-period, analog instruments operated by the PNSN and Cascades Volcano Observatory (CVO). During this time the network configuration changed little, but instruments and VCO units were often replaced as part of normal station maintenance. Data from these stations were telemetered by radio to the PNSN in Seattle, WA. Until January 2002, only triggered data were saved, limiting the ability to study this time period with continuous methods such as ambient noise interferometry.

3. Application of Coda Wave Interferometry

Seismic velocities are dependent on the physical properties of the materials through which the seismic waves travel, so that changes in these properties will produce a change in wave speed. Recent advances in theory and signal processing have allowed seismologists to observe small spatiotemporal changes in seismic velocities on the order of less than 0.1% by capitalizing on signals ordinarily discarded as noise. One technique for identifying velocity change is coda wave interferometry (CWI), wherein the codas of repeating earthquakes (also called repeaters, families, doublets or multiplets) are compared. CWI operates under the theory that the seismic coda of two co-located earthquakes is a summation of multiply scattered waves, and small changes in either the source or medium will affect how the scattered waves sum at the station and therefore alter the resulting waveform [e.g., Snieder, 2006]. The coda responds in distinct and predictable ways to different kinds of changes in the medium. For example, consider a

widespread and uniform decrease in wave speed that occurs between the times of two co-located earthquakes with the same focal mechanism. Coda waves from the second earthquake will arrive with increasing delay as the waves travel a longer effective distance through the slower medium by multiple scattering [e.g., Grêt et al., 2006]. CWI measures an apparent velocity change, which is the average relative velocity change in the volume through which the coda waves propagate. It provides a lower bound on the maximum change, especially if the change is concentrated and compact. In the case of a localized change, coda waves are most sensitive to velocity perturbations in an ellipse with foci at the source and receiver locations, but then increasingly less sensitive outside of that depending on the strength of scattering, frequency, and time lag [Pacheco and Snieder, 2005].

A change in seismic velocity is distinguishable from a change in source location, source mechanism, or scatterer location in that these other types of changes do not produce increasing lag with time for coda waves [Snieder, 2006]. For example, a change in location will alter coda wave paths, lengthening some and shortening others, but on average the travel-times will be the same, and the slope of lag with time will be zero. Although on average the slope from these other changes will be zero, they still alter the waveform and introduce uncertainty in the calculation of relative velocity change difference between earthquake pairs.

CWI is ideally suited for use in volcanic settings because repeating earthquakes are commonplace at volcanoes [e.g., Thelen et al., 2011], sometimes even during non-eruptive phases [Saccorotti et al., 2007; Petersen, 2007; Carmona et al., 2010; Massin et al., 2013], and the heterogeneity of the subsurface provides ample scattering. To find

pairs of repeating earthquakes at MSH, we cross-correlate the entire 18-year catalog of 1-10 Hz band-passed waveforms on individual stations in a window 0.1 s before to 2.4 seconds after the analyst-picked P-wave arrival, or the expected P-wave arrival based on the locations of the earthquake and station in the absence of a pick. For each individual station, if the waveforms in this window correlate above a normalized cross-correlation coefficient (CCC) of 0.8, we consider the two earthquakes to be a possible repeating pair and realign the waveforms to the time of maximum correlation. Using these parameters, we find that earthquakes with at least one matching event account for approximately 40% of the catalog, with time gaps between some pairs of up to 10 years, but on average one year or less.

We then process each pair of repeating earthquakes using the doublet method of Snieder et al. [2002] to determine velocity changes. For each pair of repeating events we divide the two waveforms into non-overlapping windows of 0.5-s length and calculate the CCC and lag for each window. We calculate the expected S-wave arrival based on the earthquakes' location using the "S3" PNSN 1-D velocity model and $V_p/V_s = 1.78$, and only consider windows after that arrival as being part of the coda. If there are at least five windows in the coda that have CCC above 0.65, we fit a straight line to those lags (Figure 3). The slope of this line defines the relative velocity change, under the assumption that the change occurs uniformly throughout the entire contributing volume [Snieder, 2006]. This method is limited to velocity changes less than ~2 or 3%, as greater lags will reduce more windows below our 0.65 CCC cutoff. Clipping may also reduce the CCC, but only affects a small portion of our dataset. We also attempt to account for slight differences in location of scatters, hypocenter, focal mechanism, and/or magnitude between the two

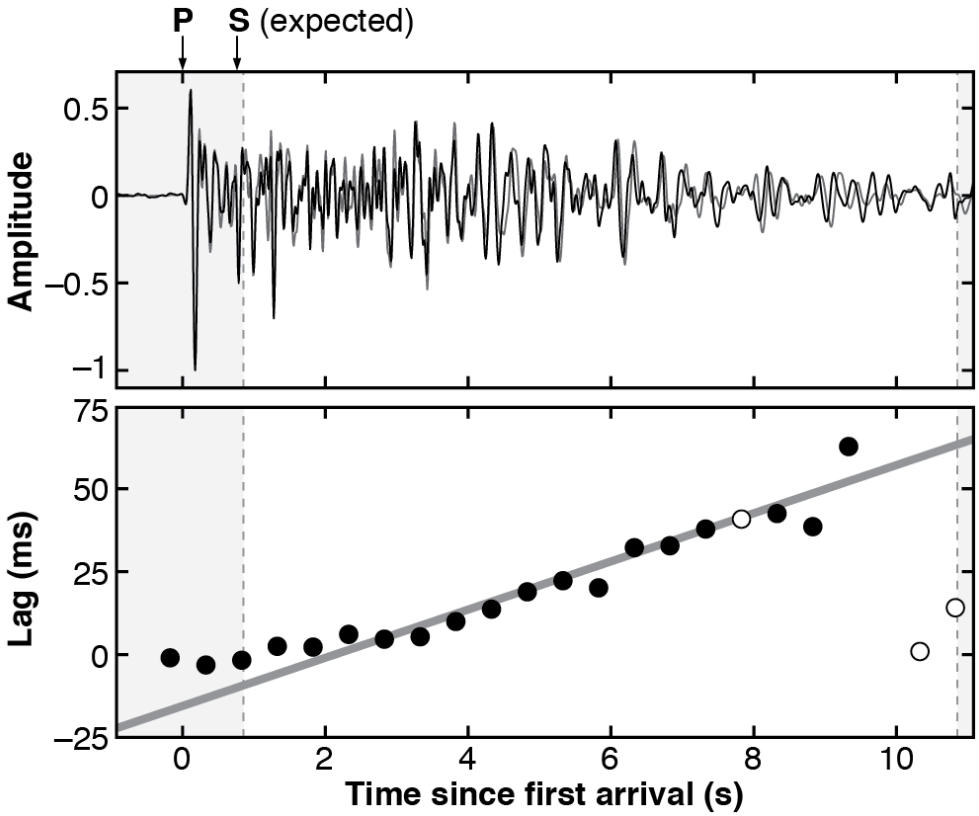

Figure 3: Top: example of two earthquakes recorded at HSR that correlate well in the early waveform, but decorrelate in the coda. S-wave was not picked on either earthquake, so expected arrival time to station is estimated using the PNSN S3 velocity model. Bottom: lag and similarity of black to gray waveform within non-overlapping, 0.5 second windows, plotted as circles at the center of the time window and lag time to maximum correlation. Unshaded region between dotted lines denotes time window used to calculate slope of lags for velocity measurement, unfilled circles indicate windows where the CCC was below the 0.65 cutoff and were not used to determine slope. This slope corresponds to a relative decrease in velocity of 0.68%.

earthquakes [e.g., Kanu et al., 2013] by only keeping pairs where the slope is well resolved and the standard deviation of the lags to the linear regression is less than 0.01 s. Although in theory the technique is precise to 0.01 or 0.02%, we estimate our error for any given pair is closer to 0.1%. This is based on the standard deviation of velocity changes for pairs less than 10 days apart, where we expect the change on this time scale to be close to zero. This process is repeated for all possible earthquake pairs for each

station out to 15 km distance from the summit of MSH.

Using the above procedure, we calculated relative velocity changes for thousands of event pairs separated by days to years. In reality, the relative velocity change is a function of both time and space, but at MSH we do not have the network density to fully resolve the spatial extent of our observed velocity changes. Therefore, in this paper we only solve at each station for the average velocity change with time within the volume through which the coda waves travel. Because different families of earthquakes occur near each other (within a few kilometers or less) and sample much of the same volume, we combine observations from many nearby earthquakes into a single velocity-change chronology.

Relative velocity changes are often compared for pairs of doublets across an abrupt known geophysical event, such as a large earthquake [Poupinet et al., 1984; Nakamura et al., 2002; Pandolfi et al., 2006; Li et al., 2007; Rubenstein et al., 2007; Battaglia et al., 2012]. In this paper we instead assume that there is some continuous function of velocity with time, and that each pair of earthquakes is sampling the difference between the velocities at those two times. We solve for the continuous function of velocity change that fits all the pairs of observed differential changes by a simple linear least-squares inversion. The forward problem for any pair of earthquakes at times t_i and t_j is simply:

$$d_{ij} = \gamma(t_j) - \gamma(t_i) \tag{1}$$

in which d_{ij} is the observed relative velocity change and $\gamma(t)$ is the continuous function of relative velocity change with time for which we intend to solve. We discretize the function $\gamma(t)$ evenly in time with a spacing of once every 10 days, i.e., the shortest

amount of time we allow velocity to change over, and linearly interpolate the function between each point. Therefore:

$$\gamma(t_i) = \gamma(t_k) + (\gamma(t_l) - \gamma(t_k))\frac{t_i - t_k}{t_l - t_k} \quad (2)$$

where k and l are the indices of γ on either side of t_i. Solving for γ is highly unstable because the problem is ill-conditioned, so we are forced to regularize the inversion. We have chosen a combination of first- and second-order Tikhonov regularization (i.e., minimizing the first and second derivatives of the solution to favor a solution that varies slowly and smoothly) with equal weight, and choose the solution with the best tradeoff between roughness and misfit. Additionally, the mean is set to zero to further stabilize the inversion, as there is no constraint on the absolute velocity.

4. Inversion Results

Before we apply the inversion to real data, we can test how well it can resolve known functions of velocity change given the uneven sampling times from our real data. We have tested how well the inversion resolves no change, a linear increase, a series of step functions, and a sinusoidal function in the presence of Gaussian noise with standard deviation of 0.1%, our calculated error. Figure 4 shows what kinds of changes are resolvable when sampling a known continuous function at the times of earthquake pairs at station HSR, which has an average number of pairs but highly uneven sampling with time (i.e., repeating earthquakes occur more commonly during autumn than spring, discussed later). The primary discrepancies between the known input and the inversion result occur for times when the data are sparse, as expected. For this level of noise, the minimum resolvable step in velocity is ~0.2% and the minimum resolvable slope is

~0.01%/year. Sinusoidal signals are well-resolved where there are data, and are not an artifact of uneven earthquake repetition.

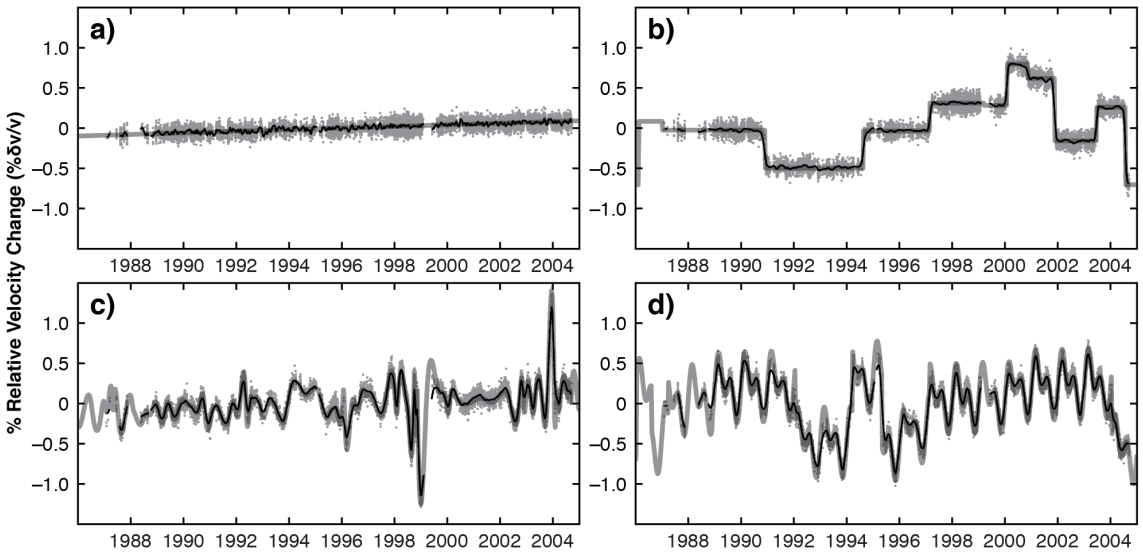

Figure 4: Tests of how well our inversion is able to recover a known function of velocity change (gray line) in the presence of Gaussian noise with standard deviation 0.1% dv/v and using the distribution of pairs at station HSR. The inverted solution (black line) has the best tradeoff between misfit and smoothness. Part (a) is a slope of 0.01%/year with no other changes, (b) is a series of small step functions, (c) is a random spline function, and (d) is the sum of two sinusoids (periods of 0.5 and 1 year) and a different series of step functions function than (b). Raw data points are plotted around the solution in gray.

For the first inversion involving real data, we incorporate only pairs with depths less than 4 km, which is where most seismicity occurs and we can expect good temporal resolution. Figure 5 shows the result of the inversion for the six most densely sampled and reliable stations. Although there are some time periods during which the solution is not well-resolved, there is a strong annual cyclicity in the relative velocity change for most of the stations. The Fourier transform of the velocity change on the nearest four stations has a strong peak near 365 days, with a secondary peak around 183 days, indicating that the changes are seasonal. Since we are more interested in velocity changes

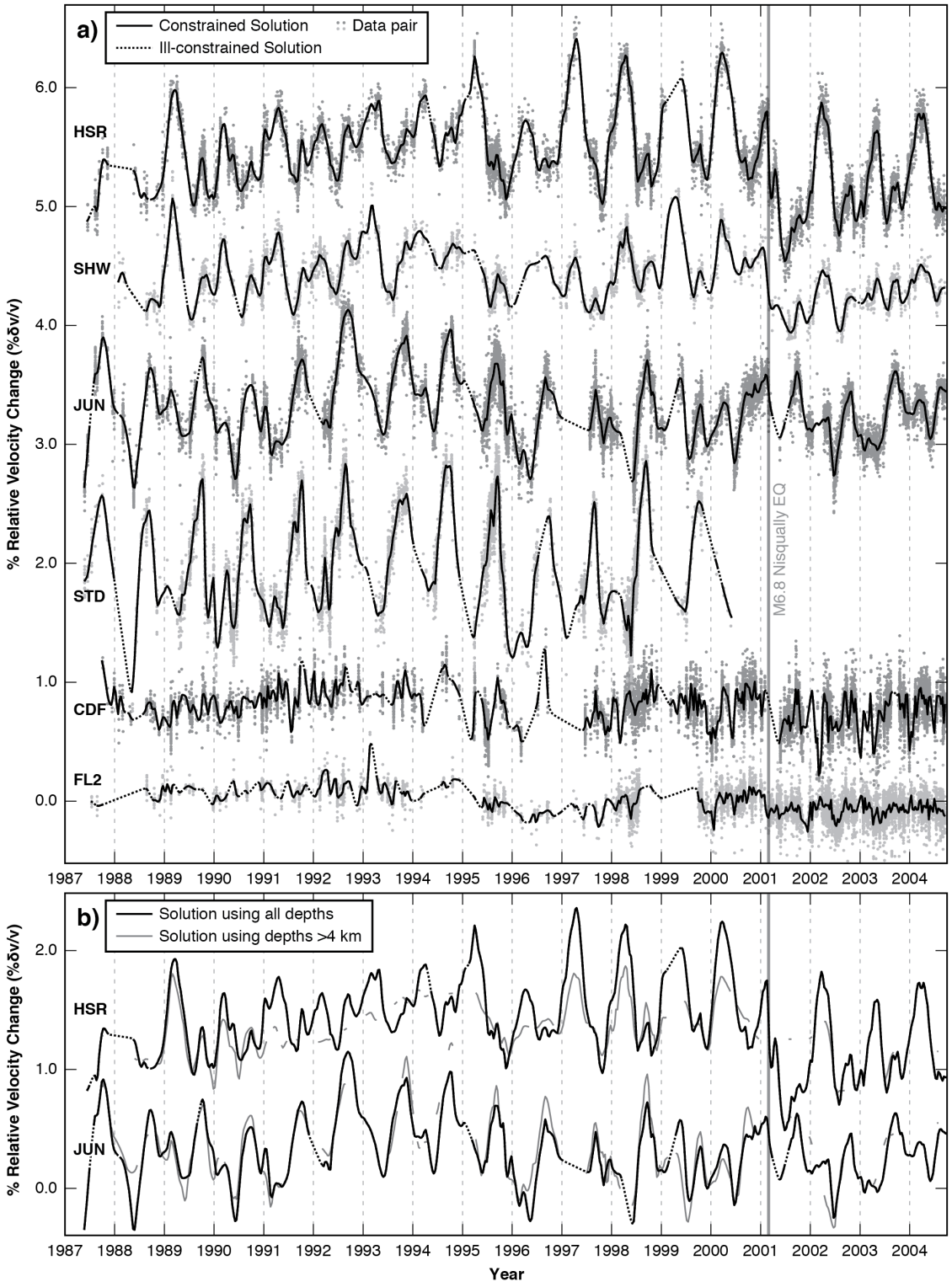

Figure 5: (a) Inversion results for shallow (<4 km; black line, dashed where solution ill-constrained) earthquake pairs only. Gray dots represent the times and relative velocity changes of individual pairs of observations. For a single earthquake pair, one dot is plotted at the time of the first earthquake, the other at

the time of the second, and their vertical separation is the observed velocity change between them. Pairs are plotted around the final solution such that if one dot is above the solution, the other is an equal distance below it. The dots serve to illustrate the temporal density of data, as well as uncertainty in the continuous solution. (b) Comparison of inversion solution using shallow (same as in (a)) and deep (>4 km; gray line, not plotted where ill-constrained) earthquake pairs separately for two representative stations. Solutions for deep and shallow source earthquakes are similar in timing and amplitude, indicating the coda waves from both depth subsets are sampling similar, presumably shallow volumes. Vertical gray line in both plots corresponds to date of M6.8 Nisqually earthquake. Results for stations SEP, YEL, EDM, and SOS are not plotted because there were an insufficient number of pairs to produce a stable inversion.

due to changes within the volcano itself, we have also inverted for velocity change using a subset of earthquakes in the depth range 4 to 10 km, where we expected changes from the magma chamber could be more visible due to a deeper source and sampling volume. Although the seismicity is more clustered in time, there are pairs of repeating earthquakes that span the gaps between swarms. Figure 5b also shows the remarkable similarity between relative velocity changes for the 1 to 4 km and 4 to 10 km depth ranges, and demonstrates that seasonal velocity changes are stronger than any other signal from within the volcano for the entire depth range we consider. The similarity in amplitude of the annual velocity changes for both subsets further suggests our coda waves are primarily composed of surface waves sampling the shallow subsurface, consistent with our 1-10 Hz band pass.

5. Seismicity Rate and Seasonal Repeaters

We observe a greater rate of repeating earthquakes during summer than winter when we include the entire catalog regardless of magnitude. Christiansen et al. [2005] found that M1.5+ earthquakes at MSH are statistically more common between July and October than during the rest of the year. There is still a possibility this is in part an

artifact of an incomplete catalog due to station health during the winter. Christiansen et al. [2005] attribute the increased seismicity to reduced normal stress from snow unloading and/or increased pore pressure of between 8 and 64 kPa from a rise in groundwater level by pore pressure diffusion.

Another observation is that the time between pairs of earthquakes is not randomly distributed, but has annual cyclicity, and further suggests that seismicity and stress changes in the shallow subsurface are seasonal in nature. Figure 6 illustrates that although most pairs of earthquakes have less than 6 months of time between them, there are a significant number of pairs that recur on a nearly yearly basis. Pairs that occur only in summer dominate the seasonal recurrence of repeating earthquakes, but other seasons

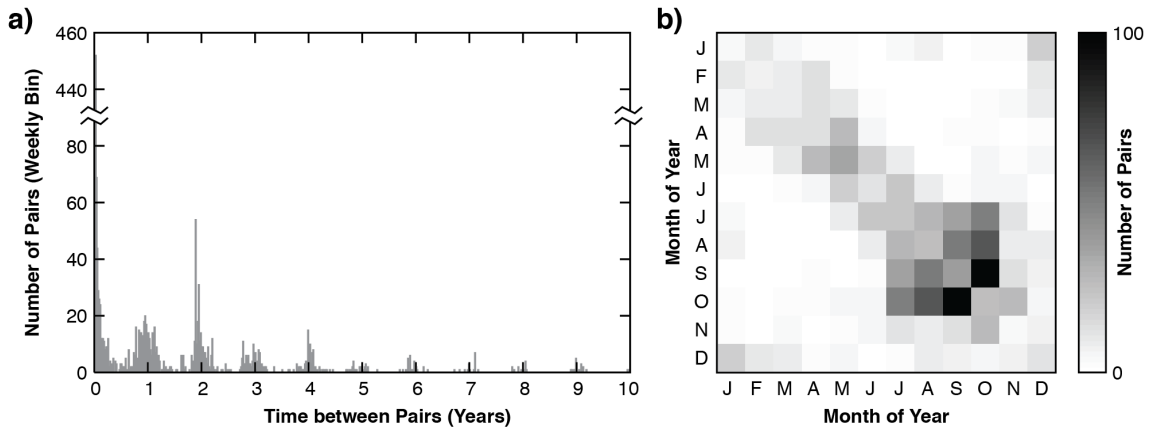

Figure 6: (a) Number of pairs of repeating earthquakes versus time between pairs in 1-week bins. Similar earthquakes repeat on yearly time scales and are not randomly distributed with time. (b) Matrix of number of pairs of earthquakes where one earthquake occurs in the month denoted by row and the second occurs in the month by column. The matrix is symmetric, does not take into account which earthquake occurred first, and only includes pairs of earthquakes with time between earthquakes greater than 6 months. Although we have more pairs that occur each summer, pairs that occur in winter repeat primarily in winter. For both plots, only repeating earthquakes of M0+ and depths <4 km are included to reduce effects of biased sampling of smaller earthquakes during the summer and lack of sustained earthquakes at depth.

show a similar preference. If the shallow, heterogeneous stress field is changing throughout the year from hydrologic changes, then the different families of earthquakes could be responses to those changes. That is, earthquakes that happen in the winter might have different orientations than the earthquakes during the summer, and although they may be located close to one another, they don't have similar waveforms.

6. Interpretation

6.1. Seasonal variation as climatological loading

Comparing the relative velocity change as a function of time within each year reveals that the largest changes in velocity do not occur with the same pattern on every station (Figure 7). Stations on the volcano (HSR and SHW) have the highest relative velocity changes in the spring months (March through May), while stations off the volcano (STD and JUN) have highest changes in the late summer and early autumn (August through October). Although less obvious, the timing of the secondary peak for stations on the volcano aligns with the primary peak for stations off the volcano, and vice versa. To test how well the differences between stations are actually resolved by the inversion, we can compare the reduced chi-square misfit (χ^2_{red}) for the data at each station with various velocity change models, γ(t). For example, a value calculated for the data from HSR and model from JUN of close to 1 would indicate the model fits the data within the measurement uncertainties and accounts for the number of degrees of freedom. Table 1 summarizes the values of for data from the six best stations and models with no velocity change, the best model for that station, HSR's best model, JUN's best model, and a model using data from all stations in the same inversion. Perhaps unsurprisingly,

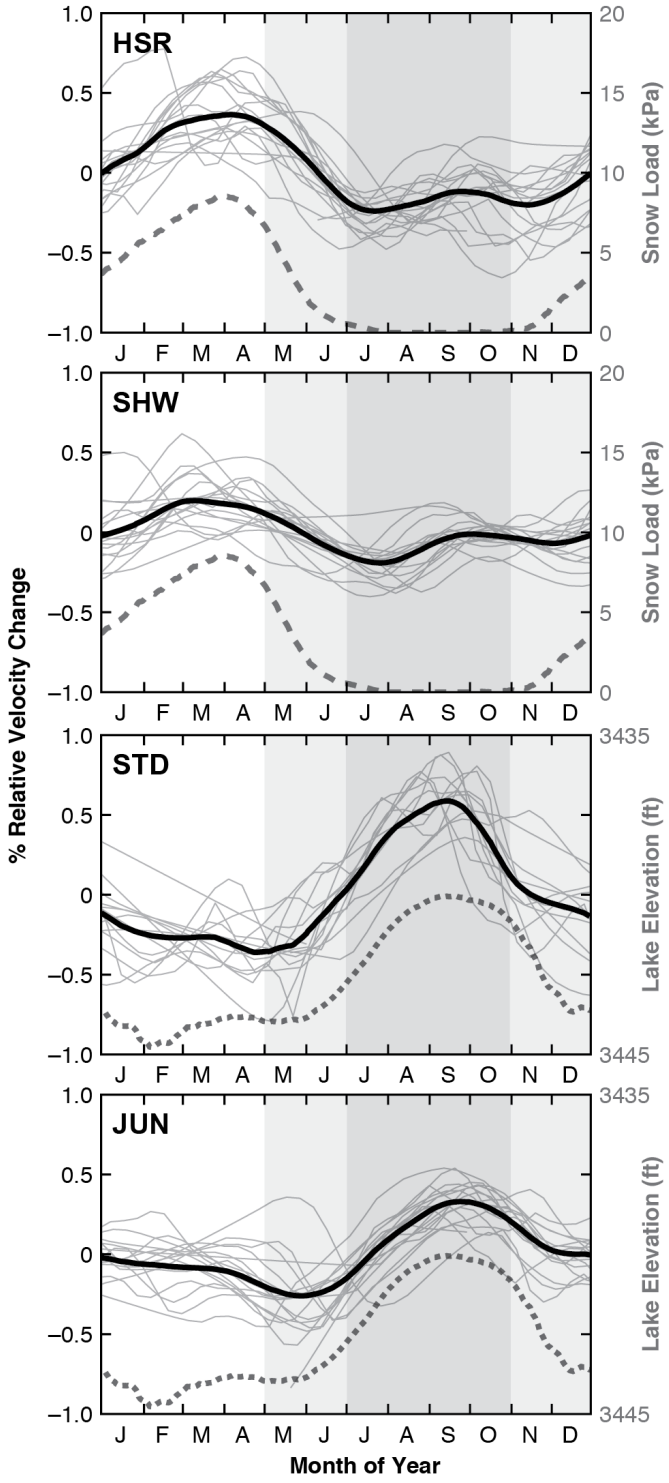

Figure 7: Velocity as a function of month of year, demeaned raw solutions in light gray and average in thicker black. Dashed line corresponds to average yearly snow load at SNOTEL station 748 in Sheep Canyon. Dotted line corresponds to average lake elevation at Spirit Lake, plotted with an inverted y-axis to better illustrate the anti-correlation. Shaded area denotes months of the year with increased shallow seismicity from Christiansen et al. [2005].

	Zero change	Best fit	HSR model	JUN model	Hybrid model
HSR	6.26	2.25	2.25	8.00	4.78
SHW	5.15	1.84	3.73	5.99	3.53
STD	4.09	1.86	6.26	3.19	2.93
JUN	5.64	1.86	8.11	1.86	2.73
CDF	2.16	1.51	6.81	3.84	2.08
FL2	1.90	1.51	11.07	5.65	2.39

Table 1. Comparison of χ^2_{red} misfit of data to different models.

using the model of JUN with the data from HSR (and vice versa) results in a significant increase in the misfit, even more than the assumption of zero change. We conclude that the models of velocity change are unique and resolvable from each other.

Given that the difference in amplitudes between stations is resolvable, the differences most likely represent different processes to which stations have varying sensitivity with a ~6 month offset and recurrence interval of one year. The high relative velocity in March corresponds to the peak annual snowpack, which we have verified using four SNOTEL stations in the Mount St. Helens vicinity (Fig. 2), and would act to increase the velocity by closing cracks due to increased surface loading. The general shape of the snowpack curve (Figure 7) corresponds to the velocities at stations nearest the volcano (HSR and SHW) with nearly zero lag. Also, HSR and SHW would receive more snow than JUN and STD due to their elevation, and the relatively slower velocities in spring 1996 occurred during a year with lower snowpack further suggest a causal relationship (Figure 8a).

The later peak in relative velocity in September corresponds to times when earthquakes occur more frequently. It seems to us an unlikely coincidence that increased velocity and earthquakes occur during the same time of year. One possibility is that an

increase in the height of the groundwater table increases pore pressures and reduces local effective normal forces, resulting in more frequent earthquakes. In addition, an increase in the height of the groundwater table could increase velocities by closing cracks due to the weight of the water, similar to snow pack, or through poroelastic effects. Although no direct measures of the groundwater table are available in the area, lake elevation data from Spirit Lake may be used as a proxy and constraint on groundwater models. Simple hydrologic modeling by Christiansen et al. [2005] indicates the groundwater level change is on the order of 1 to 9 m. The timing of the maximum highs in modeled groundwater levels qualitatively coincides with the onset of increased seismicity rate and relative velocity increases. A complication of this interpretation is that the depth of the water table is unknown, but could potentially be several km deep [Hurwitz et al., 2003] or only a few tens of meters deep if there is a perched aquifer [Bedrosian et al., 2008].

Lake level data serve as a proxy for groundwater changes. When lake elevation is compared to velocity (Figures 7 and 8b) we find the two are anti-correlated. The September peak in velocity increases at STD and JUN corresponds to lower lake elevations, suggesting shallow water loading is likely not affecting the velocity. We propose instead that at the lower elevations of STD and JUN velocities reflect fluid saturation in the shallow subsurface, such that decreased water saturation (indicated by low lake level) increases the velocity and vice versa [e.g., Grêt et al., 2006]. At higher elevations, velocity changes are smaller during this time of year, so fluid saturation may not change much seasonally. We note lake level was abnormally high in early 1996 and 1997 compared with other years, but this does not correspond to extraordinary decreases in the velocity change record. We presume during most years complete saturation was

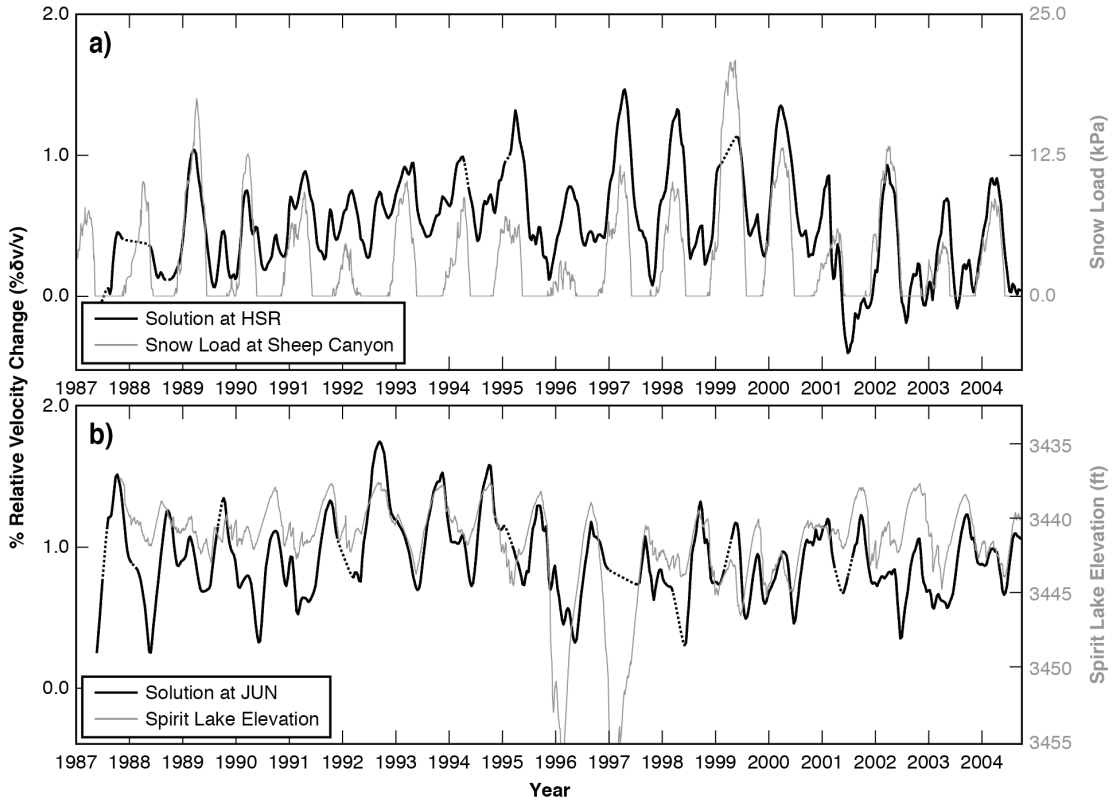

Figure 8: (a) Comparison of full velocity record at HSR with snow load. Note that lower velocities in 1996 correspond to a winter with lower snow loading. (b) Comparison of full velocity record at JUN with elevation of Spirit Lake, which we use as a proxy for shallow fluid saturation. Lake elevation is plotted with an inverted y-axis to emphasize anti-correlation of saturation with velocity.

achieved, and during those two years lake level increased beyond the level corresponding to full saturation and had no extra effect. Changes in saturation are likely very shallow (on the order of perhaps a few meters) and should not affect seismicity at depth. Therefore, the simplest explanation of correlation between seismicity and velocity is that seismicity is more related to snow unloading, and anti-correlated with the higher velocities in winter.

Let us also briefly consider other possible candidates for seasonal changes in velocity. Thermoelastic strain (i.e., deformation related to spatiotemporal variations of

temperature) could also produce seasonal velocity changes through seasonal changes in temperature [Ben-Zion and Leary, 1986; Meier et al., 2010], but does not readily explain the generation of seasonal earthquakes or the discrepancy in sensitivity between stations. Daily to weekly variations in barometric pressure of a few kPa have been shown to alter velocities in wells [e.g., Silver et al., 2007], and barometric pressure also varies seasonally. Barometric pressure is not measured at SNOTEL stations near Mount St. Helens, and the nearest comparable station (approx. 100 km north) at Burnt Mountain (SNOTEL site 942) measured seasonal variations of <1 kPa with higher pressures during the summer. The amplitude of the barometric pressure variations is significantly less than that due to snow loading, and is likely insufficient to explain the velocities at STD and JUN. Weekly variations in barometric pressure there are on the order of 3–4 kPa, which could contribute to some of the misfit in our inversions, as we do not allow velocities to change on time scales shorter than two weeks.

One way to discriminate between possible sources is if we filter the coda in separate frequency bands (1-5 and 5-10 Hz; Figure 9). The higher frequency velocity changes are greater than the lower frequency changes in September and the reverse is observed in March. If we assume the 1-5 Hz energy is sampling deeper than 5-10 Hz due to the frequency-dependent depth sampling of surface waves in the coda, this result suggests that the peak velocities in September are located shallower than in March, which is most consistent with shallow fluid saturation variations.

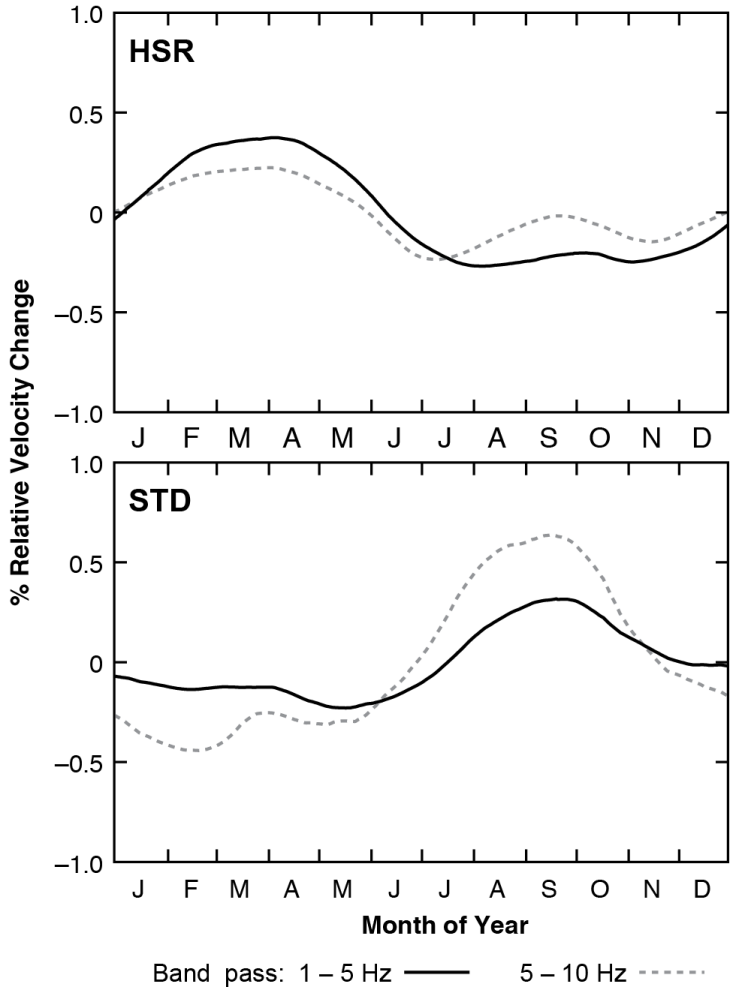

Figure 9: Velocity as a function of month of year in two different frequency bands (1-5 Hz and 5-10 Hz) at stations HSR and STD. The difference between the 1-5 and 5-10 Hz bands suggests the velocity changes in spring are deeper than the changes in autumn, due to the frequency-dependent depth sampling of surface waves in the coda.

6.2. Response to Nisqually Earthquake

Decreases in seismic velocity are commonly observed following earthquakes, particularly on soft soils, and have been interpreted by other authors as non-linear response to shaking, which heals on the timescale of seconds to years [Dodge and Beroza, 1997; Li et al., 2007; Rubenstein et al., 2007; Brenguier et al., 2008b; Sawazaki et al., 2009; Wegler et al., 2009; Yamada et al., 2010; Tatagi et al., 2012]. One clear non-annual

signal is a sharp decrease in velocity in early 2001 of 0.2% at CDF and FL2, 0.5% at SHW, and 0.7% at HSR (it is unresolved at STD due to a low number of pairs crossing the date of the earthquake, and difficult to objectively quantify at JUN). The timing of this decrease corresponds exactly with the February 28, 2001, M6.8 Nisqually earthquake, which occurred 113 km to the NNW of MSH at 52 km depth.

The Nisqually earthquake is unique in that it is the only large or local earthquake that coincides with an observable change in velocity in our data. There are no obvious changes during the times of the M5.8 Satsop earthquake in 1999, the M5.4 Duvall earthquake in 1996, a nearby M4.9 in 1989, or the more distant M7.9 Denali earthquake in Alaska in 2002. The Nisqually earthquake imparted peak ground acceleration (PGA) on the order of 6 to 7% g to the entire network at MSH, based on the PNSN ShakeMap. This was likely the strongest shaking during the 18-year study period; all other earthquakes cited above had estimated PGA less than 2% g at MSH. However, this acceleration is low compared to the level of shaking considered in the literature, where the largest changes also occur near the rupture. Additionally, the velocity does not recover in at least the next three years as one might expect for a non-linear soil-related response, and there is no appreciable difference between the amplitude in different frequency bands, further suggesting the velocity change is not concentrated at the surface. Given the distance from the earthquake and that the observed changes are concentrated nearest the volcano's summit, the most likely explanation is a dynamic yet permanent response to shaking. Battaglia et al. [2012] studied the response of Yasur volcano to a nearby M7.3 earthquake and also found the maximum change occurred near the summit. PGA and velocity changes at Yasur are comparable, though slightly higher, than MSH

for Nisqually (0.5 – 3.5% velocity change and ~15% g). Battaglia et al. [2012] proposed opening of cracks near the volcanic conduit due to permeability enhancement [Rojstaczer et al., 1995] or exsolution of magmatic gasses as possible explanations for decreased velocity at Yasur, which may also be appropriate to apply at MSH.

6.3. Long-term trends

By increasing the weight of the regularization in the inversion, we can damp out the annual signal to more clearly compare long-term trends without introducing unnecessary artifacts from filtering the best fit. One by-product is smoothing of steps in velocity, such as due to the Nisqually earthquake or any smaller steps that might be present but obscured by the large annual signal. Figure 10 shows the result of damping the inversion just enough to eliminate the seasonal signal. The velocities increase and decrease in roughly the same way for most of the stations, though with different amplitudes. This similarity leads us to believe the signal is real and not a station-specific artifact. Also, it is small or nonexistent on stations far away from the volcano (CDF, FL2) and slightly smaller for stations near the summit (SHW, HSR) than further from the summit (STD, JUN).

We do not see a relationship between the times of deep swarms and the sense of velocity change. Velocities generally increase during the 1989-1992 and 1998 swarms and perhaps decrease around 1995, but such changes are not unique to just these time periods. There is no convincing evidence of magma injection that would presumably change velocities during the other periods, indicating the majority of the long-term signal is persistent and likely not directly related to magmatic injection. Although we find no

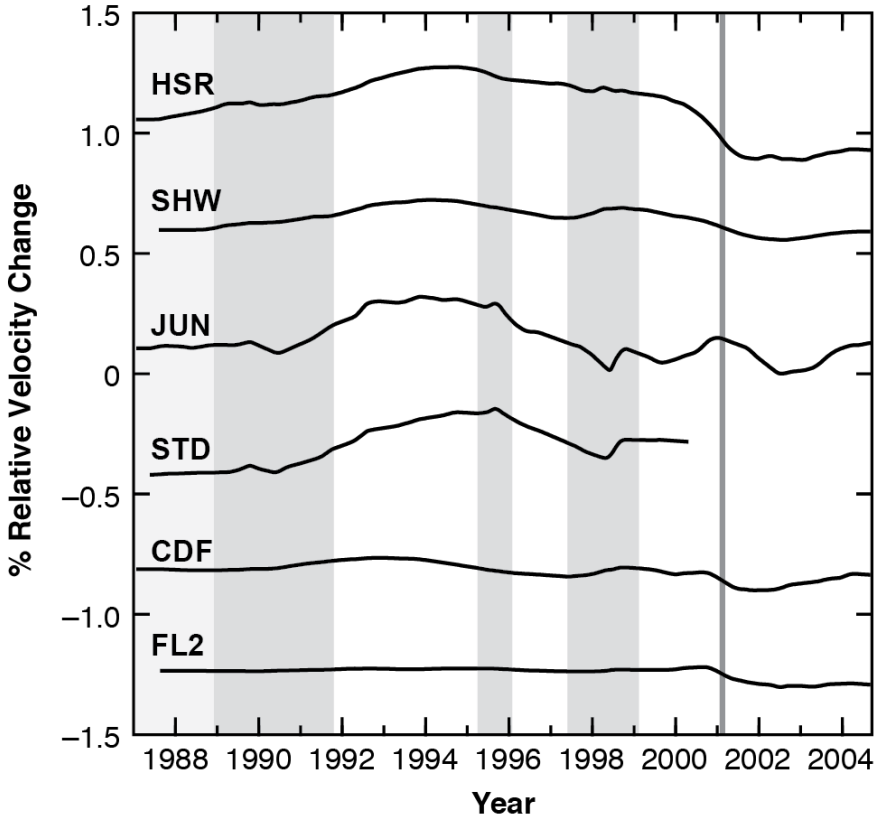

Figure 10: Inversion solution with greater weight of smoothing regularization, mostly damping the annual signal with the exception of 1989 and 1998 on stations JUN and STD due to the large amount of pairs. Vertical line corresponds to time of Nisqually earthquake; the step-like decrease in velocity has also been smoothed as a result of the increased regularization. Times of increased deep seismicity and deformation are highlighted in gray, at the same times as in Figure 1.

conclusive evidence for a change in velocity during the times of proposed intrusions, it is still possible some changes are volcanic in origin or potentially related to accumulation of exsolved gases from depth. We also note that, as mentioned before, 1996 was a dry year and may be partially to blame for the relative decrease in velocity. If that is the case, an alternative explanation for the long-term trend is that it is related to variability in the water table over the course of several years. Again, without well data we cannot independently verify whether this is the case. Other possibilities for increasing velocity are the growth of Crater Glacier or settling of the dome, but the large signal at more

distant stations suggests a distributed source.

7. Discussion

For the 1987-2004 time period at MSH the subsurface velocity structure appears to respond to small stress changes, such as those due to the loads imparted by seasonal precipitation and shaking from a distant large earthquake. However, we do not see any correlations between velocity changes and the time when injections of magma have been proposed to occur beneath MSH. A possible explanation for why we don't see any evidence of magma injection is that velocity changes caused by intrusions were small and/or localized where we have little sensitivity with this method, which is limited to the providing information only about the volume sampled by coda waves. As we have seen from the similarity of velocity changes for shallow and deep earthquakes, coda waves may not sample the deeper part of the magmatic system, where magma likely was accumulating in 1987-2004, as much as the shallower subsurface. Successful detection of deeper changes in velocity associated with small injections of new magma may depend on favorable occurrence of well-distributed deeper earthquakes and dense scattering. However, we expect that a velocity change due to an intrusion would not be limited to the chamber alone, and would be distributed around the chamber and to the surface as the host rock deforms due to the increased pressure in the system.

Let us consider the amplitude of a velocity change at the surface due to increased pressure in the magma chamber. We know from Moran [1994] that focal mechanisms of deep earthquakes corresponded to pressure changes within an approximately cylindrical magma chamber, which increased from below lithostatic pressure during 1980 to above

lithostatic pressure in 1987-1992. Although there is a large tradeoff between parameters, especially chamber radius and pressure, misfits decreased significantly for pressures more than 5 MPa above lithostatic pressure. We solve for near-surface deformation and strain for this pressure increase within the magma chamber by approximating it as an oblate spheroid following Bonaccorso and Davis [1999] and Lisowski [2006]:

$$u_r = \frac{\alpha^2 \Delta P}{4\mu r}\left(\frac{c_1^3}{R_1^2} + \frac{2c_1(-3+5\nu)}{R_1} + \frac{5c_2^3(1-2\nu) - 2c_2 r^2(-3+5\nu)}{R_2^3}\right) \tag{3}$$

$$u_t = 0 \tag{4}$$

$$u_z = -\frac{\alpha^2 \Delta P}{4\mu}\left(\frac{c_1^2}{R_1^2} + \frac{2(-2+5\nu)}{R_1} + \frac{c_2^3(3-10\nu) - 2r^2(-2+5\nu)}{R_2^3}\right) \tag{5}$$

$$\varepsilon_{rr} = \frac{\partial u_r}{\partial r} \tag{6}$$

$$\varepsilon_{tt} = \frac{u_r}{r} \tag{7}$$

$$\varepsilon_{zz} = -\frac{\nu}{1-\nu}\left(\varepsilon_{rr} + \varepsilon_{tt}\right) \tag{8}$$

where u is displacement in the radial, tangential, and up directions; ε is strain; ΔP is change in pressure; α is the radius of the chamber; c_1 is the depth of the top of the chamber; c_2 is the depth to the bottom of the chamber; r is horizontal distance from the center of the chamber; $R_1 = \sqrt{r^2 + c_1^2}$ and $R_2 = \sqrt{r^2 + c_2^2}$ are the distances from a point on the surface to the top and bottom of the chamber, respectively; ν is Poisson's ratio; μ is the elastic modulus. For Mount St. Helens we assume values listed in Table 2.

ΔP	v	μ	c_1	c_2	α
5 MPa	0.25	1.0e10 Pa	6500 m	11500 m	500 m

Table 2. Parameters for estimating surface strain due to a pressure increase at depth.

Strain can then be related to change in shear velocity by using a simplified form of equation (11) of Hughes and Kelly [1953]:

$$\frac{\mathrm{dv}_{12}}{\mathrm{v}_{12}} = \frac{2m\theta + n\varepsilon_{33}}{4\mu} \tag{9}$$

where m and n are two of the three Murnaghan third-order elastic constants, μ is the shear modulus, θ is dilatation or volumetric strain, and ε_{33} is strain perpendicular to the direction of travel and polarization of the wave (e.g., ε_{zz} for SV velocity). The Murnaghan constants, m, n, and l, account for nonlinear elastic deformation, including opening and closing of cracks. We can estimate the Murnaghan constants using equations proposed in Tsai [2011], which relate strain from hydrologic loading to change in velocity. We can combine equations 10 and 17 of Tsai [2011] to estimate the magnitude of m/μ at the surface as:

$$\frac{m}{\mu} \sim \frac{\mathrm{dv}}{\mathrm{v}}\left(\frac{E}{(1+\nu)(1-2\nu)\phi p}\right) \tag{10}$$

where μ is the shear modulus, v is Poisson's ratio, E is Young's modulus, ϕ is porosity, p is pressure from the height of a column of water (or snow water equivalent), and dv/v is

change in velocity. Using the values in Table 3 under the assumption that the spring velocity changes are a response to direct loading due to the weight of snow pack and the possibility that autumn changes are due to groundwater level, the ratio m/μ is close to –1x10^4, at the high end of observed values in laboratory experiments for highly cracked samples [Tsai, 2011]. Without further constraint on the value of n, we assume it is close to m. Therefore, the maximum value of change in SV velocity for our theoretical magmatic intrusion is approximately –0.05% (Figure 11). Although strain and velocity increase with depth, this change is still near or below the level of noise with our method, so it is possible a 5 MPa pressure increase could have escaped detection even without consideration of finite compressibility of a zone around the chamber [Mastin et al., 2008; Dzurisin et al., 2008]. Ueno et al. [2012] observed decreases in velocity of 0.2-0.8% during several intrusion-related swarms with estimated volumes on the order of a few thousand m^3, however, these intrusions were also accompanied by measurable surface deformation and volumetric strain of more than 10^{-6}. Our predicted strain is roughly an order of magnitude less than this, consistent with our lack of observable velocity change. The choice of pressure increase is somewhat arbitrary, but allows us to estimate an upper bound on the change in pressure in the chamber given our lack of detection to as much as 10 MPa for a chamber of 500 m radius.

	v	E	ϕ	p	dv/v	m/μ
Snow load	0.25	1.0e10 Pa	1 *	10 to 20 kPa	+0.7%	–6e3 to –1e4
Water table			0.2	10 to 90 kPa	+1.0%	–9e3 to –8e4

*Table 3. Parameters for estimating Murnaghan constant m. *Assumes water exists only as snow above the surface.*

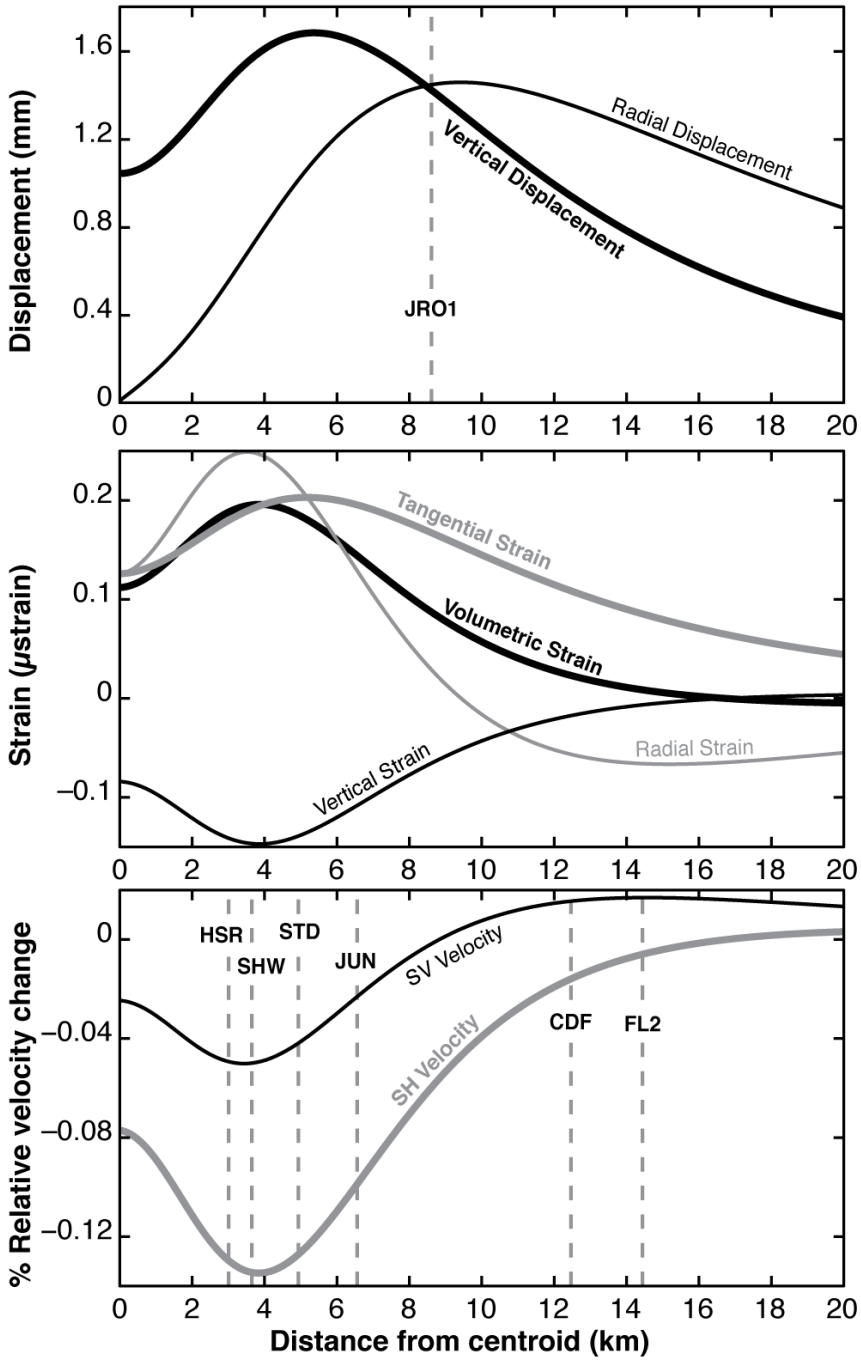

Figure 11: Estimations of displacement (top), strain (middle), and velocity change (bottom) at the surface assuming a 5 MPa increase in pressure within the MSH magma chamber. Distances to GPS and seismic stations are noted by vertical lines and labeled. The displacements are at or below the level of detection for GPS motion, consistent with the lack of observed motion. Although SH velocity is above the noise level for velocity change, coda waves are likely much more sensitive to SV velocity, which is below the noise level.

8. Conclusions

We used CWI to create a continuous record of seismic velocity change using triggered earthquake data spanning nearly two decades to investigate the history of magma injection and pressurization of the MSH magmatic system. This method is complementary to other studies of velocity change using continuous data, such as ambient noise interferometry, but can be applied to older datasets where continuous data are unavailable and only a triggered record exists. Temporal resolution of velocity change is dependent on the rate of repeating seismicity, and could also be applied to more frequent swarms of earthquakes, like those during volcanic eruptions, to produce a record of velocity change on a significantly shorter time scale than presented here.

In this study, we did not resolve a velocity change due to magmatic intrusion(s), though the lack of velocity change directly attributable to the volcano between the 1980-1986 and 2004-2008 eruptions is consistent with a lack of precursory deformation. We concede it is possible that intrusions occurred, but did not pressurize the chamber enough to alter the shallow velocity structure to which this technique is most sensitive. We estimate the maximum pressure change that could have escaped our detection to be on the order of 10 MPa, which is within the previously estimated bounds of pressure changes determined by deep earthquake focal mechanisms. We found well-resolved seismic velocity changes that are dominated by seasonal variability, likely caused by climatic forcing such as snow loading and shallow water table fluctuations. In addition, the increased rate of seismicity is anti-correlated with the higher velocities in late winter, and we believe this is most likely due to snow unloading. The most significant non-seasonal signal is a decrease in velocity at the time of the Nisqually earthquake, during which

shaking dynamically likely caused a permanent alteration of the velocity structure. We suggest the shallow seismicity and observed velocity changes are indications that the volcano was pressurized and sensitive to relatively small pressure changes of a few kPa well before the 2004 eruption.

Acknowledgements

Waveform data and earthquake catalog used in this paper are courtesy of the Pacific Northwest Seismic Network, and are freely available upon request. The authors would like to thank Seth Moran, Weston Thelen, Stephanie Prejean, Steve Malone, and Matt Haney for discussions during preparation of the text, and Weston Thelen and Florent Brenguier for their reviews.

References

Battaglia, J., J. -P. Métaxian, and E. Garaebiti (2012), Earthquake-volcano interaction imaged by coda-wave interferometry, *Geophys. Res. Lett., 39,* L11309, doi:10.1029/2012GL052003.

Bedrosian, P. A., M. Burgess, and A. Hotovec (2008), Groundwater hydrology within the crater of Mount St. Helens from geophysical constraints, *Eos Trans. AGU, 89*(53), Fall Meet. Suppl., Abstract V43E-2191.

Ben-Zion, Y., and P. Leary (1986), Thermoelastic strain in a half-space covered by unconsolidated material, *Bull. Seismol. Soc. Am., 76,* 1447–1460.

Bonaccorso, A., and P. M. Davis (1999), Models of ground deformation from vertical volcanic conduits with application to eruptions of Mount St. Helens and Mount Etna, *J. Geophys. Res., 104,* B5, 10531–10542.

Brenguier, F., N. M. Shapiro, M. Campillo, V. Ferrazzini, Z. Duputel, O. Coutant, and A. Nercessian (2008a), Towards forecasting volcanic eruptions using seismic noise, *Nature Geosci., 1,* 126–130, doi:10.1038/ngeo104.

Brenguier, F., M. Campillo, C. Hadziioannou, N. M. Shapiro, R. M. Nadeau, and E. Larose (2008b), Postseismic Relaxation Along the San Andreas Fault at Parkfield from Continuous Seismological Observations, *Science, 321,* 1478–1481, doi:10.1126/science.1160943.

Carmona, E., J. Almendros, J. A. Peña, and J. M. Ibáñez (2010), Characterization of fracture systems using precise array locations of earthquake multiplets: An example at Deception Island volcano, Antarctica, *J. Geophys. Res.,* 115, B06309, doi:10.1029/2009JB006865.

Christiansen, L. B., S. Hurwitz, M. O. Saar, S. E. Ingebritsen, and P. A. Hsieh (2005), Seasonal seismicity at western United States volcanic centers, *Earth Planet. Sci. Lett.,* 240, 307–321.

Dodge, D. A., and G. C. Beroza (1997), Source array analysis of coda waves near the 1989 Loma Prieta, California, mainshock: Implications for the mechanism of coseismic velocity changes, *J. Geophys. Res.,* 102, B11, 24,437–24,458.

Dzurisin, D., M. Lisowski, M. P. Poland, D. R. Sherrod, and R. G. LaHusen (2008), Constraints and Conundrums Resulting from Ground-Deformation Measurements

Made During the 2004-2005 Dome-Building Eruption of Mount St. Helens, Washington, in *A Volcano Rekindled: The Renewed Eruption of Mount St. Helens, 2004–2006,* edited by D. R. Sherrod, W. E. Scott, and P. H. Stauffer, *Prof. Paper 1750,* chap. 14, pp. 281–300, U.S. Geol. Surv., Reston, Va.

Gerlach, T. M., K. A. McGee, and M. P. Doukas (2008), Emission Rates of CO_2, SO_2, and H_2S, Scrubbing, and Preeruption Excess Volatiles at Mount St. Helens, 2004–2005, in *A Volcano Rekindled: The Renewed Eruption of Mount St. Helens, 2004–2006,* edited by D. R. Sherrod, W. E. Scott, and P. H. Stauffer, *Prof. Paper 1750,* chap. 26, pp. 543–571, U.S. Geol. Surv., Reston, Va.

Grêt, A., R. Snieder, and J. Scales (2006), Time-lapse monitoring of rock properties with coda wave interferometry, *J. Geophys. Res.,* 111, B03305, doi:10.1029/2004JB003354.

Hughes, D. S., and J. L. Kelly (1953), Second-Order Elastic Deformation of Solids, *Phys. Rev.,* 92, 1145–1149.

Hurwitz, S., K. L. Kipp, S. E. Ingebritsen, and M. E. Reid (2003), Groundwater flow, heat transport, and water table position within volcanic edifices: Implications for volcanic processes in the Cascade Range, *J. Geophys. Res.,* 108, B12, 2557, doi:10.1029/2003JB002565.

Kanu, C. O., R. Snieder, and D. O'Connell (2013), Estimation of velocity change using repeating earthquakes with different locations and focal mechanisms, *J. Geophys. Res.,* 118, 1–10, doi:10.1002/jgrb.50206.

Lehto, H. L., D. C. Roman, and S. C. Moran (2013), Source mechanisms of persistent shallow earthquakes during eruptive and non-eruptive periods between 1981 and 2011 at Mount St. Helens, Washington, *J. Volcan. Geotherm. Res.,* 256, 1–15, doi:10.1016/j.volgeores.2013.02.005.

Li, Y.-G., P. Chen, E. S. Cochran, and J. E. Vidale (2007), Seismic velocity variations on the San Andreas fault caused by the 2004 *M*6 Parkfield Earthquake and their implications, *Earth Planets Space,* 59, 21–31.

Lisowski, M., D. Dzurisin, R. P. Denlinger, and E. Y. Iwatsubo (2008), Analysis of GPS-Measured Deformation Associated with the 2004–2006 Dome-Building Eruption of Mount St. Helens, Washington, in *A Volcano Rekindled: The Renewed Eruption of Mount St. Helens, 2004–2006,* edited by D. R. Sherrod, W. E. Scott, and P. H. Stauffer, *Prof. Paper 1750,* chap. 15, pp. 301–333, U.S. Geol. Surv., Reston, Va.

Lisowski, M. (2006) Analytical volcano deformation source models, in *Volcano Deformation: Geodetic Monitoring Techniques,* by D. Dzurisin, chap. 8, pp. 279–304, Springer-Praxis, Chichester, UK.

Massin, F., J. Farrell, and R. B. Smith (2013), Repeating earthquakes in the Yellowstone volcanic field: Implications for rupture dynamics, ground deformation, and migration in earthquake swarms, *J. Volcan. Geotherm. Res.,* 257, 159–173, doi:10.1016/j.jvolgeores.2013.03.22.

Mastin, L. G., E. Roeloffs, N. M. Beeler, and J. E. Quick (2008), Constraints on the Size, Overpressure, and Volatile Content of the Mount St. Helens Magma System from Geodetic and Dome-Growth Measurements During the 2004–2006+ Eruption, in *A*

Volcano Rekindled: The Renewed Eruption of Mount St. Helens, 2004–2006, edited by D. R. Sherrod, W. E. Scott, and P. H. Stauffer, *Prof. Paper 1750,* chap. 22, pp. 461–488, U.S. Geol. Surv., Reston, Va.

Mastin, L. G. (1994), Explosive tephra emissions at Mount St. Helens, 1989–1991: The violent escape of magmatic gas following storms?, *Geol. Soc. Am. Bull.,* 106(2), 175–185.

Meier, U., N. M. Shapiro, and F. Brenguier (2010), Detecting seasonal variations in seismic velocities within Los Angeles basin from correlations of ambient seismic noise, *Geophys. J. Int.,* 181, 985–996.

Moran, S. C. (1994), Seismicity at Mount St. Helens, 1987–1992: Evidence for repressurization of an active magmatic system, *J. Geophys. Res.,* 99, B3, 4341–4354.

Moran, S. C., S. D. Malone, A. I. Qamar, W. A. Thelen, A. K. Wright, and J. Caplan-Auerbach (2008), Seismicity Associated with Renewed Dome Building at Mount St. Helens, 2004–2005, in *A Volcano Rekindled: The Renewed Eruption of Mount St. Helens, 2004–2006,* edited by D. R. Sherrod, W. E. Scott, and P. H. Stauffer, *Prof. Paper 1750,* chap. 2, pp. 27–60, U.S. Geol. Surv., Reston, Va.

Musumeci, C., S. Gresta, and S. D. Malone (2002), Magma system recharge of Mount St. Helens from precise relative hypocenter location of microearthquakes, *J. Geophys. Res.,* 107, B10, 2264, doi:10.1029/2001JB000629.

Nakamura, A., A. Hasegawa, N. Hirata, T. Iwasaki, and H. Hamaguchi (2002), Temporal Variations of Seismic Wave Velocity Associated with 1998 M6.1 Shizukuishi Earthquake, *Pure Appl. Geophys.,* 159, 1183–1204.

Pacheco, C., and R. Snieder (2005) Time-lapse travel time change of multiply scattered acoustic waves, *J. Acoust. Soc. Am.,* 118(3), 1300–1310.

Pallister, J. S., C. R. Thornber, K. V. Cashman, M. A. Clynne, H. A. Lowers, C. W. Mandeville, I. K. Brownfield, and G. P. Meeker (2008), Petrology of the 2004–2006 Mount St. Helens Lava Dome—Implications for Magmatic Plumbing and Eruption Triggering, in *A Volcano Rekindled: The Renewed Eruption of Mount St. Helens, 2004–2006,* edited by D. R. Sherrod, W. E. Scott, and P. H. Stauffer, *Prof. Paper 1750,* chap. 30, pp. 648–702, U.S. Geol. Surv., Reston, Va.

Pandolfi, D., C. J. Bean, and G. Saccorotti (2006), Coda wave interferometric detection of seismic velocity changes associated with the 1999 M = 3.6 event at Mt. Vesuvius, *Geophys. Res. Lett.,* 33, L06306, doi:10.1029/2005GL025355.

Petersen, T. (2007) Swarms of repeating long-period earthquakes at Shishaldin Volcano, Alaska, 2001–2004, *J. Volcan. Geotherm. Res.,* 166, 177–192, doi:10.1016/j.jvolgeores.2007.07.014.

Poland, M. P., and Z. Lu (2008), Radar Interferometry Observations of Surface Displacements During Pre- and Coeruptive Periods at Mount St. Helens, Washington, 1992–2005, in *A Volcano Rekindled: The Renewed Eruption of Mount St. Helens, 2004–2006,* edited by D. R. Sherrod, W. E. Scott, and P. H. Stauffer, *Prof. Paper 1750,* chap. 18, pp. 361–382, U.S. Geol. Surv., Reston, Va.

Poupinet, G., W. L. Ellsworth, and J. Frechet (1984), Monitoring Velocity Variations in the Crust Using Earthquake Doublets: An Application to the Calaveras Fault, California, *J. Geophys. Res.,* 89, B7, 5719–5731.

Ratdomopurbo, A., and G. Poupinet (1995), Monitoring a temporal change of seismic velocity in a volcano: application to the 1992 eruption of Mt. Merapi (Indonesia), *Geophys. Res. Lett.,* 22(7), 775–778.

Rojstaczer, S., S. Wolf, and R. Michel (1995), Permeability enhancement in the shallow crust as a cause of earthquake-induced hydrological changes, *Nature,* 373, 237–239.

Rubenstein, J. L., N. Uchida, and G. C. Beroza (2007), Seismic velocity reductions caused by the 2003 Tokachi-Oki earthquake, *J. Geophys. Res.,* 112, B05315, doi:10.1029/2006JB004440.

Saccorotti, G., I. Lokmer, C. J. Bean, G. Di Grazia, and D. Patanè (2007), Analysis of sustained long-period activity at Etna Volcano, Italy, *J. Volcan. Geotherm. Res.,* 160, 340–354, doi:10.1016/.jvolgeores.2006.10.008.

Sawazaki, K., H. Sato, H. Nakahara, and T. Nishimura (2009), Time-Lapse Changes of Seismic Velocity in the Shallow Ground Caused by Strong Ground Motion Shock of the 2000 Western-Tottori Earthquake, Japan, as Revealed from Coda Deconvolution Analysis, *Bull. Seism. Soc. Am.,* 99(1), 352–366, doi:10.1785/0120080058.

Scott, W. E., D. R. Sherrod, and C. A. Gardner (2008), Overview of the 2004 to 2006, and Continuing, Eruption of Mount St. Helens, Washington, in *A Volcano Rekindled: The Renewed Eruption of Mount St. Helens, 2004–2006,* edited by D. R. Sherrod, W. E. Scott, and P. H. Stauffer, *Prof. Paper 1750,* chap. 1, pp. 3–22, U.S. Geol. Surv., Reston, Va.

Sens-Schönfelder, C., and U. Wegler (2006), Passive image interferometry and seasonal variations of seismic velocities at Merapi Volcano, Indonesia, *Geophys. Res. Lett.,* 33, L21302, doi:10.1029/2006GL027797.

Silver, P. G., T. M. Daley, F. Niu, and E. L. Majer (2007), Active Source Monitoring of Cross-Well Seismic Travel Time for Stress-Induced Changes, *Bull. Seism. Soc. Am., 97*(1B), 281–293, doi:10.1785/0120060120.

Snieder, R. (2002), Coda wave interferometry and the equilibration of energy in elastic media, *Phys. Rev. E,* 66, 046615, doi:10.1103/PhysRevE.66.046615.

Snieder, R. (2006), The Theory of Coda Wave Interferometry, *Pure Appl. Geophys.,* 163, 455–473, doi:10.1007/s00024-005-0026-6.

Snieder, R., A. Grêt, H. Douma, and J. Scales (2002), Coda Wave Interferometry for Estimating Nonlinear Behavior in Seismic Velocity, *Science,* 295, 2253–2255.

Tatagi, R., T. Okada, H. Nakahara, N. Umino, and A. Hasegawa (2012), Coseismic velocity change in and around the focal region of the 2008 Iwate-Miyagi Nairiku earthquake, *J. Geophys. Res.,* 117, B06315, doi:10.1029/2012JB009252.

Thelen, W. A., R. S. Crosson, and K. C. Creager (2008), Absolute and Relative Locations of Earthquakes at Mount St. Helens, Washington, Using Continuous Data: Implications for Magmatic Processes, in *A Volcano Rekindled: The Renewed Eruption of Mount St. Helens, 2004–2006,* edited by D. R. Sherrod, W. E. Scott, and P. H. Stauffer, *Prof. Paper 1750,* chap. 4, pp. 71–95, U.S. Geol. Surv., Reston, Va.

Thelen, W., S. Malone, and M. West (2011), Multiplets: Their behavior and utility at dacitic and andesitic volcanic centers, *J. Geophys. Res.,* 116, B08210, doi:10.1029/2010JB007924.

Tsai, V. C. (2011), A model for seasonal changes in GPS positions and seismic wave speeds due to thermoelastic and hydrologic variations, *J. Geophys. Res.,* 116, B04404, doi:10.1029/2010JB008156.

Ueno, T., T. Saito, K. Shiomi, B. Enescu, H. Hirose, and K. Obara (2012), Fractional seismic velocity change related to magma intrusions during earthquake swarms in the eastern Izu peninsula, central Japan, *J. Geophys. Res.,* 117, B12305, doi:10.1029/2012JB009580.

Wegler, U., B.-G. Lühr, R. Snieder, and A. Ratdomopurbo, (2006), Increase of shear wave velocity before the 1998 eruption of Merapi volcano (Indonesia), *Geophys. Res. Lett.,* 33, L09303, doi:10.1029/2006GL025928.

Wegler, U., H. Nakahara, C. Sens-Schönfelder, M. Korn, and K. Shiomi (2009), Sudden drop of seismic velocity after the 2004 M_w 6.6 mid-Niigata earthquake, Japan, observed with Passive Image Interferometry, *J. Geophys. Res.,* 114, B06305, doi:10.1029/2008JB005869.

Yamada, M., J. Mori, and S. Ohmi (2010), Temporal changes of subsurface velocities during strong shaking as seen from seismic interferometry, *J. Geophys. Res.,* 115, B03302, doi:10.1029/2009JB006567.

CHAPTER 3:

Changes in Seismic Velocity During the 2004–2008 eruption of Mount St. Helens, Washington

The content of this chapter is currently in preparation for publication as:

Hotovec-Ellis, A. J., J. E. Vidale, J. Gomberg, W. Thelen, and S. C. Moran (201X) Changes in seismic velocity during the 2004–2008 eruption of Mount St. Helens, Washington, *Journal of Geophysical Research Solid Earth,* in prep.

Abstract

Mount St. Helens began erupting again in late 2004 following an 18-year quiescence. Many swarms of repeating earthquakes accompanied the extrusion of a mostly solid dacite dome. In some cases the waveforms from these earthquakes evolved slowly, likely reflecting changes in the properties of the volcano that affect seismic wave propagation. We use coda wave interferometry to quantify small changes in seismic velocity structure (usually <1%) by determining how relatively condensed or stretched the coda is between two similar earthquakes. We then utilize several hundred distinct families of repeating earthquakes at once to create a continuous function of velocity change observed at any station in the seismic network. The high rate of earthquakes allows us to track these velocity changes on a daily or even hourly time scale. Significant changes in velocity were largest near the where the dome was being extruded and were likely related to shallow deformation as magma first worked its way to the surface. We find strong correlation between velocity changes and the inverse of the real-time seismic amplitude (RSAM) during the first three weeks of activity, suggesting fluctuations of

pressure in the shallow subsurface may have driven both seismicity and velocity change. Later in the eruption, we note additional changes in velocity associated with rainfall, explosions, deflation of the magma chamber at depth, extrusion of the lava dome at the surface, and changes in extrusive dynamics. Velocity changes during this eruption are clearly a result of a complex interplay of multiple effects and are not well-explained by any single factor alone. This highlights the need for complementary geophysical data when interpreting velocity changes.

1. Introduction

Following an 18-year quiescence, Mount St. Helens (MSH) began a continuous dome-building eruption in late September 2004 that lasted into early 2008. The eruption began with approximately three weeks of intense seismic activity, visible surface deformation, and small explosions prior to the first appearance of lava at the surface [Scott et al., 2008]. For the following three years, MSH extruded a dacite dome complex that consisted of seven semi-solid "spines" south of the 1980-86 dome. The continuous extrusion of lava was accompanied by prodigious amounts of seismicity, including the highly repeatable and regularly timed "drumbeat" earthquakes [e.g., Moran et al., 2008a; Thelen et al., 2008]. Although the waveforms of many of the earthquakes are similar (i.e., repeating), they are not always exact duplicates, and have been observed to evolve with time over the course of the eruption [Moran et al., 2008a; Thelen et al., 2008; Waite et al., 2008; Matoza et al., 2009]. In this study, we quantify changes in the waveforms of repeating earthquakes in terms of small relative changes in shear-wave velocity through coda wave interferometry [e.g., Snieder, 2002]. The rich seismic dataset and availability

of complementary geophysical time series offer a unique opportunity to study changes in material properties of a volcanic system over the course of an eruption through the lens of seismic velocity change.

Small temporal changes in seismic velocity structure have recently shown promise as a tool to monitor volcanoes via seismic interferometry [e.g., Brenguier et al., 2008; Haney et al., 2014]. However, studies involving velocity changes during volcanic eruptions and eruption precursors are still relatively rare. One of the first of these studies was about precursors to the eruptions of Merapi in 1992 [Ratdomopurbo and Poupinet, 1995] and 1998 [Wegler et al., 2006], though it was later shown by Sens-Schönfelder and Wegler [2006] that velocity changes at Merapi are dominated by seasonal groundwater fluctuations. Piton de la Fournaise has been the focus of several studies [e.g., Brenguier et al., 2008; Duputel et al., 2009], and recent work by Obermann et al. [2013] has improved the ability to localize velocity changes in space. Other volcanoes where this technique has been applied include Mt. Asama [Nagaoka et al., 2010] and Miyakejima [Anggono et al., 2012] in Japan, as well as Mount St. Helens via a proof-of-concept study by Sabra et al. [2006]. Finally, Ueno et al. [2012] also studied velocity changes due to magmatic intrusions in the eastern Izu peninsula.

It is thought that seismic velocity changes over days to weeks occur through the opening or closing of cracks and pore spaces [e.g., Tsai, 2011], so one might expect to observe velocity changes in association with inflation or deflation of the volcanic edifice. Indeed, velocities have been observed to decrease prior to eruption and increase over the course of eruptions in a pattern generally consistent with cycles of inflation and deflation [e.g., Anggono et al., 2012; Duputel et al., 2009] or shattering and healing [e.g., Li et al.,

2007] associated with magma injection and eruption. However, in some cases the timing of major velocity changes is inconsistent with geodetically observed deformation [Obermann et al., 2013; Nagaoka et al., 2010], suggesting more complex processes may be at work. Additionally, groundwater recharge [Sens-Schönfelder and Wegler, 2006; Martini et al., 2009], snow loading [Bennington et al., 2013], and nonlinear effects from strong shaking [Battaglia et al., 2012; Nishimura et al., 2000] also have been found to alter velocities at volcanoes. Hotovec-Ellis et al. [2014] documented that velocities at MSH between 1987 and 2004 are changed in response to all three of these factors (seasonal snow loading, seasonal shallow groundwater saturation, and shaking from the Nisqually earthquake) while finding no conclusive evidence for velocity changes related to inferred magmatic intrusions in the period between eruptions. This work extends that of Hotovec-Ellis et al. [2014] through the first year of the 2004-2008 eruption of MSH. During the first few days of the eruption, there is significant correlation between changes in seismic activity and velocity changes on the order of several percent, which are clearly related to volcanic processes. However, for the remainder of the eruption we found that although nearly all the aforementioned drivers of velocity change likely contribute, together they are still not sufficient to explain all the observed velocity changes. We interpret that velocity changes during this eruption are the result of a complex interplay of multiple factors such as fluid saturation, shallow pressure fluctuations, and possibly extrusion of the dome itself.

2. Data

MSH has been monitored by a relatively dense seismic network since 1980, with

stations jointly operated by the Pacific Northwest Seismic Network (PNSN) and Cascades Volcano Observatory. Several new stations were installed during the 2004-2008 eruption to supplement the permanent network [McChesney et al., 2008], and two temporary deployments (Broadband Array at Mount St. Helens [Waite et al., 2008] and Mount St. Helens Temporary Array [Thelen et al., 2008]) were also performed in 2005 However, most of these additional stations were short-lived relative to the duration of the eruption. For this study, we focus on waveform data from the permanent seismic network that was operational during the entire eruption to capture as complete a time series as possible. Specifically, we use stations YEL, EDM, HSR, SHW, JUN, STD, and SOS from the PNSN network (Figure 1a). All of these are vertical-component short-period

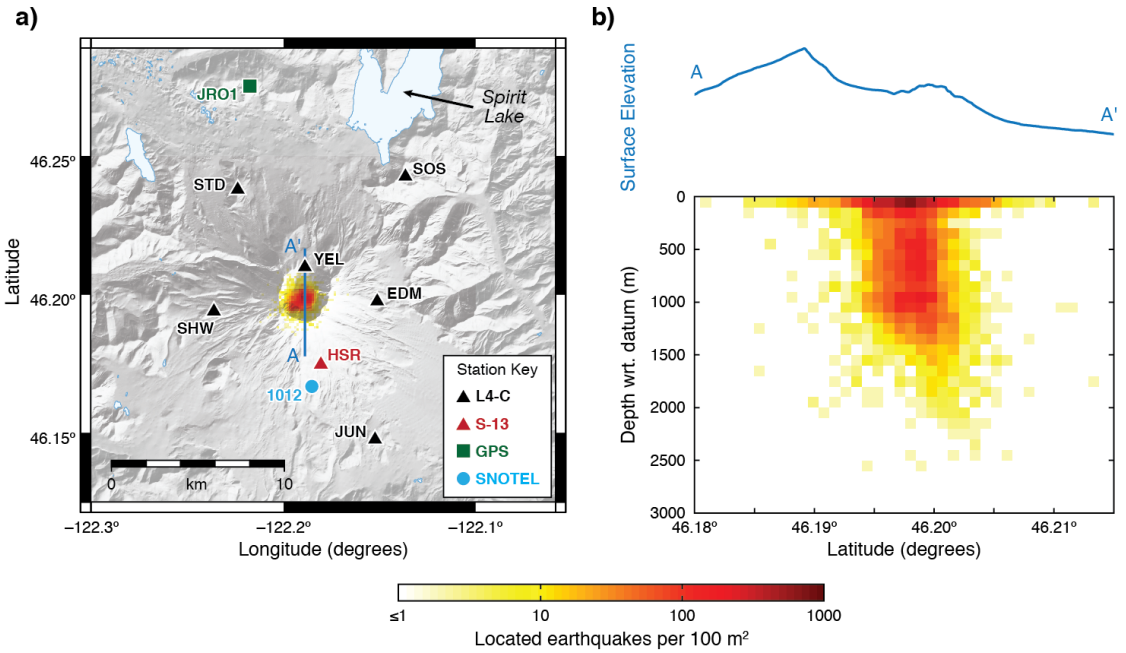

Figure: (a) Map with locations earthquakes during the eruption, plotted as a density map with earthquakes per 100 m x 100 m bin. Locations of stations used in the study are also plotted, with the exception of the stream gauge in Muddy River, located approximately 20 km southeast of the volcano. (b) Cross-section of located seismicity at MSH in PNSN catalog during the eruption, plotted with the same color and size scale as in (a).

stations with S-13 or L4-C seismometers, with continuous waveform data archived at the IRIS Data Management Center. Three permanent stations in the MSH network are not used in this study: 1) SEP was destroyed in the first explosion on October 1, and was replaced shortly after with a different sensor; in the interest of having a complete record for the eruption, we exclude this station from analysis. 2) FL2 was operational during the entire eruption, but had data quality issues through most of the period of interest. 3) CDF was also operational during the entire eruption, but had a low signal-to-noise ratio.

To investigate the relationship between changes in seismic velocity and other geophysical processes, we collected other geophysical data from the area. Locations of these instruments are also shown in Figure 1a. We use hourly weather data from SNOTEL station 1012 in Swift Creek and stream gauge data from Muddy River (approximately 20 km southeast of MSH, not included in Figure 1a) because snow depth and water were found to cause velocity changes in the MSH area between 1987-2004 [Hotovec-Ellis et al., 2014]. We also use GPS information from JRO, the only GPS station that was in continuous operation before the onset of the 2004-2008 eruption. Gas emissions [Gerlach et al., 2008], erupted volume derived from photogrammetry [e.g., Schilling et al., 2008], and geochemical data [e.g., Pallister et al., 2008] are also available, but on time scales that are too coarse for in-depth comparison. Finally, we also use real-time seismic amplitude (RSAM; Endo and Murray [1991]), frequency index [Buurman and West, 2010], and earthquake spectral amplitude (ESAM, a measure of P-wave spectra [Moran et al., 2008a]) to track evolution of earthquake behavior.

3. Methods

In order to perform coda wave interferometry on pairs of earthquakes, we require a catalog of earthquakes with similar waveforms (a result of events having similar mechanisms and being in similar locations). During the eruption, over one million small earthquakes occurred [Moran et al., 2008a]. At the peak of activity in late September and early October 2004, events were occurring every few seconds; later in 2005, events were still occurring at a rate of tens of events per hour. Due to time limitations, only ~10,000 of these events were located by the PNSN as a representative subset. Located earthquakes during this time period (Figure 1b) are shallow, concentrated at less than 2 km in depth, and showed signs of shallowing during the first few days of unrest [Moran et al., 2008a; Thelen et al., 2008]. Nearly all of the seismicity during the eruption, with the exception of rockfalls and explosions, was part of a set of repeating earthquake families [Thelen et al., 2008]. In this paper we rely upon the repeating-earthquake catalog of Thelen [2010], which contains 328,936 earthquakes sorted into 554 families of earthquakes with similar waveforms, with families lasting anywhere from several hours to several months. Two events are initially considered part of a family if the waveforms are have maximum cross-correlation values of 0.7 using a 9-second window on three or more stations. The combination process to build the catalog across multiple days requires comparison of a daily stack of similar events to the existing stack of the family if it was previously active, thus the final family may consist of some events that correlate at less than a 0.7 cross-correlation coefficient.

For each family, we bandpass-filter the waveforms from 0.5 to 10 Hz to improve signal-to-noise ratio and then align the waveforms to a common time axis. In theory it

would be straightforward to calculate the velocity change between every possible combination of pairs within a family, but in practice this becomes computationally expensive for large families of earthquakes (especially those with more than 10,000 members and multiple repetitions per minute) since the number of pairs scales as the squared number of earthquakes. Instead, we use hourly stacks and set the time of the stack to the median time of the earthquakes used to create it. Using hourly stacks of earthquakes also further improves the signal-to-noise ratio. In addition, the hourly stack averages out effects due to slight variations in source location and focal mechanism within that hour, and also averages out short-term (less than an hour) variations in seismic velocity. The averaging out of short-term velocity changes is only a factor during time periods where the velocity changes quickly; we find that it produces similar results to smaller runs done using all possible pairs over a short two-week time period.

To solve for change in velocity between pairs of hourly stacks, we use a stretching method [e.g., Hadziioannou et al., 2009; Kanu et al., 2013] applied to the coda of the two stacks. The stretching method expands and contracts the time axis of the second earthquake stack and finds the stretching factor that optimizes the correlation between the codas (Figure 2). This stretching factor is the basis for estimating the relative change in velocity between the two stacks, and is simply a constant that scales the time axis of the waveform. We use this stretching method instead of the time-windowing method [e.g., Snieder, 2002] because it has been shown to produce more stable results [Hadziioannou et al., 2009] and is less computationally expensive. We refine the stretching factor with greater precision using the objective function of Kanu et al. [2013]:

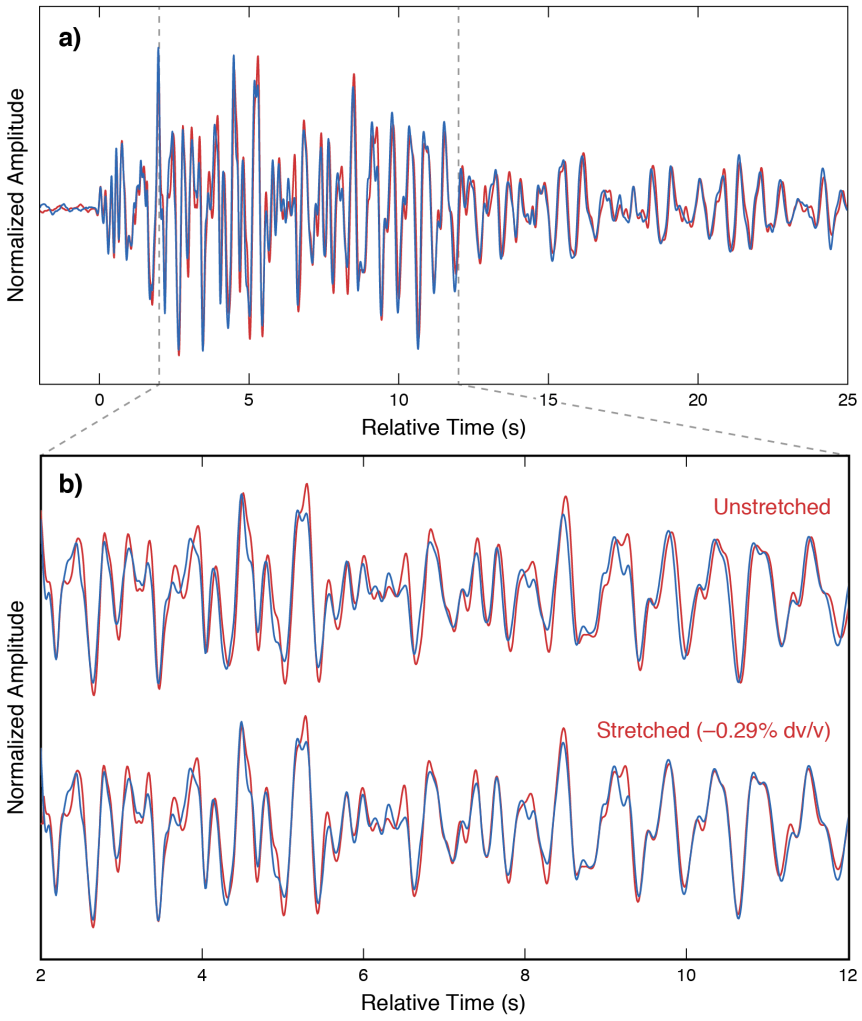

Figure 2: Illustration of stretching method. (a) Two hourly stacks of repeating earthquakes from the same family separated in time by less than one day, earlier hour plotted in blue. (b) Zoom in to the first 10 seconds used in the stretching window. Upper two waveforms are unstretched, with a slight visible difference between blue and red waveforms near the end. Lower blue waveform is the same, but the red waveform has been condensed by 0.29%, reflecting a decrease in velocity (%dv/v) between the times of the two waveforms.

$$R(\epsilon) = \left\| \hat{u}\big(t(1-\epsilon)\big) - u(t) \right\|_2 \tag{1}$$

where ϵ is the stretching factor related to velocity change (where velocity change is $(\epsilon - 1)$ * 100%), t is time, u is the reference seismogram, $\hat{u}$ is the seismogram to be

stretched, $R(\epsilon)$ is the objective function to be minimized, and $\|...\|_2$ is the L_2 norm.

We apply the stretching method over a 15-second window of the coda and require that the normalized cross-correlation coefficient in this window after stretching be above 0.8. The choice of 0.8 is a tradeoff between accuracy of measurement and number of pairs available that are above the cutoff. The accuracy of measurement may be contaminated by contributions to the coda due to changes other than velocity; changes in source location, mechanism, scattering properties, or simply added noise can also contribute to changes in coda. While none of these changes cause the coda to expand or contract directly, they can alter the amplitude and exact timing of coda wave arrivals, which contributes to lower cross-correlation coefficient. Thus, a high cross-correlation coefficient corresponds in general to fewer contributions from location and mechanism changes to the measured velocity change, as well as higher SNR levels.

We now have pairs of velocity changes for every combination of hourly stacks in each family, except for pairs that did not meet the minimum correlation-coefficient cutoff of 0.8. We used the regularized least-squares approach of Hotovec-Ellis et al. [2014] to solve for the smoothest continuous time history of velocity change that matches our pairwise observations. For the stations we consider in this paper, the number of velocity-change pairs ranged between ~800,000 and ~1,700,000. Since such large numbers create equally large matrices to invert, we capitalize on the fact that nearly all of the values in that matrix are zero and instead of solving for the inverse of the sparse matrix directly, we use the method LSQR [Paige and Saunders, 1982] to iteratively solve for the inverse matrix in a manner similar to conjugate gradients. Following the methods of Hotovec-Ellis et al. [2014], we choose the solution with the best tradeoff between roughness and

misfit, require that the iterative inversion must converge, and evenly discretize our solution in time. Choice of an appropriate discretization time scale is important, especially since the vast majority of our velocity-change pairs are only a few hours apart and do not span large changes in velocity. We chose one hour spacing, mirroring the approximate spacing of our hourly stacks. Such short spacing allows us to resolve large, sudden transients in velocity, but has the drawback of producing noisy results in the inversion step when there are few pairs during that hour. Additionally, since our data do not include any pairs that span the entire eruption, the inverted solution is most strongly controlled by the short time-scale pairs. We test how well an inversion dominated by short pairs is able to recover long-term trends by sampling a known function of velocity with time at the same pairs as HSR, add noise, and invert. The results of some of these inversion tests are shown in Figure 3. Even with significantly more noise than is contained in our data, we are still able to reliably recover trends over several months, assuming that there are no systematic biases in our data.

4. Results and Interpretations

We were able to resolve changes at an hourly time scale from the onset of repeating seismicity on September 23, 2004, through to the beginning of December 2005 (Figure 4a); after that, the earthquakes become too infrequent and the families too disconnected to invert for a continuous solution. This time period comprises all six explosions and the majority of extruded volume of lava. In general, velocity changes observed at each station are quite similar, with amplitudes decaying with distance from the dome. These observations indicate that we are seeing systematic velocity changes in a

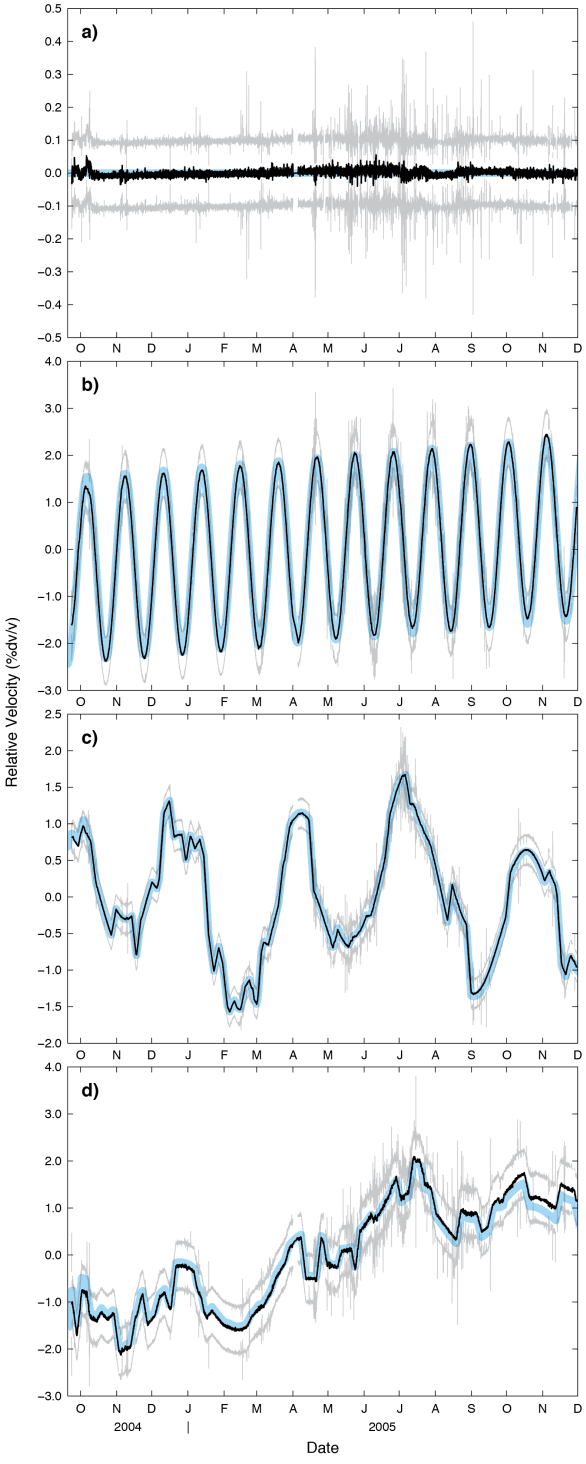

Figure 3: Inversion forward tests using the times of pairs from HSR on a synthetic (known) velocity change history (blue line). Resulting inversion is plotted in black, and spread of data around the inversion in grey. (a) Result of inversion with no velocity change (noise only). (b) Result of inversion with sinusoidal short-term velocity change with gradual, linear increase in velocity. (c) and (d) Result of inversions with gradual changes in velocity punctuated with step functions.

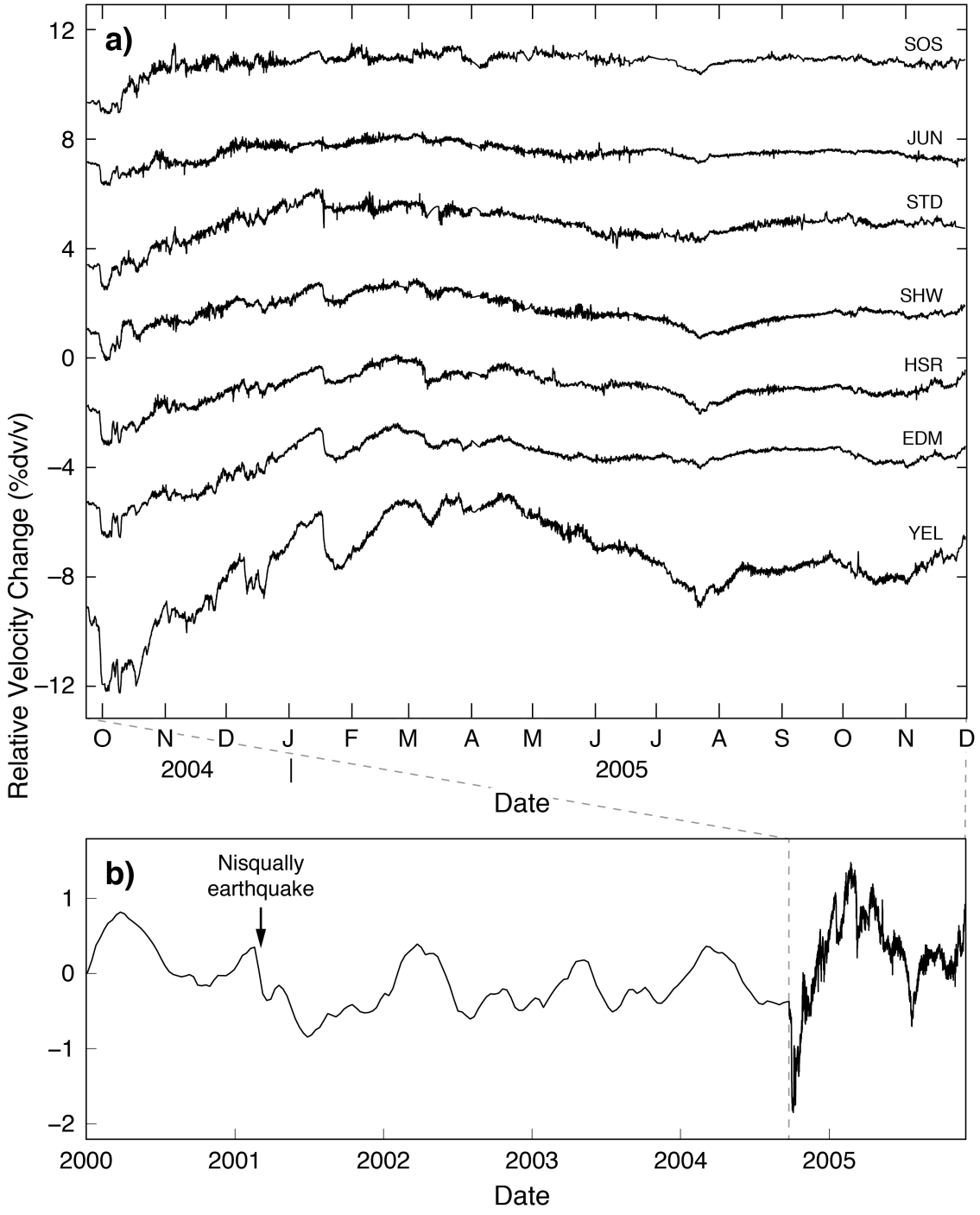

Figure 4: (a) Results of inversion by station, plotted by distance from dome with closest station (YEL) at bottom. (b) Extended time axis to include 2000-2006 for comparison at HSR (closest station used in both time periods), showing the amplitude of changes associated with the Nisqually earthquake and seasonal changes in snow loading from Hotovec-Ellis et al. [2014].

volume located near the dome. Station YEL, the closest station that was continuously operational through 2005 [McChesney et al., 2008], has the largest velocity change at 7.3%, with most of the change occurring over the first six months of the eruption. Station HSR, the closest station for which we have reliable pre-eruption estimates of velocity, has a 3.3% velocity change, nearly twice the maximum velocity change observed in the years prior to the eruption (Figure 4b).

We infer that most of the changes we observe are shallow or nearly surficial. We base that inference in part on the GPS-based and visual observations of surface deformation prior to and during extrusion of the new dome, and that confining pressure is lowest near the surface, allowing cracks to more easily open and close. Our bandpass filtering of the waveforms from 0.5 to 10 Hz in the processing will minimize the contribution from longer-period energy that samples greater depths due to the frequency-dependent depth sensitivity of the surface-wave portion of the coda waves (>100 m depth below 0.5 Hz), although the path of the body-wave energy in the coda is not well known. Furthermore, we note striking similarity of velocity change with RSAM, which reflects shallow seismicity and further bolsters the hypothesis that the velocity changes we observe are shallow (the implications of the relationship between velocity and RSAM are investigated in more detail in section 4.2). Finally, If the velocity changes are indeed concentrated at shallow depths, this corresponds to low absolute shear-wave velocities on the order of 2 km/s [Thelen et al., 2008], which should be the benchmark from which relative changes are converted to absolute change. That is, a small change in absolute velocity corresponds to a large change in relative velocity when absolute velocities are small.

In the following sections, we investigate causes for the observed velocity change by comparing velocity change to other observables. We base most of our interpretations on the premise that velocity change is primarily dependent on volumetric strain and the opening/closing of cracks and pore spaces. For ease of interpretation, we use the normalized mean of velocity changes to focus on what is common to all stations.

4.1. Estimation of change due to deflation of magma chamber at depth

First we investigate the possible causes for the broad velocity increase over the duration of the eruption. Such an increase in velocity could be due in part to far-field (>5 km distance) deflation as the magma chamber at depth depressurizes. Figure 5 shows the movement of JRO1 to the south (toward MSH) with time compared with the average normalized velocity change across the network. Displacements at JRO1 and other GPS

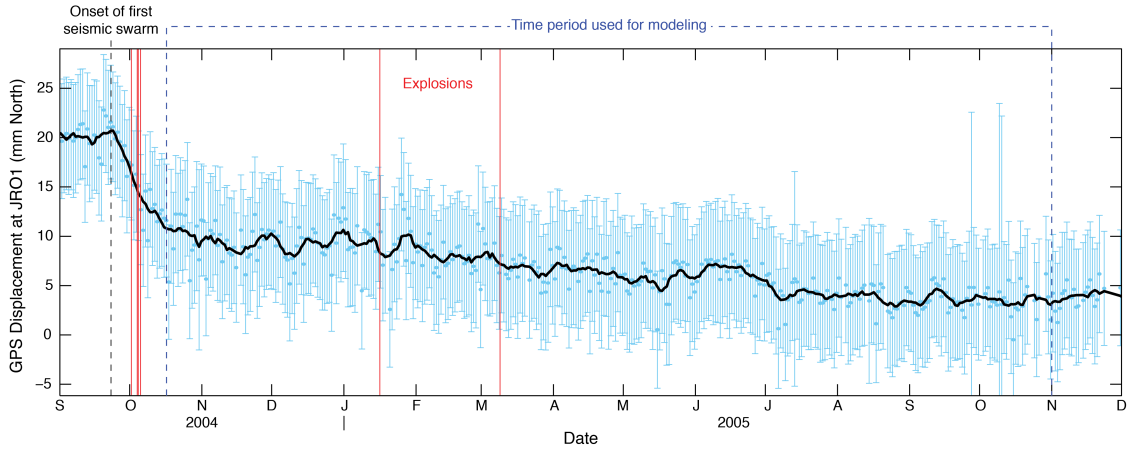

Figure 5: GPS time-series of displacement in the N-S direction at JRO1, the closest GPS station to MSH that was operational prior to the eruption. Blue dots with 1-σ error bars are the corrected displacements; heavy black line is a 10-day moving average. Southward displacement begins at the onset of the first seismic swarm on September 23, 2004, and exponentially decays after. Explosions are noted, as well as the 1-year period of displacement used to estimate velocity change.

stations approximately follow an exponential decay with time [Lisowski et al., 2008]. Although the velocity change and displacement time-series are visually different, there is still an overall increase in velocity on all stations across this time period, which could be due in part to contraction of cracks near the surface caused by deflation of the magma chamber at depth.

We estimate the expected change in velocity from the GPS-observed deformation field by first assuming a simple model that fits the observed displacements. Specifically, we use the analytic solution for an oblate spheroid magma chamber described in Lisowski et al. [2006] and Bonaccorso and Davis [1999]:

$$u_r = \frac{\alpha^2 \Delta P}{4\mu r}\left(\frac{c_1^3}{R_1^2} + \frac{2c_1(-3+5\nu)}{R_1} + \frac{5c_2^3(1-2\nu) - 2c_2 r^2(-3+5\nu)}{R_2^3}\right) \tag{2}$$

$$u_t = 0 \tag{3}$$

$$u_z = -\frac{\alpha^2 \Delta P}{4\mu}\left(\frac{c_1^2}{R_1^2} + \frac{2(-2+5\nu)}{R_1} + \frac{c_2^3(3-10\nu) - 2r^2(-2+5\nu)}{R_2^3}\right) \tag{4}$$

$$\varepsilon_{rr} = \frac{\partial u_r}{\partial r} \tag{5}$$

$$\varepsilon_{tt} = \frac{u_r}{r} \tag{6}$$

$$\varepsilon_{zz} = -\frac{\nu}{1-\nu}\left(\varepsilon_{rr} + \varepsilon_{tt}\right) \tag{7}$$

where u is displacement in the radial, tangential, and up directions; ε is strain; ΔP is change in pressure; α is the radius of the chamber; c_1 is the depth of the top of the chamber; c_2 is the depth to the bottom of the chamber; r is horizontal distance from the

center of the chamber; $R_1 = \sqrt{r^2 + c_1^2}$ and $R_2 = \sqrt{r^2 + c_2^2}$ are the distances from a point on the surface to the top and bottom of the chamber, respectively; v is Poisson's ratio; μ is the elastic modulus. We use values listed in Table 1 from Lisowski et al. [2006], which are a fair fit to the observed displacements in Figure 6a.

ΔP	v	μ	c_1	c_2	α
−11 MPa	0.25	1.0e10 Pa	6500 m	11500 m	500 m

Table 1. Parameters for estimating surface strain due to a pressure decrease at depth

The corrected observed displacements from Lisowski et al. [2008] and the modeled displacements are shown in Figure 6a, and modeled strains are shown in Figure 6b. Following Hotovec-Ellis et al. [2014] and Tsai [2011], we estimate velocity change from strain from a simplified version of Equation 11 of Hughes and Kelly [1953]:

$$\frac{\mathrm{dv}_{12}}{\mathrm{v}_{12}} = \frac{2m\theta + n\varepsilon_{33}}{4\mu} \tag{8}$$

where m and n are two of the three Murnaghan third-order elastic constants, μ is the shear modulus, θ is dilatation or volumetric strain, and ε_{33} is strain perpendicular to the direction of travel and polarization of the wave. Based on the sensitivity of velocity to snow loading as demonstrated by Hotovec-Ellis et al. [2014], we estimate that the Murnaghan constants m and n are approximately −1x10e4. This calculation produces the estimated velocity changes at the surface with distance from the dome in Figure 6c. Our

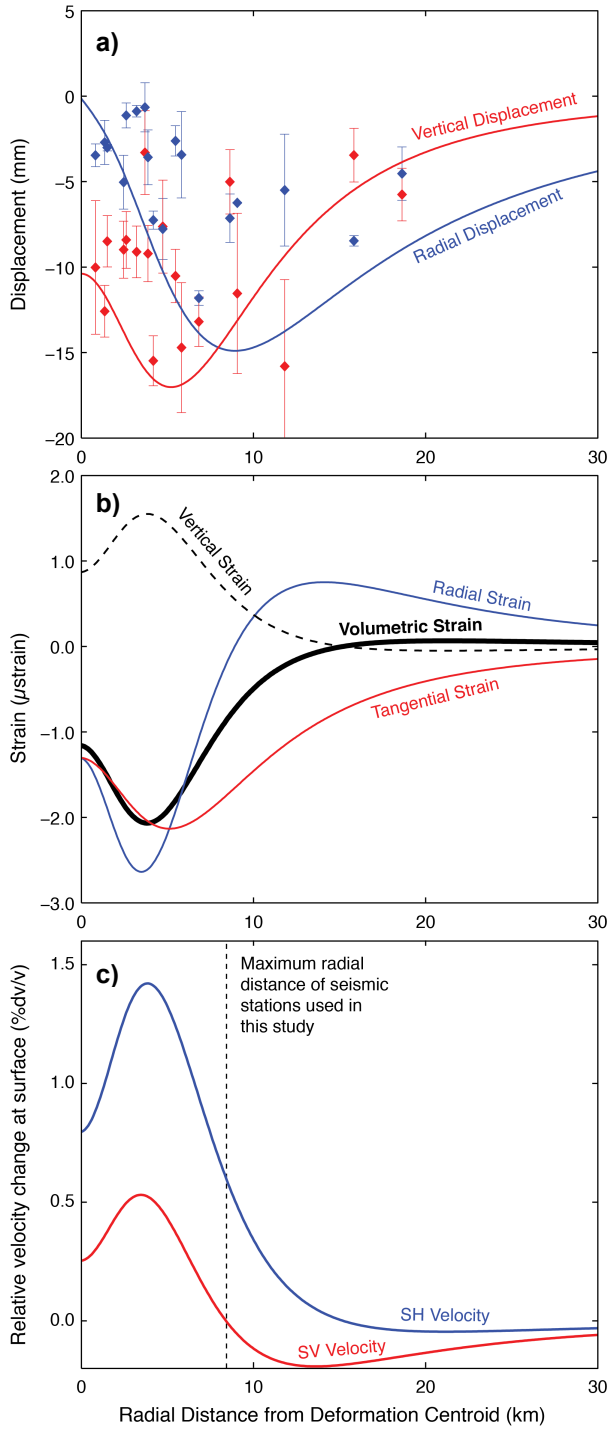

Figure 6: GPS displacement to velocity estimation. (a) Observed displacements from all GPS stations installed by October 11, with modeled displacement for decrease in pressure in an oblate spheroid magma chamber at depth. (b) Strains from modeled displacements. (c) Expected relative velocity changes based on modeled displacements and strains. This change is only for October 11, 2004 to October 11, 2005, and reflects approximately half the total deformation over the entire eruption.

In the next sections, we divide the eruption into three segments based on the behavior of extrusion and compare the record of velocity change with other data streams to further evaluate other causes of velocity change than simple deflation. The dates of these divisions correspond to the phases of Vallance et al. [2008] (i.e., the first division A spans phases 1 and 2, the second B is phase 3, and C, the last spans phases 4 and 5), which broadly represent changes in the behavior of lava extrusion. For reference, we include the full time span of velocity changes against other observations, and note the division of phases in Figure 7.

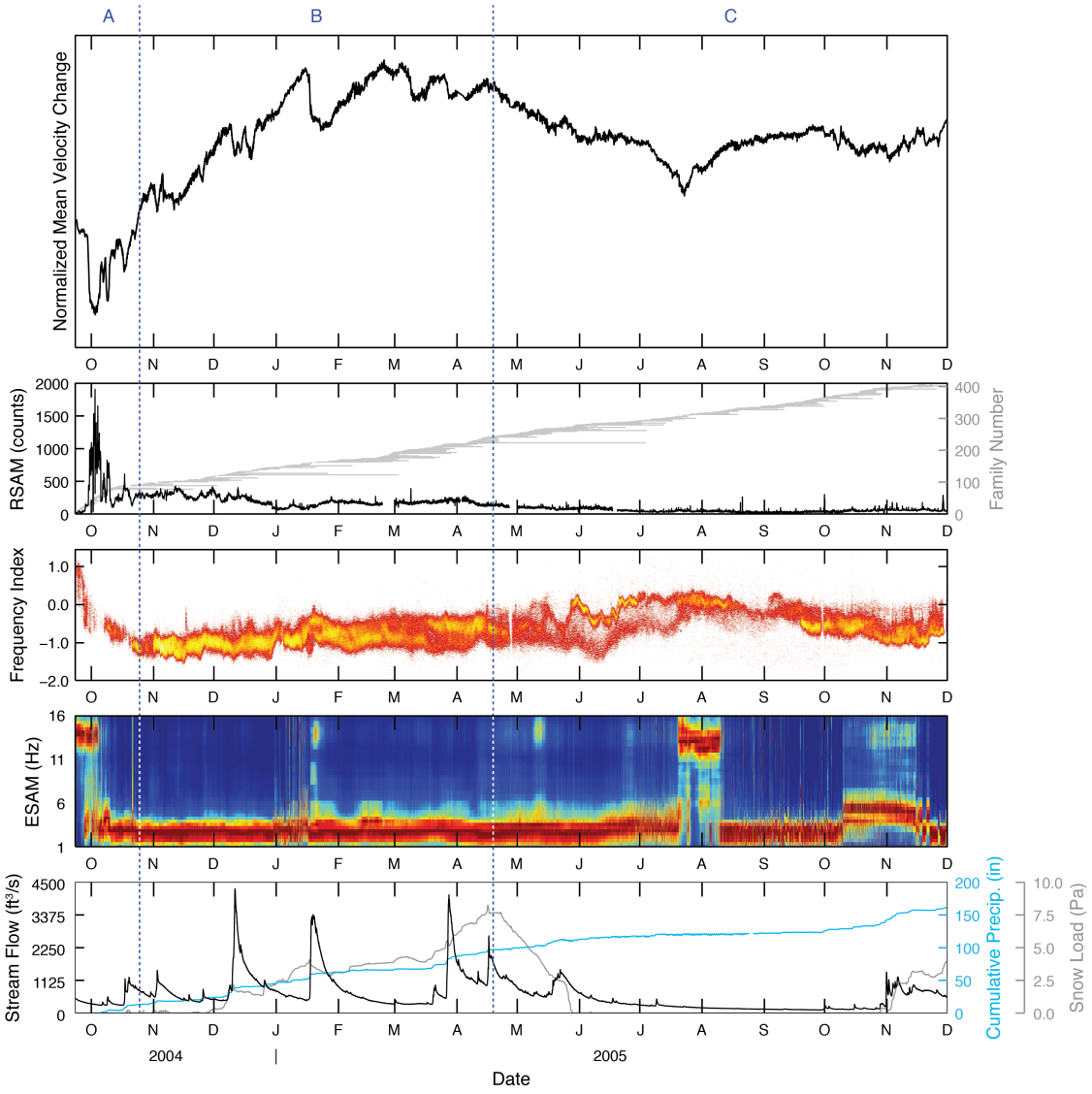

Figure 7: Comparison of mean velocity change across all stations with secondary seismic data and weather data. Top panel is normalized mean velocity change across the network. Second from top is RSAM (real-time seismic amplitude measurement) and bar plot of repeating earthquake families used; each bar is a different family and endpoints represent the start and end times. Middle plot is a density plot of frequency index, a comparison of energy in upper and lower bands of frequency, where higher indexes correspond to more energy in higher frequencies (see Buurman and West [2010] for details, plot courtesy of Silvio de Angelis). Second from bottom is ESAM (earthquake spectral amplitude measurement), which are the normalized spectra of the P-wave of each earthquake. Bottom panel is weather data; snow load and cumulative precipitation are from SNOTEL site 1012 in Swift Creek (see Figure 1 for location), stream flow is from gauge in Muddy River to the southeast of MSH. Blue dashed lines indicate time divisions for sections 4.2, 4.3, and 4.4. Time axis is delimited by month of the year.

4.2. Velocity changes associated with vent clearing and extrusion of initial spines (September 23, 2004 – October 25, 2004)

Large and striking velocity changes coincide with the start of the precursory sequence, so we compare the history of velocity change and precursory events in detail. A swarm of earthquakes beneath the dome of MSH and geodetically observed deflation at JRO1 began on September 23, 2004. The seismicity waned a few days afterward, and then resumed with more frequent, larger, and lower frequency earthquakes on September 26 [Moran et al., 2008a]. Around this time, a visible welt was observed at the surface just to the south of the 1980-86 dome where lava would eventually work its way to the surface [Dzurisin et al., 2008]. From October 1 through 5 a series of four phreatic explosions occurred as well as a significant tremor episode, most of which were followed by a pause or decline in seismicity and tremor [Moran et al., 2008b]. The dominant frequency content of earthquakes gradually shifted from higher frequencies to lower frequencies over the course of the first 1-2 weeks of the precursory phase [Moran et al., 2008a]. After the last explosion on October 5, earthquake magnitudes waxed and waned in two bursts on October 6-7 and October 8-9, which were followed two days later by the first lava reaching the surface on October 11 [Scott et al., 2008; Vallance et al., 2008]. The eruption of "Spine 1" was followed shortly after by the appearance of Spine 2 and probable subterranean and subglacial intrusion of Spine 3 [Vallance et al., 2008]. These events and associated data are summarized in Figure 8.

Our computed velocity change curves show a significant velocity decrease that occurred in association with the onset of precursory seismicity. This decrease is most obvious on YEL (0.7%), but it can also be seen on stations HSR (0.3%) and SHW (0.2%).

However, this initial decrease pales in comparison to the much larger drop beginning on September 27, where velocities decreased by more than 2% at YEL, more than 1% at HSR, SHW, and EDM, and more than 0.5% at STD and JUN (Figure 8). This decrease is coincident with the second increase in seismic activity, and tapers off just before the first

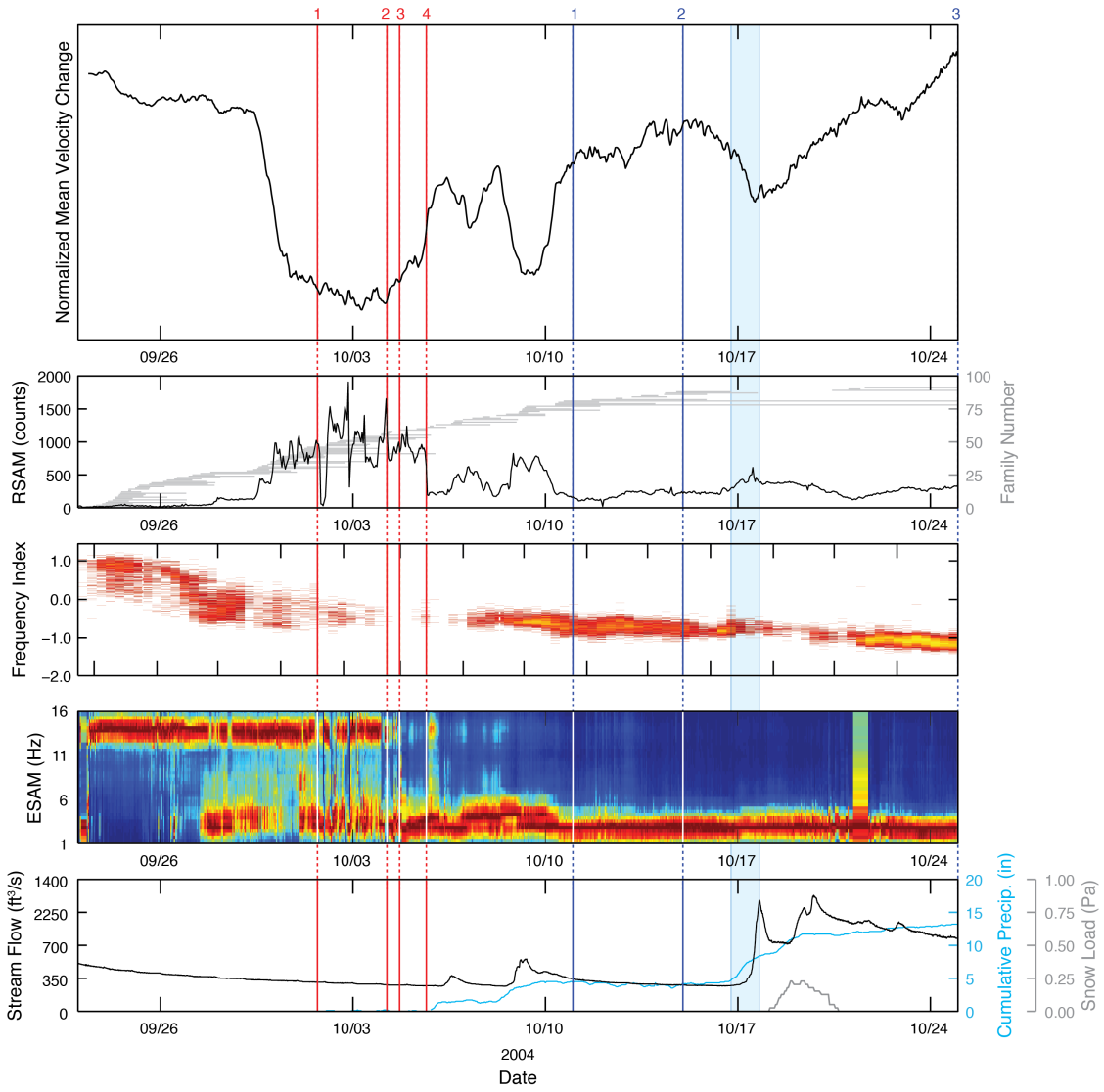

Figure 8: Comparison of velocity change with other time-series during Period A. Same layout as Figure 7. Blue filled box is a rainstorm that corresponds to a decrease in velocity, with start defined from increase in precipitation at Swift Creek, end at peak in stream flow in Muddy River, and must have at least 3 inches of cumulative precipitation. Dark blue lines are the start of each new spine extrusion, and red lines are explosions.

explosion on October 1. Velocities increase with the fourth explosion on October 5, and follow a similar pattern as overall seismic amplitudes through October 9 with two cycles of decreased and increased velocities. The striking inverse correlation between seismic amplitude and velocity change is illustrated in Figure 9a, where velocity is plotted against RSAM values computed at 10-minute intervals, with RSAM values inverted to better show the anti-correlation. In Figure 9b, we show the normalized zero-lag cross-correlation coefficient of velocity against -1*RSAM for September 23 thru October 25, plotted such that the window of correlation begins at the first observation of velocity change and expands with time. Correlation peaks at 0.97 after the first explosion on October 1 and remains around 0.9 for the rest of this time period. Correlation drops off significantly after October 25.

Our interpretation is that both the seismicity and velocity are changing in response to shallow fluctuations in pressure as magma works its way to the surface. Increases in pressure cause the rates of earthquakes to increase and cracks to be propped open, causing a decrease in velocity. This inflation is distinct from the longer-term GPS-observed deflation, and is likely more shallow and localized than the deeper deflation of the magma chamber. As pressure is released in the system during explosions, cracks close and velocity increases again, in association with temporary seismicity declines. Once the first lava reached the surface on October 11 the correlation between RSAM and velocity becomes weaker, and we presume pressure in the sampling volume of the coda waves remains more or less constant through the rest of the eruption as gases and magma have an open path to the surface.

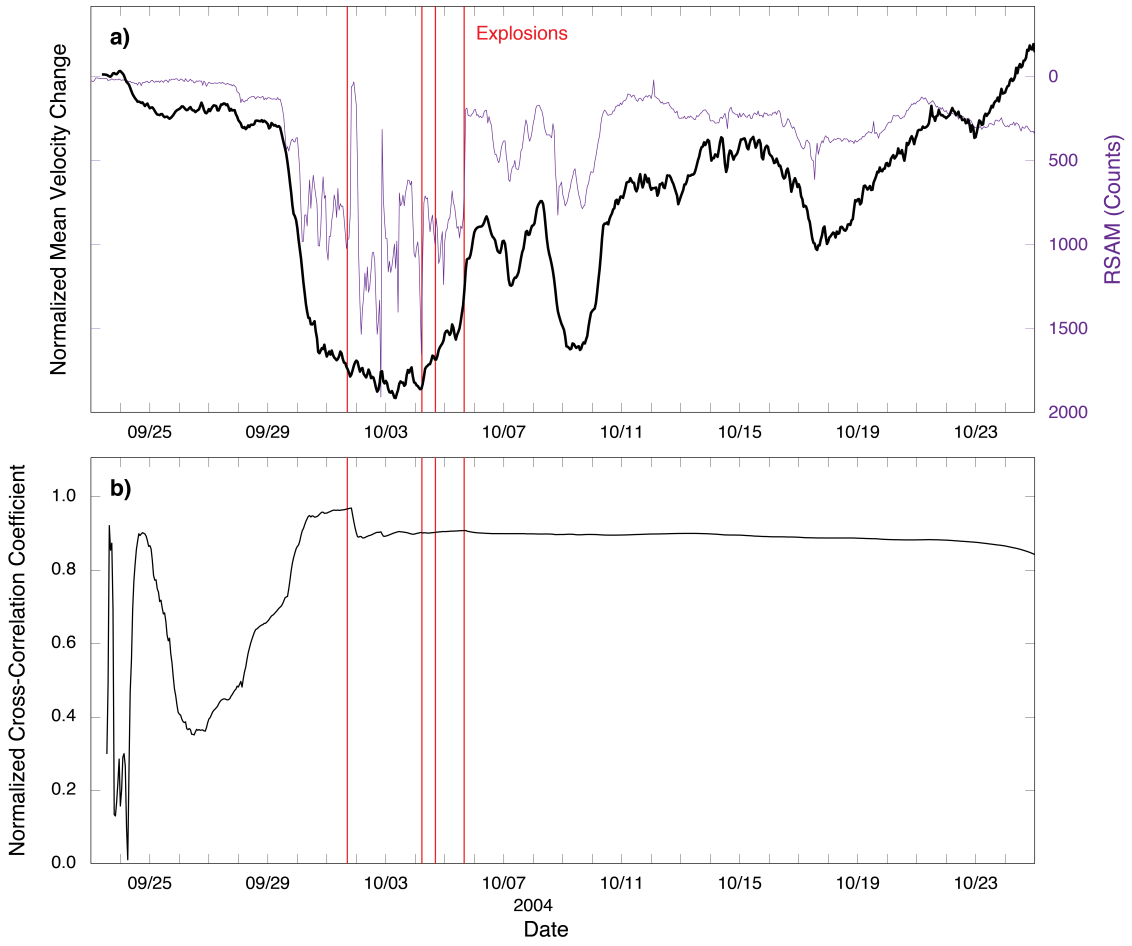

Figure 9: (a) Overlay of mean velocity change (black) and RSAM (purple, increasing RSAM down to emphasize anti-correlation) during Period A. (b) Correlation of velocity with RSAM as a function of time, where the start of the correlation window is at the beginning of the velocity change record and the end expands with time in the plot. The two do not become highly correlated until September 30, but remain correlated above 0.8 through much of the rest of the period.

We find no clear changes associated with changes in frequency content of earthquakes. Seismic velocities generally increase through extrusion of Spines 1 and 2, with a slight decrease in velocity following the appearance of Spine 2. There is a small rainstorm on October 17 that appears as an increase in RSAM due to wind noise, but it is unclear here whether there is a causal effect on velocity as the velocity began to drop well

before the storm. We elaborate on velocity changes more likely associated with the weather in the next section.

4.3. Velocity changes associated with recumbent growth of whaleback spines and rainstorms (October 25, 2004 – April 19, 2005)

Velocities during this phase primarily increase. As discussed in section 4.1, we presume at least part of the increase in velocity is due to the deflation of the edifice, perhaps with a component of healing recently formed cracks. Another possible contribution to the increase might be closure of cracks under the new dome due to the growing weight of extruded lava, beginning with the extrusion of Spine 3. Spine 3 extruded nearly horizontally toward the south, eventually coming into contact with southern crater wall mid-November (T1 in Figure 10) and fracturing and decoupling from the vent in mid-December (T2 in Figure 10) [Vallance et al., 2008]. The first two major transitions in the behavior of Spine 3 (T1 and T2) seem to be temporally correlated with small decreases in velocity, consistent with the visual observation of fractures in the dome. The second fragment that detached from the dome in early December was considerably larger than the first, which is in parallel with a larger velocity change signal at this time. However, the break-up of Spine 4 (T3) in early April does not have an obvious decrease in velocity associated with it, even though large fractures visibly grew on the surface, indicating that velocity changes may not be related to the state of individual extruded spines.

The most prominent decrease in velocity in this phase occurs after explosion 5, and explosion 6 also has a decrease in velocity associated with it. Because the sense of

velocity change for these two explosions is opposite to that of explosion 4, it is therefore inconsistent with the velocity change being the result of a release of pressure alone. One possible explanation is that the explosions damage the conduit and create new cracks. Both of these explosions are further complicated by more gradual decreases in velocity

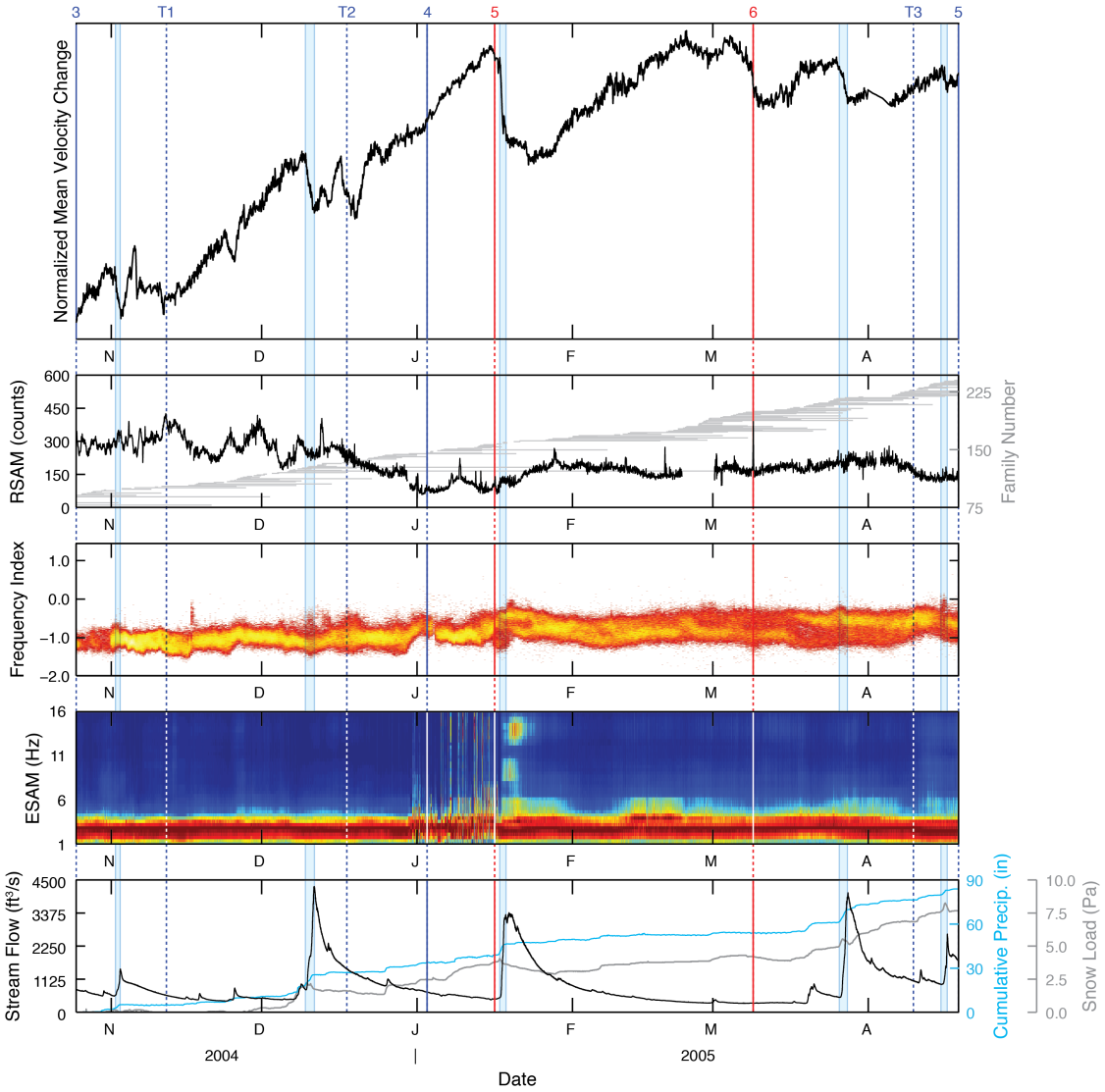

Figure 10: Comparison of velocity change with other time-series during Period B. Same layout as Figures 7 and 8. Dashed lines are important transitions in the behaviors of spine extrusion. T1 is where Spine 3 begins pushing against south crater wall. T2 is where Spine 3 "deflects off south crater wall, fractures, breaks up, and decouples from source" [Vallance et al., 2008]. T3 is where Spine 4 also "encounters south crater wall, fractures, and decouples from source."

around the times of the explosions. In neither case do we believe the gradual changes around the times of these explosions to be due to smoothing in the inversion, at least not at the timescales of days for these changes. Explosion 6 has what could be a precursory decrease in velocity in the ~5 days before the explosion, as well as a ~2 hour long precursory increase in seismicity that slowly recovers post-explosion [Moran et al., 2008b]. The increase in seismicity prior to the explosion could have been related to increasing pressure, the explosion may have released some of that pressure, but the net effect with the second crack opening mechanism was still a decrease in velocity.

Explosion 5 is associated with the largest short-term transient during this time period, yet the explosion itself was significantly less energetic than Explosion 6. The initial small velocity decrease associated with the explosion preceded a much larger velocity decrease by several hours, coincident with the onset of rainfall. We believe that this second, larger decrease is related to the infiltration of rainwater into the already opened and newly formed cracks from the explosion. However, we cannot explain the decrease in velocity by precipitation alone, since the amplitude of velocity change is larger than other small decreases in velocity that also occur around times of precipitation.

We define the onset of a rainstorm (blue shaded regions of Figure 10) from the first break in slope of the cumulative precipitation record, the end by peak stream flow in Muddy River after which flow rates slowly decay, and further define that a rainstorm must have at least 3" of cumulative precipitation. Velocities decrease during a rainstorm due to increased fluid saturation, which should prop open shallow pore spaces. This effect has been seen in laboratory experiments [Grêt et al., 2006], and there is other evidence observed in the field [e.g., Hotovec-Ellis et al., 2014; Sens-Schönfelder and

Wegler, 2006]. We noted in previous work that snow loading could also have a considerable effect on seismic velocity; however, the winter of 2004/2005 had approximately half the snowfall of previous years. As a result, we expect only a minimal effect on velocity change, on the order of perhaps a few tenths of a percent at the highest elevation stations.

4.4. Velocity changes associated with spines thrusting over previous spines (April 19, 2005 and onward)

There were no explosions during this last period, nor were there many rainstorms (Figure 11). Long-term GPS-measured deflation and steady lava extrusion continued; however, seismic velocities decreased significantly through mid-July. Snow loading decreases through this time period as it melts, but the amplitude and timing of the change in load is insufficient to entirely account for the downward trend. Starting in late November 2005 seismic velocities increase again coincident with the onset of snow accumulation. If we were able to resolve velocity change through to the next year, we would expect seasonal effects to dominate, since precipitation was much greater over the winter of 2005-2006 than 2004-2005.

Having ruled out changes in snow depth as a cause for velocity changes, we suggest the gradual decrease in velocity from mid-April to late July reflects a difference in the extrusion style of Spine 5 compared to the other spines. Particularly in July, Spine 5 featured a significant amount of internal deformation [Vallance et al., 2008; Moran et al., 2008a] that we argue tended to open more cracks than it closed. In particular, Spine 5 thrust over the remnants of Spine 4, became gradually steeper with time, and was prone

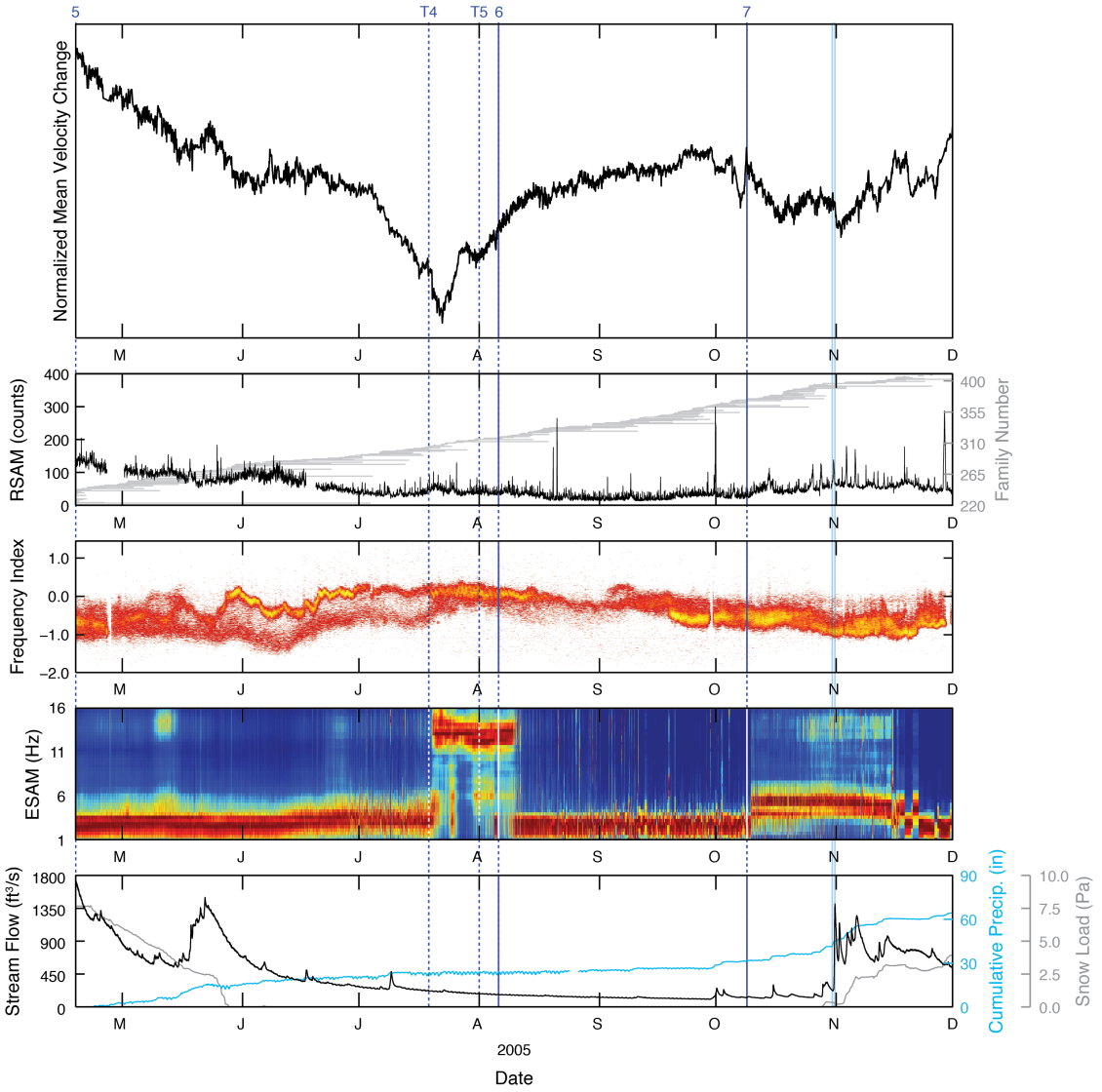

Figure 11: Comparison of velocity change with other time-series during Period C. Same layout as Figures 7, 8, and 10. T4 is when Spine 5 "crumbles to feed rockfall avalanches and slumping events." T5 is when Spine 5 "fractures near its source and begins to slump." [Vallance et al., 2008]

to crumbling as it grew [Vallance et al., 2008]. Spine 5 continued to crumble through late July and early August (T4), before fracturing near its source and slumping (T5) prior to the emergence of Spine 6. Additionally, there were also changes in the behavior of seismicity during the extrusion of Spine 5 and its transition to Spine 6 [Moran et al., 2008a]. Specifically, although the drumbeat earthquakes dominate the seismicity, there is

a separation of frequency content and amplitude between the drumbeats and other families of smaller earthquakes (i.e., subevents [Matoza and Chouet, 2010]), seen as a separation in frequency index in Figure 11 that is unique to this time period. Also, the amplitude of earthquakes declines while the spacing between earthquakes grows, even though magma flux remained roughly constant. Moran et al. [2008a] cite changes in clamping forces related to the angle of extrusion, changes in the locus of extrusion, or changes in frictional properties along the conduit margin as possible causes.

We further note the sharp decrease in velocity on July 19 coincides with the onset of a higher frequency, "hybrid" swarm of earthquakes identified by Moran et al. [2008a] (see ESAM inset in Figure 11). This swarm continued through the transition between Spines 5 and 6 by differential shearing, and encompasses the sharp "v"-shaped transition from decrease to increase in seismic velocities. However, the end of the hybrid swarm does not appear to be related to a change in velocity. Another, weaker hybrid swarm seems to accompany a change in the trend of velocity change later in October, related to the growth of Spine 7 [Moran et al., 2008a]. Although there may be some temporal correlation between the behavior of seismicity and velocity change, it is not nearly as clear as during the vent-clearing stage.

5. Conclusions

We used subtle changes in the waveforms of thousands of repeating earthquakes during the recent dome-building eruption of MSH to investigate changes in the shallow structure of the volcano with hourly temporal resolution. Specifically, we use coda wave interferometry to solve for relative velocity changes, and relate these to other geophysical

observables in the framework that volumetric expansion and the opening of cracks and pore spaces decreases velocity and vice versa. Velocity changes related to shallow pressure fluctuations dominate the vent-clearing phase of eruption, which we base on the high correlation between velocity change and seismic amplitude. That is, increases in pressure create more earthquakes and prop open shallow cracks by inflation, causing a decrease in velocity near the surface; then when pressure is released in explosions or slower effusion, seismicity declines and velocities increase. We find several short-term velocity decreases associated with the largest rainstorms during the study period, but otherwise there is little effect of weather during most of the eruption in large part due to an unusually mild winter. Otherwise, the remaining changes in velocity are likely due in part to the deflation of the volcano or subtle changes in extrusion of the new dome. However, the exact relationship between velocity change and dome extrusion is still unclear, and could be a combination of several effects.

To this point, we have offered explanations for the most obvious features in the velocity change record; however, many features remain ambiguous even given the variety of other data we have available to compare to. The prospect of using velocity changes to monitor volcanoes is exciting, but we caution that weather data, deformation, and secondary seismic information are still necessary to interpret the observed signals, as the myriad of possible sources is still poorly constrained. We have shown that precipitation- and snow-related changes are relatively easy to identify given nearby weather data with sufficient resolution, and shallow pressurization is a likely culprit when velocities and seismicity change in sync, but more work is necessary to identify other processes uniquely.

References

Anggono, T., T. Nishimura, H. Sato, H. Ueda, and M. Ukawa (2012), Spatio-temporal changes in seismic velocity associated with the 2000 activity of Miyakejima volcano as inferred from cross-correlation analyses of ambient noise, *J. Volcan. Geotherm. Res., 247–248,* 93–107, doi:10.1016/j.jvolgeores.2012.08.001.

Battaglia, J., J. -P. Métaxian, and E. Garaebiti (2012), Earthquake-volcano interaction imaged by coda-wave interferometry, *Geophys. Res. Lett., 39,* L11309, doi:10.1029/2012GL052003.

Bennington, N. L., M. M. Haney, S. De Angelis, and C. H. Thurber (2013), Relative velocity changes using ambient seismic noise at Okmok and Redoubt volcanoes, Alaska, Abstract S53E-06 presented at 2013 Fall Meeting, AGU, San Francisco, Calif., 9-13 Dec.

Bonaccorso, A., and P. M. Davis (1999), Models of ground deformation from vertical volcanic conduits with application to eruptions of Mount St. Helens and Mount Etna, *J. Geophys. Res., 104,* B5, 10531–10542.

Brenguier, F., N. M. Shapiro, M. Campillo, V. Ferrazzini, Z. Duputel, O. Coutant, and A. Nercessian (2008), Towards forecasting volcanic eruptions using seismic noise, *Nature Geosci., 1,* 126–130, doi:10.1038/ngeo104.

Buurman, H. and M. West (2010), Seismic Precursors to Volcanic Explosions During the 2006 Eruption of Augustine Volcano, in *The 2006 Eruption of Augustine Volcano,* edited by J. A. Power, M. L. Coombs, and J. T. Freymueller, *Prof. Paper 1769,* chap. 2, pp. 41–57, U.S. Geol. Surv., Reston, Va.

Duputel, Z., V. Ferrazzini, F. Brenguier, N. Shapiro, M. Campillo, and A. Nercessian (2009), Real time monitoring of relative velocity changes using ambient seismic noise at the Piton de la Fournaise volcano (La Réunion) from January 2006 to June 2007, *J. Volcan. Geotherm. Res., 184,* 164–173, doi:10.1016/j.jvolgeores.2008.11.024.

Dzurisin, D., M. Lisowski, M. P. Poland, D. R. Sherrod, and R. G. LaHusen (2008), Constraints and Conundrums Resulting from Ground-Deformation Measurements Made During the 2004-2005 Dome-Building Eruption of Mount St. Helens, Washington, in *A Volcano Rekindled: The Renewed Eruption of Mount St. Helens, 2004–2006,* edited by D. R. Sherrod, W. E. Scott, and P. H. Stauffer, *Prof. Paper 1750,* chap. 14, pp. 281–300, U.S. Geol. Surv., Reston, Va.

Endo, E., and T. Murray (1991), Real-time Seismic Amplitude Measurement (RSAM): a volcano monitoring and prediction tool, *Bull. Volcan., 53,* 533–545, doi: 10.1007/BF00298154.

Gerlach, T. M., K. A. McGee, and M. P. Doukas (2008), Emission Rates of CO_2, SO_2, and H_2S, Scrubbing, and Preeruption Excess Volatiles at Mount St. Helens, 2004–2005, in *A Volcano Rekindled: The Renewed Eruption of Mount St. Helens, 2004–2006,* edited by D. R. Sherrod, W. E. Scott, and P. H. Stauffer, *Prof. Paper 1750,* chap. 26, pp. 543–571, U.S. Geol. Surv., Reston, Va.

Grêt, A., R. Snieder, and J. Scales (2006), Time-lapse monitoring of rock properties with coda wave interferometry, *J. Geophys. Res.,* 111, B03305, doi:10.1029/2004JB003354.

Hadziioannou, C., E. Larose, O. Coutant, P. Roux, and M. Campillo (2009), Stability of monitoring weak changes in multiply scattering media with ambient noise correlation: Laboratory experiments, *J. Acoust. Soc. Am., 125,* 3688–3695.

Haney, M., A. J. Hotovec-Ellis, N. L. Bennington, S. De Angelis, and C. Thurber (2014), Tracking changes at volcanoes with seismic interferometry, *Encyclopedia of Earthquake Engineering, in review*.

Hotovec-Ellis, A. J., J. Gomberg, J. E. Vidale, and K. C. Creager (2014), A continuous record of intereruption velocity change at Mount St. Helens from coda wave interferometry, *J. Geophys. Res., 119,* 2199–2214, doi:10.1002/2013JB010742.

Hughes, D. S., and J. L. Kelly (1953), Second-Order Elastic Deformation of Solids, *Phys. Rev.,* 92, 1145–1149.

Kanu, C. O., R. Snieder, and D. O'Connell (2013), Estimation of velocity change using repeating earthquakes with different locations and focal mechanisms, *J. Geophys. Res.,* 118, 1–10, doi:10.1002/jgrb.50206.

Li, Y.-G., P. Chen, E. S. Cochran, and J. E. Vidale (2007), Seismic velocity variations on the San Andreas fault caused by the 2004 *M*6 Parkfield Earthquake and their implications, *Earth Planets Space,* 59, 21–31.

Lisowski, M., D. Dzurisin, R. P. Denlinger, and E. Y. Iwatsubo (2008), Analysis of GPS-Measured Deformation Associated with the 2004–2006 Dome-Building Eruption of Mount St. Helens, Washington, in *A Volcano Rekindled: The Renewed Eruption of Mount St. Helens, 2004–2006,* edited by D. R. Sherrod, W. E. Scott, and P. H. Stauffer, *Prof. Paper 1750,* chap. 15, pp. 301–333, U.S. Geol. Surv., Reston, Va.

Lisowski, M. (2006) Analytical volcano deformation source models, in *Volcano Deformation: Geodetic Monitoring Techniques,* by D. Dzurisin, chap. 8, pp. 279–304, Springer-Praxis, Chichester, UK.

Matoza, R. S., M. A. Garcés, B. A. Chouet, L. D'Auria, M. A. H. Hedlin, C. De Groot-Hedlin, and G. P. Waite (2009), The source of infrasound associated with long-period events at Mount St. Helens, *J. Geophys. Res., 114,* B04305, doi:10.1029/2008JB006128.

Matoza, R. S., and B. A. Chouet (2010), Subevents of long-period seismicity: Implications for hydrothermal dynamics during the 2004–2008 eruption of Mount St. Helens, *J. Geophys. Res., 115,* B12206, doi:10.1029/2010JB0007839.

McChesney, P. J., M. R. Couchman, S. C. Moran, A. B. Lockhart, K. J. Swinford, R. G. LaHusen (2008), Seismic-Monitoring Changes and the Remote Deployment of Seismic Stations (Seismic Spider) at Mount St. Helens, 2004–2005, in *A Volcano Rekindled: The Renewed Eruption of Mount St. Helens, 2004–2006,* edited by D. R. Sherrod, W. E. Scott, and P. H. Stauffer, *Prof. Paper 1750,* chap. 7, pp. 129–140, U.S. Geol. Surv., Reston, Va.

Moran, S. C., S. D. Malone, A. I. Qamar, W. A. Thelen, A. K. Wright, and J. Caplan-Auerbach (2008a), Seismicity Associated with Renewed Dome Building at Mount St. Helens, 2004–2005, in *A Volcano Rekindled: The Renewed Eruption of Mount St. Helens, 2004–2006,* edited by D. R. Sherrod, W. E. Scott, and P. H. Stauffer, *Prof. Paper 1750,* chap. 2, pp. 27–60, U.S. Geol. Surv., Reston, Va.

Moran, S. C., P. J. McChesney, and A. B. Lockhart (2008b), Seismicity and Infrasound Associated with Explosions at Mount St. Helens, 2004–2005, in *A Volcano*

Rekindled: The Renewed Eruption of Mount St. Helens, 2004–2006, edited by D. R. Sherrod, W. E. Scott, and P. H. Stauffer, *Prof. Paper 1750,* chap. 6, pp. 111–127, U.S. Geol. Surv., Reston, Va.

Nagaoka, Y., K. Nishida, Y. Aoki, and M. Takeo (2010), Temporal change of phase velocity beneath Mt. Asama, Japan, inferred from coda wave interferometry, *Geophys. Res. Lett., 37,* L22311, doi:10.1029/2010GL045289.

Nishimura, T., N. Uchida, H. Sato, M. Ohtake, S. Tanaka, and H. Hamaguchi (2000), Temporal changes of the crustal structure associated with the M6.1 earthquake on September 3, 1998, and the volcanic activity of Mount Iwate, Japan, *Geophys. Res. Lett., 27,* 269–272.

Obermann, A., T. Planés, E. Larose, and M. Campillo (2013), Imaging preeruptive and coeruptive structural and mechanical changes with ambient seismic noise, *J. Geophys. Res., 118,* 1–10, doi:10.1002/2013JB010399.

Paige, C. C., and M. A. Saunders (1982), LSQR: An Algorithm for Sparse Linear Equations and Sparse Least Squares, *ACM Transactions on Mathematical Software, 8,* 43–71.

Pallister, J. S., C. R. Thornber, K. V. Cashman, M. A. Clynne, H. A. Lowers, C. W. Mandeville, I. K. Brownfield, and G. P. Meeker (2008), Petrology of the 2004–2006 Mount St. Helens Lava Dome—Implications for Magmatic Plumbing and Eruption Triggering, in *A Volcano Rekindled: The Renewed Eruption of Mount St. Helens, 2004–2006,* edited by D. R. Sherrod, W. E. Scott, and P. H. Stauffer, *Prof. Paper 1750,* chap. 30, pp. 648–702, U.S. Geol. Surv., Reston, Va.

Ratdomopurbo, A., and G. Poupinet (1995), Monitoring a temporal change of seismic velocity in a volcano: application to the 1992 eruption of Mt. Merapi (Indonesia), *Geophys. Res. Lett.,* 22(7), 775–778.

Sabra, K. G., P. Roux, P. Gerstoft, W. A. Kuperman, and M. C. Fehler (2006), Extracting coherent coda arrivals from cross-correlations of long period seismic waves during the Mount St. Helens 2004 eruption, *Geophys. Res. Lett., 33,* L06313, doi:10.1029/2005GL025563.

Schilling, S. P., R. A. Thompson, J. A. Messerich, and E. Y. Iwatsubo (2008), Use of Digital Aerophotogrammetry to Determine Rates of Lava Dome Growth, Mount St. Helens, Washington, 2004–2005, in *A Volcano Rekindled: The Renewed Eruption of Mount St. Helens, 2004–2006,* edited by D. R. Sherrod, W. E. Scott, and P. H. Stauffer, *Prof. Paper 1750,* chap. 8, pp. 146–167, U.S. Geol. Surv., Reston, Va.

Scott, W. E., D. R. Sherrod, and C. A. Gardner (2008), Overview of the 2004 to 2006, and Continuing, Eruption of Mount St. Helens, Washington, in *A Volcano Rekindled: The Renewed Eruption of Mount St. Helens, 2004–2006,* edited by D. R. Sherrod, W. E. Scott, and P. H. Stauffer, *Prof. Paper 1750,* chap. 1, pp. 3–22, U.S. Geol. Surv., Reston, Va.

Sens-Schönfelder, C., and U. Wegler (2006), Passive image interferometry and seasonal variations of seismic velocities at Merapi Volcano, Indonesia, *Geophys. Res. Lett.,* 33, L21302, doi:10.1029/2006GL027797.

Snieder, R. (2002), Coda wave interferometry and the equilibration of energy in elastic media, *Phys. Rev. E,* 66, 046615, doi:10.1103/PhysRevE.66.046615.

Thelen, W. A. (2010), Testing the sensitivity of precursory changes in multiplets to surficial phenomenon at Mount St. Helens (2004–2008), Abstract V33C-2392 presented at 2010 Fall Meeting, AGU, San Francisco, Calif., 13–17 Dec.

Thelen, W. A., R. S. Crosson, and K. C. Creager (2008), Absolute and Relative Locations of Earthquakes at Mount St. Helens, Washington, Using Continuous Data: Implications for Magmatic Processes, in *A Volcano Rekindled: The Renewed Eruption of Mount St. Helens, 2004–2006,* edited by D. R. Sherrod, W. E. Scott, and P. H. Stauffer, *Prof. Paper 1750,* chap. 4, pp. 71–95, U.S. Geol. Surv., Reston, Va.

Tsai, V. C. (2011), A model for seasonal changes in GPS positions and seismic wave speeds due to thermoelastic and hydrologic variations, *J. Geophys. Res.,* 116, B04404, doi:10.1029/2010JB008156.

Ueno, T., T. Saito, K. Shiomi, B. Enescu, H. Hirose, and K. Obara (2012), Fractional seismic velocity change related to magma intrusions during earthquake swarms in the eastern Izu peninsula, central Japan, *J. Geophys. Res.,* 117, B12305, doi:10.1029/2012JB009580.

Vallance, J. W., D. J. Schneider, and S. P. Schilling (2008), Growth of the 2004–2006 Lava Dome Complex at Mount St. Helens, Washington, in *A Volcano Rekindled: The Renewed Eruption of Mount St. Helens, 2004–2006,* edited by D. R. Sherrod, W. E. Scott, and P. H. Stauffer, *Prof. Paper 1750,* chap. 9, pp. 170–208, U.S. Geol. Surv., Reston, Va.

Waite, G. P., B. A. Chouet, and P. B. Dawson (2008), Eruption dynamics at Mount St. Helens imaged from broadband seismic waveforms: Interaction of the shallow

magmatic and hydrothermal systems, *J. Geophys. Res., 113,* B02305, doi:10.1029/2007JB005259.

Wegler, U., B.-G. Lühr, R. Snieder, and A. Ratdomopurbo, (2006), Increase of shear wave velocity before the 1998 eruption of Merapi volcano (Indonesia), *Geophys. Res. Lett.,* 33, L09303, doi:10.1029/2006GL025928.